Femtosecond Transient Absorption Spectroscopy – Technical Improvements and Applications to Ultrafast Molecular Phenomena

Dissertation zur Erlangung des naturwissenschaftlichen Doktorgrades
der
Julius-Maximilians-Universität Würzburg

vorgelegt von

Florian Kanal

aus Kirchheim unter Teck

Würzburg 2015

Eingereicht bei der Fakultät für Chemie und Pharmazie am _____

Gutachter der schriftlichen Arbeit
1. Gutachter: Prof. Dr. T. Brixner
2. Gutachter: _____

Prüfer des öffentlichen Promotionskolloquiums
1. Prüfer: Prof. Dr. T. Brixner
2. Prüfer: _____
3. Prüfer: _____

Datum des öffentlichen Promotionskolloquiums: _____

Doktorurkunde ausgehändigt am _____

List of Publications

[1] D. Reitzenstein, T. Quast, F. Kanal, M. Kullmann, S. Ruetzel, M. S. Hammer, C. Deibel, V. Dyakonov, T. Brixner, and C. Lambert,
Synthesis and Electron Transfer Characteristics of a Neutral, Low-Band-Gap, Mixed-Valence Polyradical,
Chem. Mater. **22**, 6641–6655 (2010).

[2] P. Rudolf, F. Kanal, J. Knorr, C. Nagel, J. Niesel, T. Brixner, U. Schatzschneider, and P. Nuernberger,
Ultrafast Photochemistry of a Manganese-Tricarbonyl CO-Releasing Molecule (CORM) in Aqueous Solution,
J. Phys. Chem. Lett. **4**, 596–602 (2013).

[3] P. Rudolf, F. Kanal, D. Gehrig, J. Niesel, T. Brixner, U. Schatzschneider, and P. Nuernberger,
Femtosecond Mid-Infrared Study of the Aqueous Solution Photochemistry of a CO-Releasing Molecule (CORM),
EPJ Web of Conferences **41**, 05004 (2013).

[4] F. Kanal, S. Keiber, R. Eck, and T. Brixner,
100-kHz Shot-to-Shot Broadband Data Acquisition for High-Repetition-Rate Pump–Probe Spectroscopy,
Opt. Express **22**, 16965–16975 (2014).

[5] F. Kanal, S. Ruetzel, H. Lu, M. Moos, M. Holzapfel, T. Brixner, and C. Lambert,
Measuring Charge-Separation via Oligomer Length Variation,
J. Phys. Chem. C **118**, 23586–23598 (2014).

[6] F. Kanal, D. Schleier, and P. Nuernberger,
The Ultrafast Photogeneration of the Tetrazolinyl Radical,
in preparation (2015).

[7] F. Kanal and P. Nuernberger,
Ultrafast Photochemistry of Tetrazolium Salts, Formazans, and Photo-TTC,
in preparation (2015).

Parts of this thesis have been published in some of the peer-reviewed journal articles listed on page iii. An overview of reprinted and adapted passages and the corresponding page numbers can be found in the tables below. The sources of adapted figures are additionally indicated at the end of the corresponding figure captions. For all reproduced material the permission for reprint was granted by the respective publishing company holding the copyright of the articles, if not the authors were copyright owners. In cases where the only modification were style corrections due to different journals' publishing styles, the text is considered as reproduced only.

Publication		Use in Dissertation	Page Number
[4][1]	pp. 2–3	text reproduced, modified, and extended	pp. 6–7
	pp. 3, 5, 10	figures reproduced	pp. 8, 29, 87
	pp. 7, 8, 9	figures adapted	pp. 32, 34, 35
	pp. 3–4	text reproduced and modified	p. 27
	pp. 4–5	text reproduced and modified	pp. 27–28
	pp. 4, 5–6	text reproduced and modified	pp. 28–30
	p. 6	text reproduced and modified	pp. 30–31
	pp. 6–10	text reproduced and modified	pp. 31–35
	p. 7	table adapted	p. 33
	p. 10	text reproduced, modified, and extended	p. 35–36
	p. 10	text reproduced	p. 87
[5][2]	pp. 1–2	content reproduced	pp. 37–39
	pp. 2	chart adapted	p. 38, 51
	pp. 9	chart reprinted	p. 38, 51
	p. 3	content reproduced	pp. 39
	pp. 3–7	text reproduced, modified, and extended	pp. 40–48
	pp. 4, 5, 6, S24, S25	figure adapted	pp. 40, 42, 43, 44, 45
	pp. 6, 8, 10	table reprinted	pp. 41, 50, 53
	pp. 7–8	text reproduced	pp. 48–49
	pp. 8–11	text in parts reproduced and modified	pp. 49–53
	pp. 8–10	text in parts reproduced and modified, equations reprinted	pp. 18–20
	p. 10	scheme reprinted	p. 53
	p. 11	text reproduced	pp. 53–54
	pp. S22–S23	text reproduced in single parts	pp. 40–48

[1] Reproduced and adapted with permission from: Optics Express **22**, 16965–16975 (2014). Copyright (2014) by the Optical Society of America.

[2] Reproduced and adapted with permission from: Journal of Physical Chemistry C **118**, 23586–23598 (2014). Copyright (2014) by the American Chemical Society.

Publication		Use in Dissertation	Page Number
[2][3]	pp. 1–2	content reproduced and extended	pp. 57–58
	pp. 2, 3	figure and subfigure adapted and merged to one single figure	p. 59
	p. 2	figure reprinted	p. 60
	pp. 2–3	content reproduced and extended	pp. 58–61
	p. 3	data from subfigures merged to one table	p. 60
	pp. 3, 4	figure adapted	pp. 62, 63
	pp. 3–5	content reproduced and extended	pp. 61–65
[6, 7]		text, figures, charts, and schemes will (partly) be used and modified in the publications currently in preparation	pp. 67–78, 87–90

For copyrighted material from other sources that was reproduced and adapted in this thesis, permission was granted by the respective copyright holder. The use of this material is indicated in the caption of the respective figure and listed in the following table.

Publication		Use in Dissertation	Page Number
[8][4]	p. 33	subfigure adapted	p. 9
	p. 53	subfigure adapted	p. 11
[9][5]	p. 62	figure adapted and extended	p. 24
	p. 95	figure adapted, used as subfigure	p. 62

[3]Reproduced and adapted with permission from: Journal of Physical Chemistry Letters **4**, 596–602 (2013). Copyright (2013) by the American Chemical Society.

[4]Reproduced and adapted with permission from: "Pulse-sequence approaches for multidimensional electronic spectroscopy of ultrafast photochemistry" (Dissertation, Universität Würzburg). Copyright (2014) by Dr. Stefan Rützel.

[5]Reproduced and extended with permission from: "Uncovering photoinduced chemical reaction pathways in the liquid phase with ultrafast vibrational spectroscopy" (Dissertation, Universität Würzburg). Copyright (2014) by Dr. Philipp Rudolf.

Contents

1 Introduction

A large number of molecular processes—both natural and artificial—are driven by light. The most prominent process in nature is photosynthesis, which turns sunlight into chemically available energy that fuels all biological life on earth. Plants as well as algae and some bacteria are capable of funneling absorbed light-energy on an ultrafast time scale from a collecting antenna to the photosynthetic reaction center. Another important light-driven phenomenon is the process of vision in the eye, in which an ultrafast isomerization of a chromophore embedded in a retinal protein is involved. Apart from these natural processes, mankind has begun decades ago to technologically exploit light-induced processes. Preparative photochemistry has made reaction products easily accessible which might not have been imaginable or only accessible via a large number of single synthesis steps in conventional chemistry. One reason for that is that by absorption of a photon, the amount of energy is about two orders of magnitude higher than the thermal energy available for a molecular process. The high photon energy is transferred quasi instantaneously into the molecular system. Thermal energy, i.e., heating, will strongly affect the vibrational and rotational excitation of the system as a whole without pushing the system towards a specific reaction channel accessible from an electronically excited state. Apart from synthetic chemistry, the development of photovoltaics made it possible to convert light-energy into chemical potentials and therefore providing electric energy.

When light-induced processes are studied, typically macroscopic quantities are measured. These indicate quantities such as overall efficiencies, reaction speeds, and changes in the samples' properties. The measured properties are usually averaged over a large number of individual microscopic steps that sum up to the overall observed process. For instance, a photochemical reaction shows a conversion within seconds to hours. However, the initial elementary reaction steps underlying the reaction proceed on a time scale of femto- to picoseconds (10^{-15} to 10^{-12} s).

For a basic understanding of the light-induced processes it is necessary to study the elementary steps with time-resolved techniques on a molecular level. The most prominent method to study liquid-phase dynamics is transient absorption spectroscopy. This experimental approach is a pump–probe experiment where the sample is excited with an ultrashort laser pulse. The ensuing non-equilibrium dynamics of the system are inspected with a second laser pulse. With suitable pulsed lasers it is possible to investigate the molecular dynamics on a time scale which is on the order of the most basic molecular phenomena itself. Transient absorption spectroscopy has been improved with respect to various aspects. On the technical side the utilizable frequency ranges and their respective bandwidths were maximized. Concomitantly, the number of studied systems has widely been enlarged. Some of the most prominent molecular processes studied with transient absorption spectroscopy are energy transfer, charge transfer, bond formation and breaking, bond rearrangements, and even more complex combinations of all these processes.

One limiting factor in spectroscopic experiments is measurement and averaging time. The issue of measurement time has two interconnected major aspects. The first is to efficiently measure and average time-resolved data to approach the technically possible signal-to-noise ratio. Therefore, it is desirable to shorten the overall measurement time. Secondly, the achieved data quality within a given acquisition time can strongly vary. That is, improved data quality in shorter measurement times make the investigation of sensitive or photodegrad-

ing samples possible when they are exposed only for shorter times to pulsed laser sources. By the same token, kinetic processes like the assembling of aggregates can be studied with ultrafast methods in different stages of the process of formation when the increment for a single measurement is sufficiently small enough. For this resason, the first aim of this thesis is to implement shot-to-shot detection for a 100 kHz transient-absorption spectrometer. The clear advantage of shot-to-shot data acquisition has already been demonstrated for a large number of low-repetition-rate lasers of repetition rates up to some kHz. Due to the strong correlation of consecutive laser pulses, calculating the change in absorbance for pairs of subsequent pulses is highly beneficial compared to other averaging and detection schemes. Therefore, it seems desirable to apply data acquisition with detection of every single pulse also for high repetition rates, potentially reducing the measurement time by orders of magnitude.

Apart from a technical advancement of the method, the main goal of this work is the application of time-resolved optical spectroscopy to a number of photoinduced processes. The complex phenomena mentioned at the beginning can be better understood when their constituting subprocesses are studied in less complex model systems. When emergent effects of multifaceted molecular architectures are not taken into consideration, the approach of studying smaller entities of the overall system leads to an improved understanding of the whole process itself. Under these assumption, in this thesis several light-induced molecular phenomena of increasing complexity are studied. Suitable model systems are taken into consideration, which show different photoinduced phenomena. The increasing complexity of the processes predetermines the structure of the thesis. Whilst the first process treated in this thesis leaves the molecular system intact and only a charge is transferred, in the second model system light absorption triggers the formation of new photoproducts. As a combination, the last example shows a combination of both in-depth studied processes.

The thesis is structured as follows. The fundamental aspects of ultrafast time-resolved spectroscopy are shortly introduced in Chapter 2 both from technical and theoretical points of view. In addition, the basic aspects of global analysis of time-resolved spectroscopic data are discussed. The experimental requirements for the experiments discussed in this thesis are given in this chapter as well.

The results for the implementation of a transient shot-to-shot absorption spectrometer are presented in Chapter 3. Apart from the new 100 kHz shot-to-shot data acquisition, the noise characteristics of the employed laser system are analyzed to quantify the advantage of shot-to-shot detection under the abovementioned criteria of measurement time and data quality.

A very important aspect in chemistry and nature is the transfer of charges which accompanies almost every chemical reaction and biochemical process. The results of a study of optically-induced electron transfer in donor–acceptor oligomers are shown in Chapter 4. The oligomers consist of alternating donor and acceptor units, allowing electron transfer throughout the whole chain. In order to better understand the charge separation in large polymers, the limited length of the molecular oligomer chains was systematically varied. The primarily targeted synthesis of the compounds allows a combination of ultrafast time-resolved spectroscopy with theoretical calculations. For data analysis, global lifetimes analyses are employed in combination with the calculation of the corresponding electron-transfer rates.

One of the most basic chemical reaction is the cleavage of a bond and the dissociation of a parent molecule into stable fragments or intermediates upon photoexcitation. With the release of a CO ligand, carbonyl complexes can be studied as exemplary systems for dissociation.

The change of the C–O stretching vibration corresponding to an altered binding-situation is an excellent probe in time-resolved mid-infrared spectroscopy. Therefore, in Chapter 5 the dissociation dynamics of a carbon-monoxide-releasing molecule are presented. Studying the elementary process of light-induced bond breakage is important to better understand the general photochemistry of this class of transition-metal complexes. Apart from that, also the therapeutic potential of CO release from metal carbonyls can be estimated better when not only the overall release properties but the single release steps are elucidated.

A third molecular photoinduced reaction combines both aspects studied in the chapters before. The breaking of bonds, the transfer of electrons, and additionally the reformation of a bond are a reaction sequence potentially occurring in the photochemistry of tetrazolium salts. Therefore, Chapter 6 presents the elucidation of the complex photochemistry of a tetrazolium salt. The compound class of tetrazolium cations shows a solvent-dependent photochemistry involving both electron transfer as well as bond breaking and formation to yield the respective photoproducts. Hence, the photochemistry of tetrazolium ions is a textbook example to study combined molecular phenomena in a small molecule on the way to understand even more complex reaction schemes in larger associated molecular systems.

Finally, the results of the thesis are summarized in Chapter 7. In addition, possible future experiments which might either confirm or even extend the results gained during the course of this thesis are discussed.

2 Theoretical Background and Experimental Techniques

The following chapter gives a short overview of some aspects forming the theoretical fundaments of the optical experiments presented in this thesis. For more detailed considerations the reader is referred to the textbooks and references cited in the text. Section 2.1 deals with the principles of ultrafast time-resolved spectroscopy. Briefly, the experimental acquisition of optical time-resolved data is outlined as a basis for the experimental data-acquisition development presented in Chapter 3. A special focus in Section 2.2 is put on photophysical and photochemical processes as well as their corresponding signal contributions in transient absorption spectroscopy. These explanations will be useful in the discussion of molecular photoinduced dynamics in Chapters 4 to 6. For a quantitative evaluation of molecular dynamics studied in this thesis global lifetime analysis is used, which is shortly introduced in Section 2.3. Section 2.4 will briefly review the fundamentals of nonlinear optics on which the optical devices necessary to perform ultrafast spectroscopy are based on. To complete the theoretical considerations, Section 2.5 describes the basics of different electron-transfer theories which are thereafter used in Chapter 4 to calculate and interpret electron transfer rates to explain the corresponding time-resolved experiments. Finally, the experimental setups and configurations for ultrafast spectroscopy applied in the different chapters of this thesis are described in Section 2.6.

2.1 Principles of Ultrafast Time-Resolved Sepectroscopy

For the time-resolved study of excited-state molecular dynamics or molecular processes like charge and energy transfer, conformational rearrangements as well as the detection of short-living reactive intermediates in chemical reactions the method of choice is the so-called pump–probe technique [10–12]. The general principle is to pump, i.e., to excite a molecular ensemble to a state above the ground state at an exactly defined moment in time. Subsequently, the excited-state dynamics are probed at different delay times τ between the pump and the probe event. A large variety of different experimental realizations for preparing excited-state populations or reactive intermediates and suitable probing methods can be employed. The pump event which triggers the population of the excited state in the sample system can either be irradiation of the sample with a laser pulse or radionuclides (e.g., α-particles) or a sudden change in temperature or pressure to transfer energy into the initial equilibrium system [13]. Pulsed lasers are intrinsically suitable for time-resolved experiments. Since the development of femtosecond laser sources almost four decades ago, ultrafast molecular processes can be studied with pulsed-laser techniques. For ultrafast optical excitations with laser pulses different observables can be detected as probe signals. For example, in gas-phase experiments either charged fragments of molecules or photoelectrons can be detected after dissociation of the parent molecule by either the pump or the probe pulse. In the liquid phase, either a change of absorbance can be measured or fluorescence emitted by the sample after excitation can be collected.

In the course of this thesis optical pump–probe spectroscopy was applied to study light-induced molecular dynamics. The so-called transient absorption spectroscopy is probably the

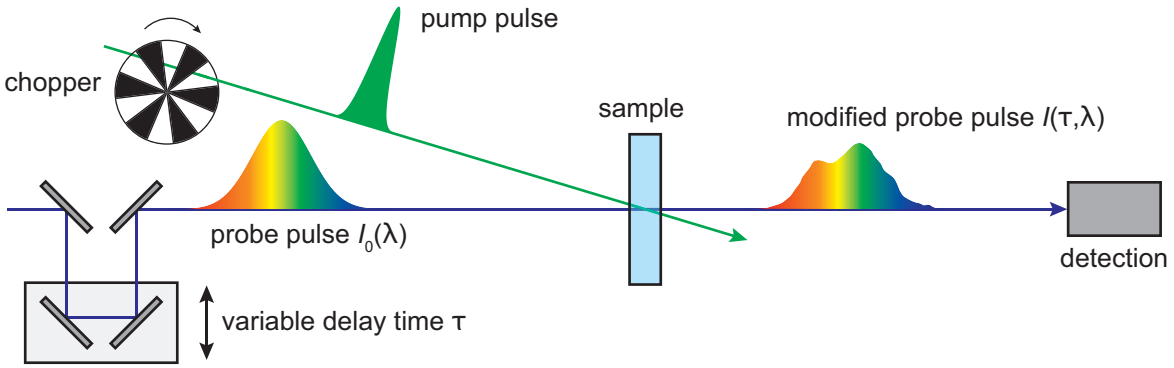

Figure 2.1: Schematic representation of a pump–probe experiment to measure photoinduced molecular dynamics. In the transient absorption technique, an optical pump pulse excites the molecular sample whereas a temporally delayed probe pulse measures the pump-induced change in the sample's absorbance. Therefore, the wavelength-dependent intensity of the probe spectra has to be measured with and without the pump interaction. See the text for further explanations.

most common pump–probe variation in the liquid phase measuring the pump-induced difference in the sample's absorbance of a probe pulse. The central wavelength of the excitation pulse is chosen to fit to the linear absorption of the molecular sample under investigation. The spectrum of the probe pulse is determined by the molecular event to be studied. Probe spectra in the ultraviolet (UV) and visible (Vis) regime are used to study electronic transitions and absorptions of photoproducts. Furthermore, mid-infrared (MIR) probe pulses can be used to examine molecular vibrations what is especially useful when structurally different reactive intermediates have to be distinguished from another. As the absorption bands in the MIR region are spectrally narrower than in the visible and structure-specific, assignments to possible chemical structures can be made more easily. The schematic procedure of transient absorption spectroscopy is depicted in Fig. 2.1. Independently of the spectral regime, in transient absorption spectroscopy an ultrashort pump pulse excites a subensemble of a molecular sample and a second laser pulse probes the absorption as a function of the probe wavelength λ and delay time τ. The delay time τ can be adjusted by changing the length of one pulse's optical pathway. An adjustable mechanical stage as delay line is typically used for measurements of delay times up to a few nanoseconds. Nowadays, excitation from the UV up to the near-infrared (NIR) spectral regime with probing in the UV/visible or the MIR spectral regime is routinely used. Of special interest are probe supercontinua which in combination with multi-channel detection allow a frequency-resolved acquisition of broadband difference spectra [14, 15]. The different optical devices needed for generating the respective pump and probe pulses will be introduced in Section 2.4.

The desired signal for transient absorption spectroscopy is derived from measuring the probe pulses as follows. The absorbance $A(\lambda)$ of each probe pulse is defined by the intensity of the incident and transmitted light, $I_0(\lambda)$ and $I(\lambda)$, in the Beer–Lambert law,

$$A(\lambda) = \lg \frac{I_0(\lambda)}{I(\lambda)}, \tag{2.1}$$

via the decadic logarithm. Experimentally, one is interested in the change in absorbance $\Delta A(\tau,\lambda)$ induced by the pump pulse defined as the difference between the absorbance of the pumped $[A_\mathrm{p}(\tau,\lambda)]$ and the unpumped sample $[A_\mathrm{u}(\lambda)]$:

$$\Delta A(\tau,\lambda) = A_\mathrm{p}(\tau,\lambda) - A_\mathrm{u}(\lambda) = \lg \frac{I_0(\lambda)}{I_\mathrm{p}(\tau,\lambda)} - \lg \frac{I_0'(\lambda)}{I_\mathrm{u}(\lambda)}. \tag{2.2}$$

Typically, however, one does not measure the incident probe intensities I_0 and I_0'. Rather one calculates the absorbance change in an approximate but simplified version from

$$\Delta A(\tau,\lambda) = \lg \frac{I_\mathrm{u}(\lambda)}{I_\mathrm{p}(\tau,\lambda)}. \tag{2.3}$$

If the incident probe intensities are equal and do not fluctuate between the two measurements, Eq. (2.2) and Eq. (2.3) give the same result, otherwise an error is introduced. Thus the evaluation with Eq. (2.3) works well if the intensities between successive measurements are well correlated. Since this condition is fulfilled on a shot-to-shot basis for 1 kHz laser systems, shot-to-shot detection is advantageous and is nowadays employed in many laboratories by blocking every second pump pulse with an optical chopper (Fig. 2.1). However, finite data readout times of the detector and the maximum speed of the pump-beam chopper have so far limited this approach to lasers with repetition rates of a few kHz.

For high repetition rates ($\geq$ 100 kHz) one typically averages $I_\mathrm{p}(\tau,\lambda)$ and $I_\mathrm{u}(\lambda)$ over k successive probe pulses on the detector. The blocking of the pump beam can either be performed with a mechanical shutter or a rotating chopper. The change in absorbance is calculated for two subsequent averaged sequences of k probe pulses with the corresponding pump pulses blocked or unblocked (Fig. 2.2, state of the chopper highlighted in gray). For one delay time τ the change in absorbance is averaged n times. The number of detected pulses is $i = 2nk$ for each τ (Fig. 2.2). The averaging of the change in absorbance is repeated for t time delays τ constructing a transient map. The signal-to-noise ratio can further be improved by averaging over N individual transient maps measured successively. In Chapter 3 the development of an experimental realization of a 100 kHz shot-to-shot transient absorption experiment is described in detail.

2.2 Basic Concepts of Photophysics and Photochemistry

A brief overview of quantum-mechanical and phenomenological treatments of photophysical and photochemical processes is given in the following. Detailed explanations can be found in textbooks [13, 16, 17] and the cited references in the text.

For molecules which are of the size of several hundreds of picometers, quantum mechanics has to be applied for a correct description of their properties. Within the scope of this thesis it is sufficient to assume that the oscillating electromagnetic field $\boldsymbol{E}$ is constant along the spatial dimension of the molecule as the wavelength of the used light pulses is much larger than a typical molecule. In this dipole approximation the dipole moment $\boldsymbol{\mu}$ of a molecule can be calculated by the expectation value of the quantum mechanical dipole operator $\hat{\boldsymbol{M}}$ for the molecule's overall wavefunction $|\Psi\rangle$,

$$\boldsymbol{\mu} = \langle\Psi|\hat{\boldsymbol{M}}|\Psi\rangle = -\langle\Psi|e\,(\Sigma \boldsymbol{r}_i - \Sigma Z_N \boldsymbol{R}_N)\,|\Psi\rangle, \tag{2.4}$$

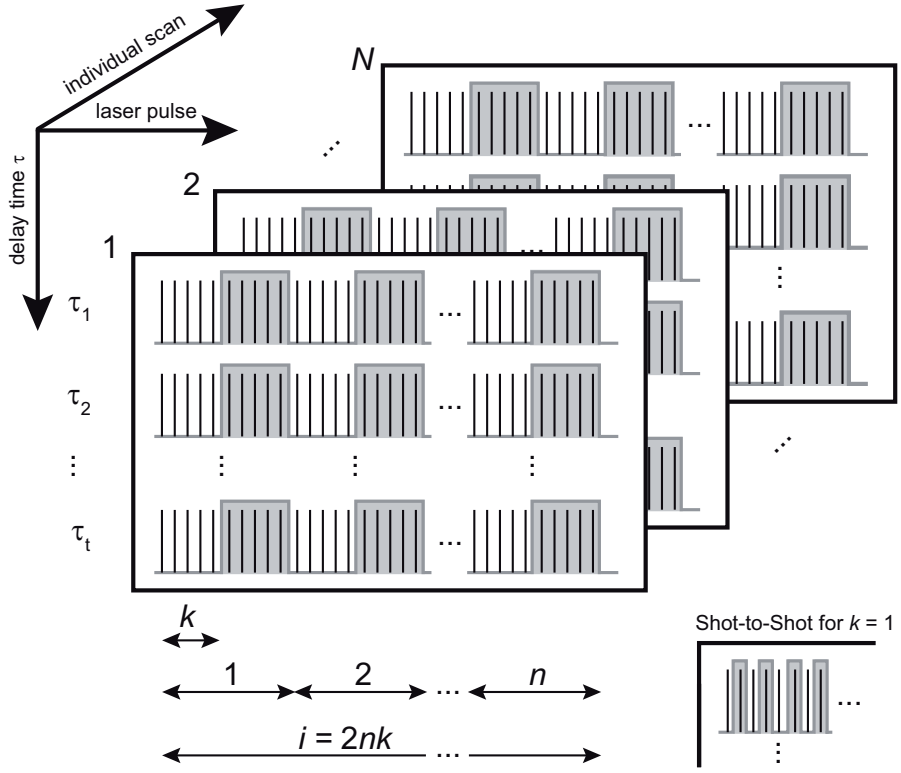

Figure 2.2: Typical scheme for measuring and calculating changes in absorbance $\Delta A(\tau,\lambda)$. For k probe pulses averaged on the detector the chopper either blocks or transmits k successive pump pulses (state of the pump chopper shown in gray). At a given delay time τ the change in absorbance is averaged over n values of $\Delta A(\tau,\lambda)$, resulting in an overall number of i recorded pulses. Afterwards a set of N transient maps each one consisting of t delay times τ can be averaged. For $k = 1$ the calculation of $\Delta A(\tau,\lambda)$ is done on a shot-to-shot basis (inset on lower right). Reprinted with permission from Ref. [4]. Copyright (2014) Optical Society of America.

with the nuclear charge Z and the elementary charge e. The coordinates of the N nuclei are represented by the vectors $\boldsymbol{R}_N$ and of the i electrons by the vectors $\boldsymbol{r}_i$, both contributing to the dipole operator $\hat{\boldsymbol{M}}$. The matrix element for a light-induced transition from an initial (i) to a final (f) quantum-mechanical state is in that case

$$W_{\mathrm{fi}} = \langle \Psi_{\mathrm{f}} | \boldsymbol{\mu}_{\mathrm{fi}} \boldsymbol{E} | \Psi_{\mathrm{i}} \rangle , \tag{2.5}$$

with the transition dipole element $\boldsymbol{\mu}_{\mathrm{fi}}$ which in turn reads

$$\boldsymbol{\mu}_{\mathrm{fi}} = \langle \Psi_{\mathrm{f}} | \hat{\boldsymbol{M}} | \Psi_{\mathrm{i}} \rangle . \tag{2.6}$$

In the following, only electronic and vibrational transitions are considered as rotational transitions cannot be resolved in condensed phase and are therefore neglected in the studies presented in the subsequent chapters.

In the Born–Oppenheimer approximation, the overall wavefunction $|\Psi\rangle$ can be factorized into an electronic wavefunction $|\Psi_{\mathrm{el},n}(\boldsymbol{r},\boldsymbol{R})\rangle$, a nuclear wavefunction $|\chi_v(\boldsymbol{R})\rangle$ at a given electronic state for the electronic quantum number n and the vibrational quantum number v, and a spin wavefunction σ:

$$|\Psi\rangle = |\Psi_{n,v,\sigma}(\boldsymbol{r},\boldsymbol{R})\rangle = |\Psi_{\mathrm{el},n}(\boldsymbol{r},\boldsymbol{R})\rangle \, |\chi_v(\boldsymbol{R})\rangle \, |\sigma\rangle . \tag{2.7}$$

For electronic transitions the spin wavefunctions are orthonormal and therefore their integrals are either one (transition between states of the same spin multiplicity) or zero (transitions between states of different spin multiplicity, "spin selection rule"). Therefore, the spin term of the overall wavefunction in the description of transitions is omitted for simplicity. For adiabatic conditions, i.e., for cases with no interaction of different electronic states, the kinetic coupling elements of nuclear wavefunctions in different electronic states can be neglected and therefore the Born–Oppenheimer approximation holds.

With the factorized wavefunction, the transition dipole moment for a vibronic transition can be separated into the electronic transition dipole moment $\boldsymbol{M}_{\mathrm{el},n}$ and a vibrational overlap integral (Franck–Condon factor):

$$\boldsymbol{\mu}_{\mathrm{fi}} = -e \left\langle \Psi_{\mathrm{el,i}}(\boldsymbol{r},\boldsymbol{R}) | \Sigma \boldsymbol{r}_i | \Psi_{\mathrm{el,f}}(\boldsymbol{r},\boldsymbol{R}) \right\rangle \left\langle \chi_{v''} | \chi_{v'} \right\rangle = \boldsymbol{M}_{\mathrm{el},n} \left\langle \chi_{v''} | \chi_{v'} \right\rangle . \tag{2.8}$$

Both factors determine the transition probability and selection rules for molecular spectroscopy. The intensity I_{trans} of a transition is proportional to the squared transition dipole moment,

$$I_{\mathrm{trans}} \propto |\boldsymbol{\mu}_{\mathrm{fi}}|^2. \tag{2.9}$$

Apart from the previous theoretical considerations, transitions in molecules can be described in a more phenomenological manner. State diagrams were first introduced by Jabłoński for that reason [18, 19]. Figure 2.3 shows a schematic state diagram in which horizontal lines represent an exemplary molecule's eigenstates whose energies E are given by the vertical position on the energy axis. Different electronic states in the vibrational ground state are depicted as thicker lines and the corresponding spin multiplicity is given with S for singlet and T for triplet states. The electronic states possess several vibrational levels v for each vibrational mode. Resonant absorption (A, Fig. 2.3) of photons from the lowest electronic state (S_0) to higher-lying electronic states (S_1, S_n) are indicated by vertical arrows. For open-shell systems like treated in Chapter 4, the lowest electronic state might be of different spin multiplicity than a singlet but the state diagram still holds. After an excited state has been populated on the time scale of several hundreds of atto- to a few femtoseconds, radiative and non-radiative relaxation processes take place. Non-radiative relaxation via vibrational relaxation, i.e., dissipation of energy into energetically lower vibrational modes and to the surrounding bath is

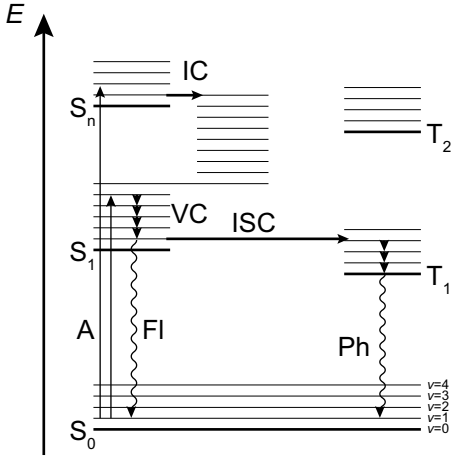

Figure 2.3: Schematic Jabłoński state diagram for an example molecular system. Horizontal lines depict levels with energy E. Electronic states are depicted with S for singlet and T for triplet states. The subscript denotes their relative order in energy. For further explanation see text. Adapted with permission from Ref. [8]. Copyright (2014) Dr. Stefan Rützel.

typically the fastest relaxation process occurring within femto- to picoseconds. Vibrational relaxation is often referred to as vibrational cooling (VC). Relaxation from an excited electronic state to another electronic (excited) state is called internal conversion (IC). For this process vibrational levels of different electronic states of the same spin multiplicity have to be close in energy and nuclear configuration. If so, a transition to the lower-lying electronic state is a possible relaxation pathway within few hundreds of femto- to some nanoseconds. When the spin multiplicities differ for the starting and ending state, the passage to another electronic state is called intersystem crossing (ISC).

A dominant radiative relaxation process is emission of light via fluorescence (Fl). The fluorescence emission typically leads to relaxation of the molecule to the electronic ground state. The transition probability to a certain vibrational state in the electronic ground state depends on the Franck–Condon factor [Eq. (2.8)]. Similar to the case of absorption, the wavefunction overlap and the transition dipole moment determine the signal intensity of fluorescence. Most organic molecules show the largest energy gap between S_0 and S_1, therefore fluorescence is typically observed from the S_1 state. Only few examples like azulene are known to show fluorescence from the S_2 state [13]. Radiative transitions disobeying the spin selection rule, hence emitting from a triplet to the singlet ground state are called phosphorescence (Ph), and typically exhibit the slowest rates of the processes described in this section on the order of seconds up to minutes or even longer. Another non-radiative relaxation process is optically-induced electron transfer (Section 2.5). Apart from the photophysical processes described above, photochemical processes can occur upon photoexcitation. Among them are isomerizations as well as the formation and breaking of bonds. Some of these processes will be addressed in more detail in Chapters 4 to 6.

In general, photophysical and photochemical processes possess various signal contributions in transient absorption spectroscopy (Fig. 2.4). After excitation the molecular sample shows a reduced ground-state absorbance as the ground state is partially depopulated. Therefore, the occurrence of reduced absorbance of the probe pulse is called ground-state bleaching (GSB). The calculated change in absorbance ΔA shows a negative signal contribution at the spectral positions of the steady-state absorption bands. When the interaction of the probe pulse with an excited molecule stimulates the repopulation of the ground state via emission of a photon, this stimulated emission (SE) leads to a signal decrease of ΔA in the probe range where the molecule emits. When the interaction with the probe pulse further promotes an already excited molecule to a higher-lying excited state, the decrease in the probe's intensity due to the excited-state absorption (ESA) leads to a positive signal contribution. When a photoproduct is formed after excitation, the newly formed molecule interacts with the probe pulse as well. The new product absorption (PA) can be detected by a positive signal in the transient data.

2.3 Global Lifetime Analysis

Information about a molecular system can be extracted from time-resolved measurement data when the data is fitted with an adequate model. Probably the analysis method most often used for time-resolved measurements is global analysis [20–24]. The following section gives an introduction about the basics of global data analysis. For further reading the reader is referred to Ref. [23]. Typically, like in this thesis, time-resolved transient absorption spectroscopy yields multidimensional data sets where one independent dimension is given by the delay-time axis τ

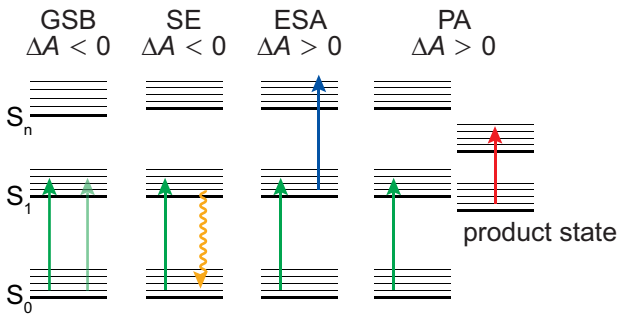

Figure 2.4: Signal contributions in transient absorption spectroscopy. Both the ground-state bleaching (GSB) and the stimulated emission (SE) result in a negative change in absorbance $\Delta A < 0$. The excited-state absorption (ESA) and the absorption of a photoproduct (PA) give a positive signal $\Delta A > 0$. A more detailed explanation is given in the text. Adapted with permission from Ref. [8]. Copyright (2014) Dr. Stefan Rützel.

and the other one by the probe wavelength λ. The dependent variable is in transient absorption spectroscopy the change in absorbance $\Delta A(\tau,\lambda)$ [Eqs. (2.2) and (2.3)]. Time-resolved spectroscopic data ΔA is considered as a superposition of n_{comp} different components each with its spectral properties $\epsilon_l(\lambda)$. The change of the sample's absorbance is the sum of the single changes in the spectroscopic changes $\Delta\epsilon_l(\lambda)$ weighed with each time-dependent concentration $c_l(\tau)$ [23],

$$\Delta A(\tau,\lambda) = \sum_{l=1}^{n_{\text{comp}}} c_l(\tau)\Delta\epsilon_l(\lambda). \tag{2.10}$$

In principle, such a data set can be evaluated by either kinetic or spectral models [23]. The model used in this thesis is the kinetic model where the temporal evolution of the concentrations c_l are assumed to be all given by first-order kinetics. Thus, Eq. (2.10) is described by a set of linear differential equations which is solved by a sum of exponential decays of the form,

$$c_l(\tau) = \exp(-k_l\tau), \tag{2.11}$$

with the decay rate k_l for each component. The approach of treating decay rates as first-order kinetics is valid for dynamics of most molecular systems. However, for a few physical processes a distribution of decay rates might be a better description of the experimental data [25]. In a global fitting approach with a kinetic model, the spectral properties $\Delta\epsilon_l(\lambda)$ are not constrained whereas the temporal properties are parameterized within Eq. (2.11). The amplitudes of the global fit, i.e., the exponential prefactors are called decay-associated difference spectra (DADS) and feature the spectral difference profiles of a certain component associated with the decay rate k_l. The components' concentrations decay independently in a parallel manner. Hence, when the experimental instrument response function (IRF) is taken into account by convolution, the parallel data model reads,

$$\Delta A(\tau,\lambda) = \sum_{l=1}^{n_{\text{comp}}-1} \text{DADS}_l(\lambda) \times \exp(-k_l\tau) \otimes IRF. \tag{2.12}$$

A different approach is the sequential model where the decay of one component gives rise to another and where no branching is possible. The amplitudes in this reaction scheme are called evolution-associated difference spectra (EADS). In the sequential model a weighing factor b for the concentrations is contained,

$$\Delta A(\tau,\lambda) = \sum_{l=1}^{n_{\text{comp}}-1} \text{EADS}_l(\lambda) \times \sum_{j=1}^{l} b_j \exp(-k_l\tau) \otimes IRF, \tag{2.13}$$

with the compartment number $j \leq l$. The weighing factor b can be modified so that more complex models than the parallel or sequential one can be solved for a better suited description of the photoinduced processes. Target models without pure parallel or pure sequential rates lead to species-associated difference spectra [20]. Anyhow, the quality of the fit, e.g., the value of χ^2 in a least-squares fit, does not have to be better for a more appropriate model. For evaluating the quality of a certain model, other methods as for instance a bayesian probability analysis have to be performed [26].

The sequential model is mathematically interconvertable into the parallel model but not vice versa [23]. For this practical reason, fitting with a sequential model is often preferred for a first data analysis. Spectral models are less often used to fit transient absorption data and are of more interest for data sets with poor temporal resolution [23]. A combination of both models leads to spectrotemporal models where a priori knowledge—which is only seldomly given—of the system is needed to set it up. When no a priori knowledge of the model is at hand, the lifetime density approach can be used to estimate the number of lifetime components from a data set without previous input of lifetimes or lifetime distributions [27–29].

As the data set $\Delta A(\tau,\lambda)$ can be considered as a $t \times s$ matrix with the matrix elements $\Delta A(\tau,\lambda)_{ts}$, which contains the measurement point at a certain delay time τ and a probe wavelength λ, matrix decomposition techniques [30] like singular-value decomposition can help to estimate the number of required kinetic parameters. In this thesis, the open-source program Glotaran [31] was used to perform global fits of the obtained time-resolved data (Chapter 3 to 6). Glotaran is a Java-based graphical user interface which employs the statistical fitting package TIMP [32] deveoloped in the statistical software environment *R* [33].

2.4 Nonlinear Optics and Light Sources for Ultrafast Laser Spectroscopy

Ultrafast time-resolved spectroscopy, i.e., spectroscopy with temporal resolution short enough to study molecular processes, requires light sources producing sub-picosecond laser pulses. With the realization of mode-locking, first subpicosecond lasers were developed almost 40 years ago [34, 35]. From then on, ultrashort pulsed lasers were constantly improved considering spectral bandwidths and pulse durations. The foundation of femtosecond lasers and the frequency conversion of femtosecond laser pulses are nonlinear optical effects. The following paragraphs will give a short introduction into the principles of nonlinear optics and the optical devices needed for the experimental realizations as basis for different kinds of spectroscopic techniques. Further detailed descriptions of nonlinear optics and femtosecond spectroscopy can be found e.g., in Refs. [36–38].

The most prominent laser sources for femtosecond pulses are nowadays titanium-doped sapphire (Ti^{3+}:Al_2O_3, Ti:Sa) solid-state lasers. The high nonlinear refractive index of Ti:Sa allows passive Kerr-lense mode-locking to achieve pulse lengths down to about 6 fs [36]. Therefore, these lasers can both be used for pulse generation in oscillators as well as for pulse amplification in amplifiers. To pump the lasing medium, adequate pump lasers have to be used. In the case of high-repetition-rate lasers, the pump source is a continuous-wave (cw) laser, at lower repetition rates the pump laser is typically also pulsed. For both purposes, typically diode-pumped solid-state lasers are used. Intensity fluctuations of the pump laser

influence the intensity stability of the output pulses what is further discussed in Section 3.3. Titanium:sapphire oscillators typically produce sub-100 fs laser pulses [39] where the central wavelength of the stimulated emission from a pumped Ti:Sa crystal can be tuned from about 660 to 986 nm depending on the cavity mirror material and the pump source [40]. The repetition rate of pulsed lasers is given by the cavity length and is typically around 80 MHz for Ti:Sa oscillators.

The conversion processes, discussed in the next paragraph are necessary to tune the laser pulses to frequency domains matching the absorption of molecular samples under study and to provide pulses short enough for highest temporal resolutions of few tens of femtoseconds. Pulse powers of oscillator pulses are generally not high enough to accomplish the necessary nonlinear effects for frequency conversions, which is the reason why they have to be amplified in energy prior to any frequency conversion processes. In this amplification process the oscillator pulses are stretched in their duration with an external stretcher and injected into another Ti:Sa laser cavity. With each passage through the amplification Ti:Sa crystal the pulse energy gets enhanced. Temporal pulse stretching is necessary to avoid damage in the amplification cavity due to high peak intensities. After being ejected from the amplifier cavity, the amplified pulse is recompressed again by means of e.g., a grating compressor to obtain its final pulse length from few to about several hundred femtoseconds. Depending on the spectral bandwidth which is obtained after amplification, the minimal achievable pulse length is given by the Fourier limit of laser pulses,

$$\tau_{\mathrm{P}} \Delta\omega \geq 2\pi c_{\mathrm{b}}, \tag{2.14}$$

where τ_{P} and $\Delta\omega$ are the temporal and spectral full width at half maximum (FWHM) of the pulse, respectively. The threshold value c_{b} can take different values for different types of spectral pulse shapes. The repetition rate of an amplifier is reduced due to restrictions e.g., of laser-medium excited-state lifetimes, cavity-dumping electronics, and electronics for minimizing cavity losses (Q-switching) from about 1 kHz to several hundreds of kHz.

The emission of a Ti:Sa amplifier which is typically operated at a fixed central wavelength around 800 nm has to be converted for the respective spectroscopic needs. Different nonlinear processes can be exploited with ultrashort laser pulses as their high power is sufficient to drive frequency conversion processes in nonlinear materials. For high-power electromagnetic fields many materials show a nonlinear response to the applied field. This nonlinear response in turn couples to the applied field [38]. The optical polarization $\boldsymbol{P}$, being the most important property for nonlinear optical effects reads,

$$\boldsymbol{P} = \epsilon_0 \left[\chi^{(1)} \boldsymbol{E}_1 + \chi^{(2)} \boldsymbol{E}_1 \boldsymbol{E}_2 + \chi^{(3)} \boldsymbol{E}_1 \boldsymbol{E}_2 \boldsymbol{E}_3 + \chi^{(n)} \boldsymbol{E}_1 \ldots \boldsymbol{E}_n \right], \tag{2.15}$$

for n interactions with $i \leq n$ incident light fields $\boldsymbol{E}_i$, the n-th order susceptibility $\chi^{(n)}$ of the material, and the permittivity of vacuum ϵ_0. Note that the number of light pulses does not necessarily have to be as large as the number of interactions. For the incident and exiting light fields conservation of energy and momentum has to apply, i.e., the frequencies ω_i and wavevectors $\boldsymbol{k}_i$ have to sum up, reading for a second order ($n = 2$) process,

$$\omega_1 + \omega_2 = \omega_3, \tag{2.16}$$

$$\boldsymbol{k}_1 + \boldsymbol{k}_2 = \boldsymbol{k}_3. \tag{2.17}$$

The most convenient method to fulfill these two boundary conditions is the so-called phase matching where the incident fields are superimposed under certain angles of incidents in a

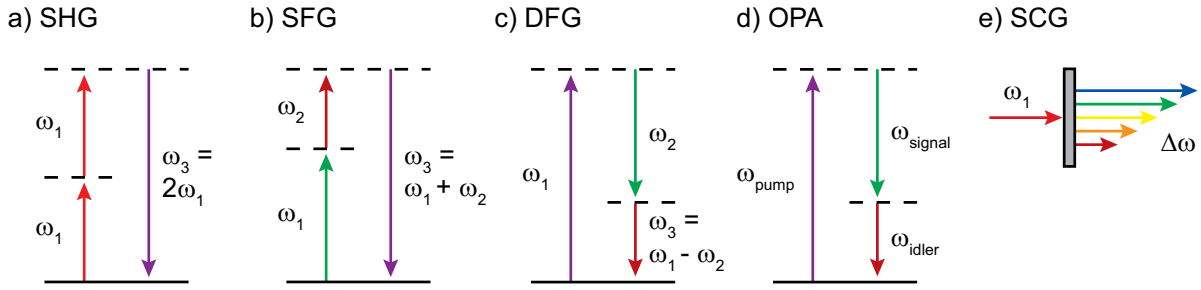

Figure 2.5: Schematic representation of nonlinear processes for frequency conversions of femtosecond laser pulses. a) The frequency of one single or two fundamental beams is doubled by second-harmonic generation (SHG). b) The sum-frequency generation (SFG) of two input frequencies ω_1 and ω_2 results in an output with the frequency $\omega_3 = \omega_1 + \omega_2$. c) Contrary to that, difference-frequency generation (DFG) gives the difference $\omega_3 = \omega_1 - \omega_2$. d) Optical parametric amplification (OPA) is the amplification of a seed beam of frequency ω_{seed} with a pump beam (ω_{pump}) higher in frequency resulting in the output of an amplified pulse ω_{signal} and an idler pulse ω_{idler}. Note that in the state level diagramm, the seed pulse is not shown. e) Supercontinuum generation (SCG) leads to a spectrally broadened output from a single input frequency ω_1. See text for a detailed discussion of the nonlinear processes shown.

birefringent nonlinear crystal (NLC). In this case, the frequency-converted light field is emitted in a predetermined direction with an efficiency increasing and a conversion bandwidth decreasing with increasing thickness d of the crystal. Birefringence is a precondition for second-order processes as otherwise—due to the inversion symmetry of the crystal—no net output field would be created. Processes of susceptibilities of orders higher than $n = 3$ are relatively unlikely as large input powers are needed.

In the course of this thesis, some nonlinear processes were employed for the generation of the pump and probe pulses (Fig. 2.5). In particular, these processes are second-harmonic generation (SHG), optical parametric amplification (OPA), noncollinear optical parametric amplification (NOPA), and difference-frequency generation (DFG). The simplest second-order frequency-conversion process is the generation of the second harmonic (Fig. 2.5a). For this purpose, a single fundamental beam (ω_1) is doubled in frequency so that $\omega_3 = 2\omega_1$ [41]. Second-harmonic generation can also be carried out in a noncollinear way when two beams of the same frequency ($\omega_1 = \omega_2$) are superimposed spatially and temporally in a χ^2-medium of adequate crystal symmetry.

When two pulses of different frequencies are overlapped in a suitable nonlinear medium, the output field is characterized by the sum of both incoming pulses' frequencies ($\omega_3 = \omega_1 + \omega_2$). Therefore, this process is called sum-frequency generation (SFG). In this context, SHG is the degenerate case of SFG. With an appropriate nonlinear medium of the right orientation also the difference of both frequencies can be achieved ($\omega_3 = \omega_1 - \omega_2$) what is then called difference-frequency generation (DFG, Fig. 2.5c). The abovementioned processes all involve the same quantum-mechanical initial and final state in the different crystals and are therefore called parametric [37].

Optical parametric amplification is the amplification of a seed pulse (ω_{seed}) by a pump pulse of higher energy and frequency ($\omega_{\text{pump}} > \omega_{\text{seed}}$) yielding in the output of an amplified pulse with frequency $\omega_{\text{signal}} = \omega_{\text{seed}}$ (signal pulse), an attenuated pulse of the pump frequency ω_{pump},

and—due to reasons of energy conservation—an idler pulse with frequency ω_{idler} being lower than that of the seed pulse.

The practical usefulness of the processes described above is the following. As the visible spectral regime is difficult to cover with mode-locked solid-state lasers [38], visible pump pulses have to be generated in a different way. From the fundamental amplified Ti:Sa output visible pump pulses can be generated in optical parametric amplifiers (OPAs, see Section 2.6.2). Therefore, one part of the fundamental beam is frequency-doubled in a β-barium-borate (β-BaB_2O_4, BBO) crystal. The frequency-doubled pump beam is overlapped with a broad whitelight supercontinuum spectrum (see below) in another BBO crystal. According to the orientation of the second crystal, i.e., for which wavelength bandwidth phase matching is fulfilled at a given angle, one part of the seed supercontinuum is amplified. As described above, an additional idler beam is generated simultaneously in this process. Depending on the desired spectral bandwidth of the amplified signal pulse either a collinear or noncollinear optical parametric amplifier (OPA or NOPA, respectively) can be utilized. With a noncollinear arrangement of seed and pump pulses for the optical parametric amplification, a much broader amplification bandwidth can be achieved. Overcoming the spectral bandwidth limitation of OPA in the noncollinear geometry was first shown for optical parametric oscillators [42, 43]. In general, OPAs and NOPAs use a second amplification stage to achieve pulse energies sufficiently high for ultrafast spectroscopy. With an additional nonlinear crystal the signal and the idler can be mixed yielding a difference-frequency signal pulse which is employed to generate mid-infrared pulses [44] (Section 2.6.2).

For high pulse energies many transparent materials like sapphire (Al_2O_3) and calcium fluoride (CaF_2) show self-phase modulation (SPM) as a third-order response to an intense light field. The refractive index of the medium is changed by the high intensity of the input pulse ("optical Kerr effect") and therefore, the instantaneous frequency ω_{inst} is altered, leading to a spectrally broadened output pulse. Spectral broadening due to SPM is the dominant process allowing for supercontinuum generation (SCG, Fig. 2.5e). To date, the whole process of SCG is not completely understood. Anyhow, whitelight supercontinua can be used as seed pulses for OPAs and as probe pulses for broadband optical probes in transient absorption spectroscopy [14, 45–50]. The spectral and temporal shape of whitelight supercontinua strongly depends on several parameters of the pump pulse. Among them are pulse energy, central frequency ω_1, pulse length as well as the photon flux per area, and the nonlinear medium itself.

2.5 Electron Transfer in Theory and Experiment

Electron and charge transfer (ET and CT) processes are ubiquitous in nature as well as in chemical reactions. Photosynthesis is the most prominent example in nature where the transfer of electrons turns the energy of absorbed photons into a chemical gradient and therefore into a source of chemical energy. Basically all chemical reactions are accompanied by an exchange of electrons from one reactant or the solvent to another reactant or vice versa. Nowadays, many technological developments like photovoltaics and light-emitting diodes are based on CT processes. Apart from an abundance of textbooks (e.g., Refs. [51–53]), in literature charge transfer is reviewed for different synthetic systems in experiment and theory [54–57]. The overwhelming number of CT processes makes them a research subject often studied in

detail. This section introduces some theoretical aspects of CT as a basis for the analysis of the experimental results in Chapter 4.

One approach to quantify experimental results on CT processes is to calculate the corresponding CT rates (Section 4.5). In the following section an overview of Marcus theory, a theoretical treatment of ET processes, is given. Although being elegant in its simplicity whilst describing many experimentally observed phenomena correctly, Marcus theory has experienced a number of improvements and extensions to even better describe CT in molecular systems.

At first, CT was mainly studied for intermolecular ET between solvated ions [58]. One of the first intramolecular ET reactions was studied in a binuclear metal complex $[(NH_3)_5Ru(\mu\text{-}pz)Ru(NH_3)_5]$ (pz = pyrazine) [59]. These systems were termed mixed-valence (MV) compounds due to their equivalent metal centers of different redox states between which the charge is transferred. Soon after the first metallic MV system, pure organic compounds were synthesized which could be named MV compounds as well. However, many of these compounds show strong charge delocalization and might therefore not be considered as MV compounds [56].

2.5.1 Classical Marcus Theory

A classical approach to theoretically address electron or more general charge-transfer phenomena is Marcus theory. Introduced by Marcus in 1956 [60], it basically considers outer-sphere electron transfers, e.g., ET between solvated metal ions (self-exchange), but can also be applied to intramolecular electron transfers as employed in this thesis.

In principle when CT is considered, one differentiates between thermally-induced CT, photoinduced, and optically-induced CT. Generally, Marcus theory considers transitions between diabatic potentials. Thermal (intramolecular) ET occurs between the ground states or after excitation as a follow-up process between excited states of a molecular donor (D) and an acceptor (A),

$$\mathrm{DA} \underset{k_{\mathrm{BET}}}{\overset{k_{\mathrm{ET}}}{\rightleftharpoons}} \mathrm{D^+A^-}. \tag{2.18}$$

with the ET rates k_{ET} and k_{BET} for the ET and the electron back-transfer, respectively. The energy enabling this process stems from random orientational fluctuations of the surrounding solvent molecules which is transferred back to the bath via relaxation after ET. Optically-induced CT processes directly lead to a charge-separated state after photon absorption,

$$\mathrm{DA} \xrightarrow{h\nu} \mathrm{D^+A^-}. \tag{2.19}$$

For a charge-separated state lower in energy than the excited state, a photoinduced ET can occur via relaxation of the excited state to the charge-separated state after absorption of a photon,

$$\mathrm{DA} \xrightarrow{h\nu} (\mathrm{DA})^* \rightarrow \mathrm{D^+A^-}. \tag{2.20}$$

In this case of ET, the excitation can either be localized on the D or A moiety. The charge recombination (CR) after optically and photoinduced ET occurs thermally.

In Marcus theory, the overall potential energy surface (PES) is reduced to parabolic potentials for both the reactant and the product state of DA among the electron-transfer coordinate

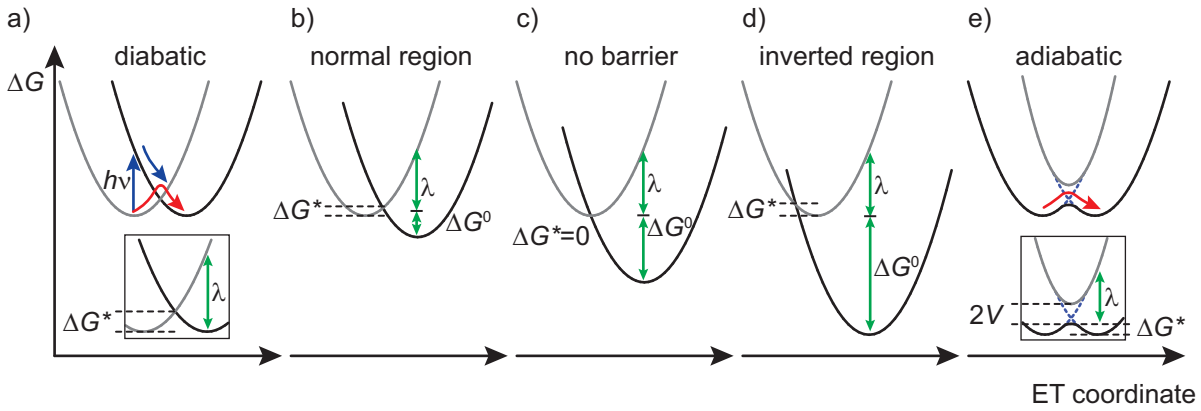

Figure 2.6: Diabatic and adiabatic potentials for electron transfer. a) The diabatic electron transfer between a donor (gray parabola) and an acceptor (black parabola) can occur either photoinduced (blue arrows) or thermally (red arrow). The energy barrier for electron transfer is given by ΔG^*, the reorganization energy by λ. b) For non-degenerate parabolas the difference in free energy between the donor and the acceptor is denoted with ΔG^0. In the Marcus normal region, $\Delta G^0 < \lambda$. c) In the optimal region, the barrier for electron-transfer vanishes due to an increased driving force for the electron transfer ($\Delta G^0 = \lambda$). d) For a further increased driving force, $\Delta G^0 > \lambda$ and the activation barrier increases again. e) For adiabatic potentials, a discrimination between a donor and acceptor parabola is not possible anymore. The separation in energy between the adiabatic potentials is $2V$. Note that both a) and d) show insets to clarify the values of λ and ΔG^*.

(Fig. 2.6). For an electronic coupling V between the donor and the acceptor smaller than the thermal energy ($V < k_B T$, with the Boltzmann constant k_B and the absolute temperature T) the electron transfer is diabatic (Fig. 2.6a–d), i.e., the donor and the acceptor state are spatially localized. For a coupling $V > k_B T$, the electron transfer is adiabatic (Fig. 2.6e) with a partially delocalized electron whose transfer is faster than the molecule's nuclear reorganization. With the difference of $2V$ between the minimum of the upper and the local maximum of the lower parabola (Fig. 2.6e), the barrier for adiabatic ET is about V higher than for the diabatic case. Assuming that both parabolas possess the same curvature, the activation barrier ΔG^* for the self-exchange reaction (Fig. 2.6a, red arrow) is given by the difference between the bottom of the parabolas and their intersection. The energy gap between the bottom of the reactant potential and the vertical position at the same reaction coordinate value in the product potential is the reorganization energy λ. The reorganization energy consists of two different contributions which are the inner or vibrational reorganization energy λ_i and the outer reorganization energy λ_o. The first contribution includes the changes of geometry in the molecular system when the electron is transferred. The second term accounts for the contribution of the solvent reorganization upon the modified charge distribution. The photoinduced CT is depicted with blue arrows in the case of the self-exchange (Fig. 2.6a). The whole reorganization energy is put into the system by excitation from the D potential to the A potential via absorption of a photon. Photoinduced CT can be described in terms of the Franck–Condon principle [61] but will not further be discussed in this thesis.

Calculation of Free Energies, Reorganization Energies, and Electron Transfer Rates

The rate k_{ET} for a thermally-induced ET [Eq. (2.18)] between two diabatic potential surfaces is given by an Arrhenius-type expression:

$$k_{ET} = k_0 \exp\left(-\frac{\Delta G^*}{k_B T}\right), \tag{2.21}$$

with the prefactor k_0 and the free energy of activation ΔG^*. The prefactor k_0 depends on different factors like the electronic coupling V and the vibrational frequency at the transition state of the ET. From geometric considerations, one can deduce the value for the activation barrier for harmonic parabolic potentials,

$$\Delta G^* = \lambda/4. \tag{2.22}$$

In the cases of non-degenerate reactant and product states (Fig. 2.6a–d), the thermodynamic driving force is the difference in free energy ΔG^0 between the minima of both potentials, leading to a modified expression of the activation barrier,

$$\Delta G^* = \frac{(\lambda + \Delta G^0)^2}{4\lambda}. \tag{2.23}$$

Equation (2.22) becomes the limit case of Eq. (2.23) for degenerate potentials. Inserting Eq. (2.23) into Eq. (2.21) yields the so-called Marcus equation for the ET rate,

$$k_{ET} = k_0 \exp\left(-\frac{(\lambda + \Delta G^0)^2}{4\lambda k_B T}\right). \tag{2.24}$$

Within the approach of Weller [62], the thermodynamic driving force ΔG^0 can be calculated as follows,

$$\Delta G^0 = \frac{N_A z e}{1000}\left(E_{1/2}^{ox} - E_{1/2}^{red}\right) - \frac{N_A e^2}{1000 \times 4\pi\epsilon_0}\left[\left(\frac{1}{2r_D} + \frac{1}{2r_A}\right)\left(\frac{1}{\epsilon_r} - \frac{1}{\epsilon_s}\right) + \frac{1}{\epsilon_s d_{DA}}\right], \tag{2.25}$$

with the number z of transferred electrons and the Avogadro number N_A. The potentials $E_{1/2}^{ox}$ and $E_{1/2}^{red}$ for oxidation of the donor and reduction of the acceptor, respectively, can be determined by electrochemical measurements. Hence, the permittivities ϵ_s and ϵ_r consider the solvent in which the electrochemical measurement is performed and the ET is studied. The donor and acceptor moiety are assumed to be spheres with the radii r_D and r_A. The separation between point charges D and A is taken into account by d_{DA}.

The free energy needed to transfer a charge in a dielectric medium, i.e., between D and A, is used as an estimate for the outer reorganization energy in the Born equation [60,63–65],

$$\lambda_o = \frac{e^2}{4\pi\epsilon_0}\left(\frac{1}{n^2} - \frac{1}{\epsilon_s}\right)\left(\frac{1}{2r_D} + \frac{1}{2r_A} - \frac{1}{d_{DA}}\right), \tag{2.26}$$

with n being the refractive index of the solvent.

The inner reorganization energy λ_i is independent from the solvent as only changes in bond lengths and angles contribute to it. Thus, for calculating the inner reorganization energies, well-established quantum-chemical calculation protocols can be used for the gas phase without solvation of the molecule. For cationic compounds exhibiting charge transfer the "neutral in cation geometry" (NICG) method can be applied [56]. In this approach, one assumes a degenerate dimer of the donor or acceptor subunit under consideration. For this dimer the geometry is optimized with quantum-chemical methods. Afterwards, the energy of the oxidized subunit is calculated by using the wavefunction of the neutral species for the cation and vice versa. When the concise values for electronic coupling and reorganization energies are taken into account, one gets a modified Marcus equation [63],

$$k_{ET} = 4\pi^2 hc^2 V^2 \sqrt{\frac{1}{4\pi\lambda_o k_B T}} \exp\left[-\frac{(\lambda_i + \lambda_o + \Delta G^0)^2}{4\lambda_o k_B T}\right]. \tag{2.27}$$

Different Marcus Regions

One of the unexpected and in the past strongly debated predictions of Marcus theory was the decrease of the ET rate for high thermodynamic driving forces ΔG^0. When ΔG^0 is increased, the intersection of the reactant and product parabola moves to smaller ET-reaction-coordinate values, simultaneously lowering the barrier for ET. Therefore, the ET rate gets larger. This ET region is called Marcus normal region ($-\Delta G^0 < \lambda$, Fig. 2.6b). When the activation barrier ΔG^* reaches the value of λ, i.e., when the product parabola intersects with the minimum of the reactant parabola (optimal region), the ET activation barrier vanishes and the ET rate reaches its maximum value without a barrier ($\Delta G^0 = \lambda$, Fig. 2.6c). For a further increased value of ΔG^*, the barrier gets larger again resulting in a decrease of the ET rate again ($-\Delta G^0 > \lambda$, Marcus inverted region, Fig. 2.6d). Therefore, Marcus theory predicts an inverted-region effect which was not expected from pure thermodynamic considerations. The activation barrier consists of two parts, only one of them being dependent on the reaction's thermodynamics. This means, from a certain point on, the intrinsic activation barrier is overcome and the inverted region is reached. Apart from its prediction in the 1950s it took about 30 years for the experimental confirmation of the inverted region effect on electron transfer [66].

2.5.2 Semiclassical Bixon–Jortner Theory

Although reproducing several experimental observations quite well, it was often observed that the inverted region is insufficiently described by Marcus theory. Especially the electron transfer rates were often underestimated by orders of magnitude. Therefore, numerous theoretical extensions have been made for a better description of ET. Bixon and Jortner proposed a diabatic approach based on a vibronic coupling model where the electronic coupling V is connected to the vibrational motion of the nuclei [56]. The Bixon–Jortner theory separates the inner and outer reorganization energy in two contributions. A high-energetic averaged mode $\tilde{\nu}_v$ represents the molecular vibrations whereas the classically treated solvent coordinate is described by a harmonic potential. The averaged molecular mode $\tilde{\nu}_v$ is treated quantum mechanically with the Huang–Rhys factor,

$$S = \lambda_i / \tilde{\nu}_v, \tag{2.28}$$

which replaces the Franck–Condon factor in a Golden-Rule-type expression [first term of the sum in Eq. 2.29)]. The Huang–Rhys factor is introduced for the sake of simplicity in ET rate calculations and represents the number of vibrations that are excited for one individual ET process. Hence, the semiclassical equation reads for the ET rate,

$$k_{\mathrm{CR}} = 4\pi^2 hc^2 V^2 \sum_{j=0}^{\infty} \frac{\exp(-S)S^j}{j!} \sqrt{\frac{1}{4\pi\lambda_{\mathrm{o}} k_{\mathrm{B}} T}} \exp\left[-\frac{(jhc\tilde{\nu}_v + \lambda_{\mathrm{o}} + \Delta G^0_{\mathrm{IVCT}})^2}{4\lambda_{\mathrm{o}} k_{\mathrm{B}} T}\right], \tag{2.29}$$

with the quantum number j representing the manifold of vibrations in the ET product state.

When the diffusive solvent motion is rate-limiting the ET one can modify Eq. (2.29) by introducing the longitudinal solvent relaxation time τ_{L} within the adiabatic parameter H_{A}[67],

$$H_{\mathrm{A}} = \frac{8\pi^2 hc^2 V^2 \tau_{\mathrm{L}}}{\lambda_{\mathrm{o}}}, \tag{2.30}$$

resulting in an extended formalism for the ET rate [68],

$$\begin{aligned} k_{\mathrm{CR}} &= 4\pi^2 hc^2 V^2 \sum_{j=0}^{\infty} \frac{\exp(-S)S^j}{j!} \sqrt{\frac{1}{4\pi\lambda_{\mathrm{o}} k_{\mathrm{B}} T}} \\ &\quad \times \exp\left(-\frac{(jhc\tilde{\nu}_v + \lambda_{\mathrm{o}} + \Delta G^0_{\mathrm{IVCT}})^2}{4\lambda_{\mathrm{o}} k_{\mathrm{B}} T}\right) \left(1 + H_{\mathrm{A}} \frac{\exp(-S)S^j}{j!}\right)^{-1}. \end{aligned} \tag{2.31}$$

Although the abovementioned theoretical approaches are purely diabatic in nature—apart from the adiabatic parameter in Eq. (2.30)—it has been shown that they suffice to describe systems which are rather adiabatic [69–71]. Thus, the considerations above are used in Chapter 4 to calculate ET rates for adiabatic systems as well.

2.6 Experimental Techniques

The fundamental experimental technique applied in this thesis is the study of light-induced molecular dynamics by transient absorption spectroscopy, which is a pump–probe technique applied in the condensed phase. In Section 2.1 a general introduction into ultrafast time-resolved spectroscopy was given with special attention on the signal detection in optical transient absorption spectroscopy. The subsequent Section 2.6.1 describes the steady-state absorption measurements and long-term irradiation experiments. Section 2.6.2 describes the experimental conditions for the experiments performed at 1 kHz repetition rate. Apart from a detailed overview of the setups for visible and mid-infrared probe detection also extensions for ultraviolet excitation and double-pulse excitation (pump–repump–probe spectroscopy), which were realized during this thesis, are described.

2.6.1 Steady-State Absorption and Irradiation Experiments

Steady-state absorption spectra were measured with a JASCO V-670 spectrometer in a spectral region from UV to NIR in quartz cuvettes of either rectangular or cylindrical shape (200 µm path length). The absorption spectra shown in Chapter 4 were measured with a similar device in the group of Prof. Lambert. In the case of all transient absorption experiments the

integrity of the samples was checked by UV/Vis steady-state absorption measurements before and after the time-resolved experiment. Fourier-transform infrared (FTIR) absorption spectra were recorded with a JASCO FT/IR-4100 spectrometer. Irradiation experiments (Chapter 6) are conducted with solutions in closed specimen jars ($\varnothing$ = 30 mm) irradiated with an array of light-emitting diodes (LED) with a maximum emission at 369 nm. The irradiated solution (about 40 ml) is continuously circulated with a peristaltic pump through a 200 μm path-length flow-through cuvette inserted into the spectrometer. Absorption spectra are taken for various irradiation times.

2.6.2 Ultrafast Spectroscopy at 1 kHz

The experiments performed at a repetition rate of 1 kHz were carried out with a commercial one-box amplifier system (Spectra-Physics, Solstice [72]). The oscillator (Spectra-Physics Mai Tai [73]) with a repetition rate of 80 MHz is pumped by a diode-pumped solid-state laser. The oscillator generates pulses around 800 nm having an average power of 10 nJ. About half of the output power is injected into the cavity of the amplifier by means of a Pockel's cell (electro-optic modulator, EOM) after pulse stretching. The amplifier is pumped by an intracavity-doubled diode-pumped neodymium-doped yttrium lithium fluoride (Nd:YLF) laser (Spectra-Physics Empower [74]) and are afterwards recompressed to a pulse length below 100 fs with a typical pulse energy of 3.5 mJ.

UV/Vis/NIR-Pump–Vis-Probe Transient Absorption Spectroscopy

Figure 2.7 gives an overview of the setup employed for the experiments conducted at 1 kHz with a whitelight supercontinuum as probe pulses. The setup built before [75,76] was utilized and expanded for UV-excitation during this thesis. The probe beam is generated by focusing a fraction (~1 µJ) from the amplifier with a lens (f = 75 mm) into a 5 mm CaF_2 plate. To avoid damages, the CaF_2 plate is horizontally moved on a linear translation stage. An iris is put in front of the focusing lens to adjust the beam diameter for optimal whitelight generation. The remaining fundamental part is filtered from the resulting whitelight probe with a "hot mirror" (HM, Thorlabs FM01). The probe beam is focused with a spherical mirror (f = 125 mm) into the sample flow-cell (200 µm path length, beam diameter 30 µm). After spectrally dispersing the probe beam in a spectrograph (Acton SP-2500), each probe spectrum is recorded with a charge-coupled-device (CCD) camera (Princeton Instruments Pixis 2K) at 1 kHz. The central wavelength of the pump beam can be chosen from the UV to the NIR spectral regime by different options. For all of them, the pump beam is delayed via a motorized linear delay stage (Newport M-IMS600LM) and mechanically chopped (New Focus 3501) at half the repetition rate (500 Hz). Hence, the difference spectra can be calculated on a shot-to-shot basis. The polarization of the pump and the probe beam is adjusted to the magic angle (MA) configuration (54.7°) by inserting a $\lambda/2$ plate in the respective pump beam. To avoid errors in the MA in noncollinear geometry [77] the 800 nm whitelight seed was turned to vertical polarization, i.e., perpendicular to the plane spanned by the overlapping pump and probe beam by means of a $\lambda/2$ plate. For NIR excitation, a fraction of the amplifier output is focused with an achromatic lens (f = 200 mm) into the sample (beam diameter 70 µm) and overlapped with the probe beam. For visible excitation, the output of a commercial NOPA (LightConversion,

TOPAS white) can be focused with a spherical mirror (f = 175 mm) into the sample cell (Fig. 2.7, green and dashed green from VIS1 on). For the option of UV excitation, the visible output is doubled in a BBO crystal (d = 100 µm, θ = 40.5°) placed shortly before the focal position of a reflective telescope (f_1 = 125 mm, f_2 = 125 mm). The unconverted visible part is filtered with a periscope high-reflective filter (LightConversion, HRs 275–350 nm and HRs 345–420 nm, according to the used pump wavelength). For switching between UV and visible excitation only small modifications have to be carried out. Mirrors VIS1 and VIS2 (Fig. 2.7) are replaced with mirrors UV1 and UV2 to guide the seed to the SHG-BBO and the UV output back into the pump path. The horizontal beam displacement by the filter can be readjusted by the mirrors afterwards to obtain the same focal position in the sample like with the visible pump. To adjust the focal position in direction of the beam, the focusing mirror is mounted on a linear translation stage. In the case of UV excitation, all pump mirrors after UV2 are replaced by aluminum coated mirrors which have a higher reflectivity than the silver mirrors used in the visible pump beam. The UV or visible pump beam is focused into the sample with a spherical mirror (f = 175 mm, beam diameter 100 µm) and overlapped with the probe beam. The temporal resolution of the setup was estimated from a fit of the coherent artifact from measurements of pure solvents [8] and is 115 fs or better for the whole probe-wavelength range with UV pump pulses at 260 nm and better than 120 fs for the 800 nm pump beam. The sample is circulated with a micro annular gear pump (mzr-4605, hnp Mikrosysteme GmbH) so that for each laser shot fresh sample is in the pumped region. Variable attenuator wheels in the visible and NIR beam allow the adjustment of the pump power used for different experiments.

UV-Pump–MIR-Probe Transient-Absorption Spectroscopy

For the transient absorption experiments with MIR probing (Fig. 2.8) the same laser system as for the visible probe pulses is used. The pump pulses are produced in another NOPA (Light-Conversion, TOPAS white) where the internal frequency doubling is used to produce UV pulses with pulse durations of about 50 fs. The UV pulses are focused with a spherical mirror (f = 125 mm) into a 100 µm flow-cell CaF_2-window cuvette (beam diameter 170 µm). To adjust the focal position of the pump pulse in beam direction, the focusing mirror is mounted on a linear translation stage. The sample is circulated with the same pump like in the visible-probe experiments. The MIR probe pulses (horizontally polarized) are generated in a MIR OPA [44,78] which was built earlier [79]. The fundamental 800 nm input beam is the residual beam from the NOPA after a fraction of its power was used to produce the pump pulses. By DFG of the signal and the idler output in a silverthiogallate ($AgGaS_2$) crystal, MIR pulses from 4 to 10 µm with a pulse energy up to 600 nJ can be produced. A germanium longpass filter (LPF, Fig. 2.8, 2 mm thickness) blocks the remaining signal and idler pulses not converted to the MIR. The MIR probe pulses are guided by means of gold coated optics and focused with a spherical mirror into the sample (beam diameter 120 µm). After passing the sample, the probe pulses are spectrally dispersed in a grating spectrometer (Chromex 250 is/sm spectrograph/monochromator) and detected with a liquid-nitrogen cooled 32-pixel Mercury Cadmium Telluride (HgCdTe) photodetector array for every laser shot. Since the pump beam is modulated with half of the repetition rate, difference spectra are calculated on a shot-

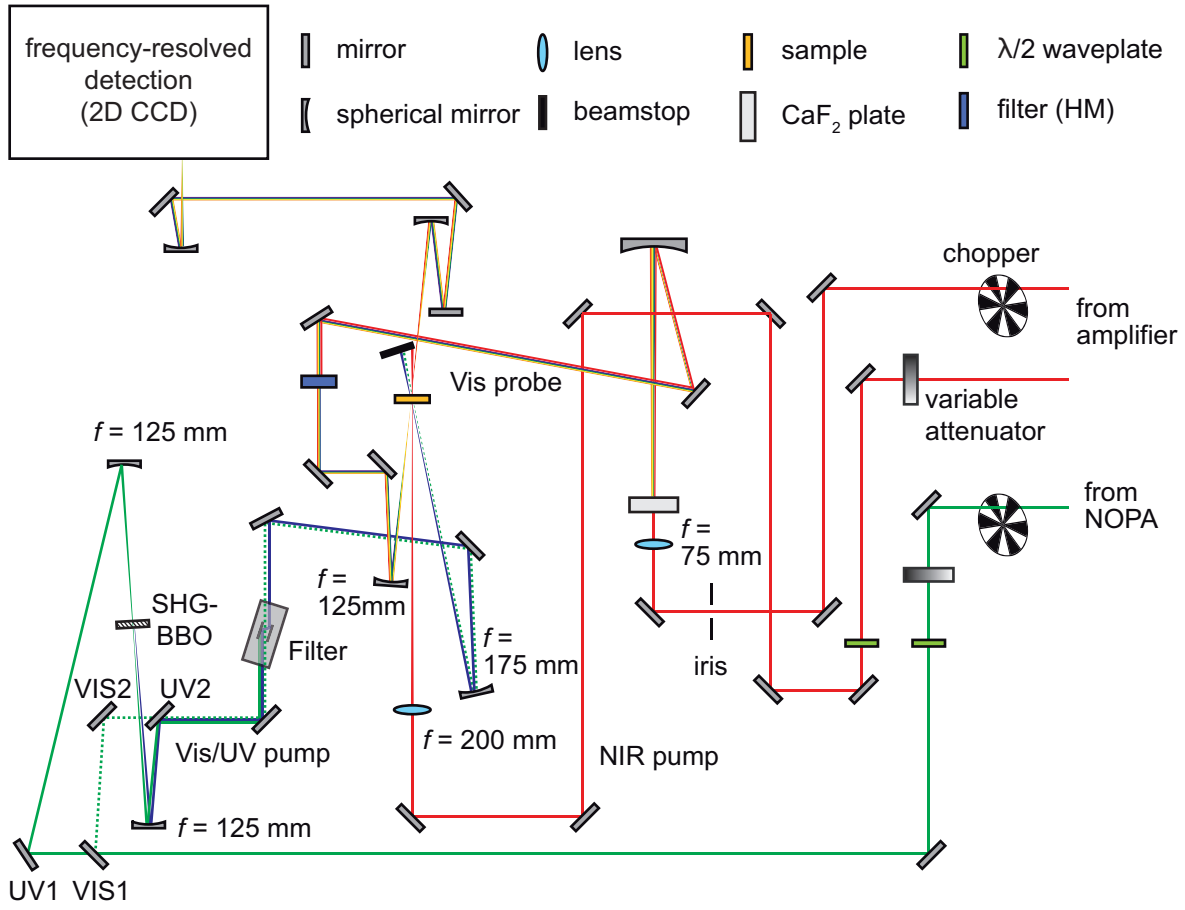

Figure 2.7: Topview of the UV/Vis/NIR-pump–Vis-probe setup, not to scale. The different options for the pump wavelengths are depicted in red (NIR pump), green (visible pump), and blue (UV pump), respectively. The broadband probe beam is drawn as a color continuum. The legend on top shows the used optical elements. Note that either the Vis (beam path via mirror Vis1) or the UV pump option (with SHG telescope and mirrors UV1 and UV2) can be used. See text for further explanations.

to-shot basis. With a $\lambda/2$ waveplate the pump polarization is rotated to achieve magic angle configuration. The temporal resolution of the setup was determined to be about 400 fs [9].

Setup for UV-Pump–UV-Repump Experiments

Experiments applying an additional pulse for dumping a molecular system to the ground state after evolving in the excited state were used to study molecular ground-state dynamics [80–82]. Pump–dump spectroscopy also allows to unravel the contributions of overlapping features in pump–probe spectroscopy when the course of a photochemical process is influenced by a change in the pump–dump delay time [80]. To study dark states which are not accessible by absorption of one pump photon [83, 84] or dynamics of higher-lying excited states, pump–repump–probe spectroscopy can be applied [85–87].

In the case of transient absorption spectroscopy, a second pump pulse, i.e., the repump pulse with a certain pump–repump delay time τ_{PR} is overlapped with the pump and the probe pulse in the sample. The repump pulse can either be a copy of the initial pump pulse (see below) or can

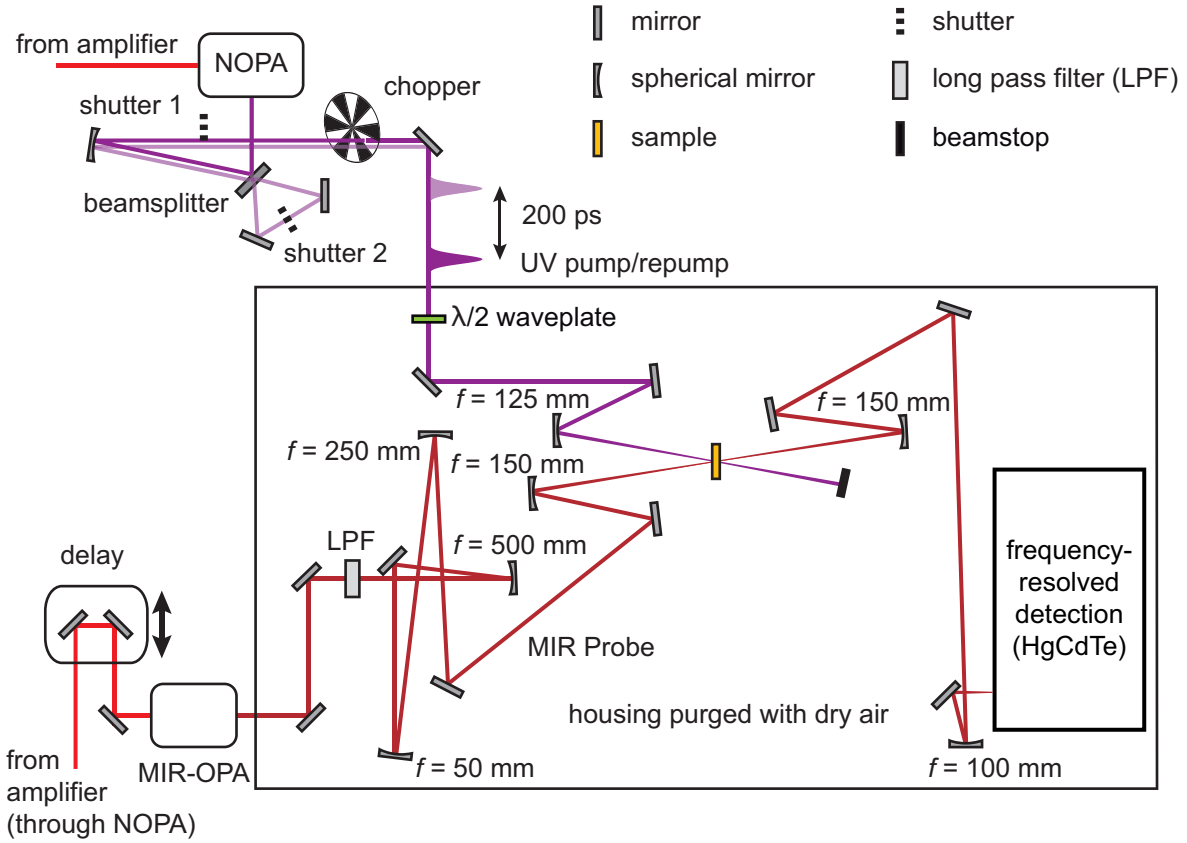

Figure 2.8: UV-pump–MIR-probe setup. The pump beam is depicted in violet, the MIR probe in dark red. The legend on top right shows the used optical elements. See text for further details. Adapted and extended from Ref. [9]. Copyright (2014) Dr. Philipp Rudolf.

be of different wavelength. By replacing one mirror in the pump path by a UV-beamsplitter (50% reflection and emission each) the pump beam can be doubled and recombined with the initial pump beam in an interferometer arrangement (Fig. 2.8). Both the pump and the repump beam (Fig. 2.8, dark violet and light violet) are guided almost collinearly through the mechanical chopper to the setup where both beams are overlapped with the MIR probe beam. Inserting a spherical mirror with a long focal length after the interferometer keeps the divergence of the pump and the repump beam small. Employing two shutters (Shutter 1 and Shutter 2, Fig. 2.8), either the pump, the repump, or both beams can be blocked independently. Therefore, it is necessary that pump and repump are not fully collinear. The changes in absorbance ΔA_P, ΔA_R, and ΔA_PR are calculated according to Eq. (2.3) for the case of either the pump, the repump or both pulses at the same time being present. The change in absorbance induced by molecules excited by both the pump and the repump pulses ΔA_diff is calculated by the difference of the combined signal and the two difference spectra for only one excitation pulse,

$$\Delta A_\mathrm{diff} = \Delta A_\mathrm{PR} - \Delta A_\mathrm{P} - \Delta A_\mathrm{R}. \tag{2.32}$$

With this extension, pump–repump–probe experiments can be performed with a fixed time delay τ_PR between the pump and repump pulse. In the case of the pump–repump experiments

described in Chapter 5, the delay time τ_{PR} was adjusted to 200 ps by the length of the interferometer pathway.

3 Development of 100 kHz Shot-to-Shot Broadband Data Acquisition

Parts of the project outlined in this chapter were conducted during the supervision of the Master thesis [88] of Sabine Keiber. The electronics for the high-speed chopper were designed and realized by Reiner Eck. The results presented here were already published in Ref. [4] and are reprinted with permission in Sections 3.1 to 3.4. Whereas in Section 2.1 the principles of data acquisition for transient absorption spectroscopy were already outlined, Section 3.1 of this chapter will give an introduction in different approaches to detect changes in absorbance in high-repetition-rate spectroscopy. It is shown in detail how broadband shot-to-shot data acquisition is developed for a repetition rate of 100 kHz to potentially reduce the measurement time by orders of magnitude compared to low-repetition-rate lasers. As a proof-of-principle experiment transient absorption spectroscopy on a laser dye is shown in Section 3.2. A detailed noise analysis is given in Section 3.3 emphasizing the advantages of high-repetition-rate data acquisition over averaging probe spectra before calculating ΔA. The chapter will be closed with an outlook on further possible improvements and adaptions of 100 kHz shot-to-shot readout to other experiments.

3.1 Experimental Realization of Mechanical Chopping at 100 kHz

High-repetition-rate lasers have the advantage of shorter measurement times for the same number of laser shots compared to experiments at low repetition rates. It was shown by Polack et al. that a 400 nm pump beam can be chopped by a mechanical chopper synchronized to a 100 kHz laser [89, 90]. A mid-infrared probe and reference beam were measured spectrally integrated with 100 kHz on two HgCdTe detectors. Using a lock-in amplifier the 50 kHz pump-beam modulation was filtered from the difference in the transmitted probe and the reference beam. The change in absorbance sent from the lock-in amplifier was averaged for 30,000 pulses. Spectrally resolved broadband shot-to-shot detection has only been reported for high-repetition-rate lasers up to 20 kHz [91]. This section demonstrates 100 kHz shot-to-shot broadband detection of transient absorption spectra by combining synchronized mechanical chopping of a 100 kHz laser and a commercially available fast CCD line camera.

For the experiments performed at 100 kHz repetition rate a commercial high-repetition-rate laser system was employed. The seed pulses for the amplifier are generated in a Ti:Sa oscillator (Coherent Mira 900 [92]) pumped by a fraction (~4.5 W) of the output of a 18 W diode-pumped solid-state laser (Coherent Verdi V-18 [93]). The oscillator pulses at 76 MHz repetition rate centered around 800 nm (FWHM = 12 nm) have a pulse duration of about 100 fs. Oscillator pulses with pulse energies of about 2 to 3 nJ are injected via an acousto-optic modulator ("cavity dumper") into the amplifier (Coherent RegA 9000 [94]) operating at 100 kHz. The Ti:Sa crystal of the regenerative amplifier is pumped by the remaining part (~13.5 W) of the pump laser amplifying the injected pulses by a factor of about 1000 in pulse energy. The amplified pulses are recompressed in the amplifier resulting in an output of 3 µJ with a pulse duration of about 170 fs.

The setup used in this thesis was employed in former studies with shutters to integrate the signal of many probe pulses on a charge-coupled device (CCD) [95–97] and modified for

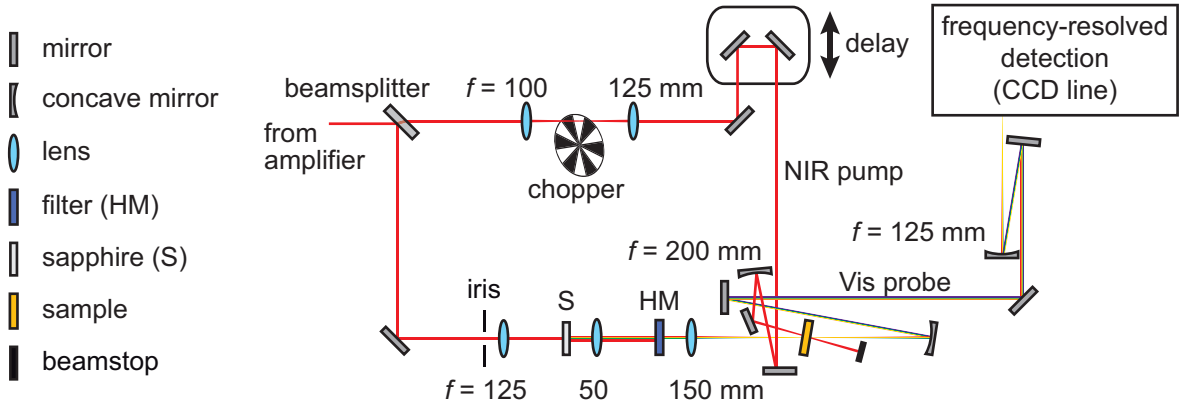

Figure 3.1: Topview of the layout of the NIR-pump–Vis-probe setup, not to scale. The near-infrared pump beam is depicted in red, the visible probe beam with a color continuum. The optical elements are described in the legend on the left and are further described in the text.

the demands of shot-to-shot readout. A topview of the setup used for transient absorption experiments at high repetition rate is given in Fig. 3.1. The output of the amplifier is split into two parts. One fraction ($\approx$ 30%)—the NIR pump beam (Fig. 3.1, red)—is sent through a telescope (f_1 = 100 mm, f_2 = 125 mm) with the chopper wheel placed in its focus. After passing the chopper unit the pump travels along a motorized linear delay stage (Newport M-IMS600LM) and is focused with a spherical mirror (f = 200 mm) into the 200 µm path-length flow-cell sample cuvette (beam diameter 210 µm). The major part of the amplifier output is adapted in beam diameter with an iris and focused (f = 125 mm) in a 1 mm sapphire plate to produce a whitelight supercontinuum probe beam. This whitelight continuum (Fig. 3.1, color continuum) is recollimated and the 800 nm fundamental part is reflected with a "hot mirror" (HM, Thorlabs FM01) transmitting the visible spectrum below 720 nm. The probe beam is focused with a lens (f = 150 mm) into the sample cell (beam diameter 160 µm) and overlapped with the 800 nm pump beam. Both beams are horizontally polarized. The sample is circulated with a micro annular gear pump (mzr-4605, hnp Mikrosysteme GmbH). The synchronized 100 kHz trigger signal (see below) is electronically gated to trigger the acquisition of i probe pulses (Fig. 2.2) with a fast CCD line camera (e2v AViiVA EM4, 1024 pixels, pixel size 14 × 28 µm) attached to a spectrometer (Acton SP-500, 150 g/mm grating blazed at 500 nm). Thus the spectrum of each single probe pulse is measured. As the pump beam is modulated with half the repetition rate (see below), the change in absorbance ΔA is calculated from the intensities for pairs of successive probe pulses according to Fig. 2.2 (inset) and Eq. (2.3) for the whole recorded spectrum.

For a shot-to-shot calculation of the change in absorbance ΔA the pump beam has to be blocked for every second pulse. In principle, this task can be approached in various ways. Acousto-optic modulators (AOMs) can be used to diffract into a slightly different direction every second pulse up to several hundred kHz repetition rates. The diffracted beam can then be used as the modulated pump beam. However, the dispersion added to the pulses in AOM crystals stretches the pulse length significantly. This issue can be overcome if acousto-optic programmable dispersive filters (AOPDFs) are used as the pulse can be compressed simul-

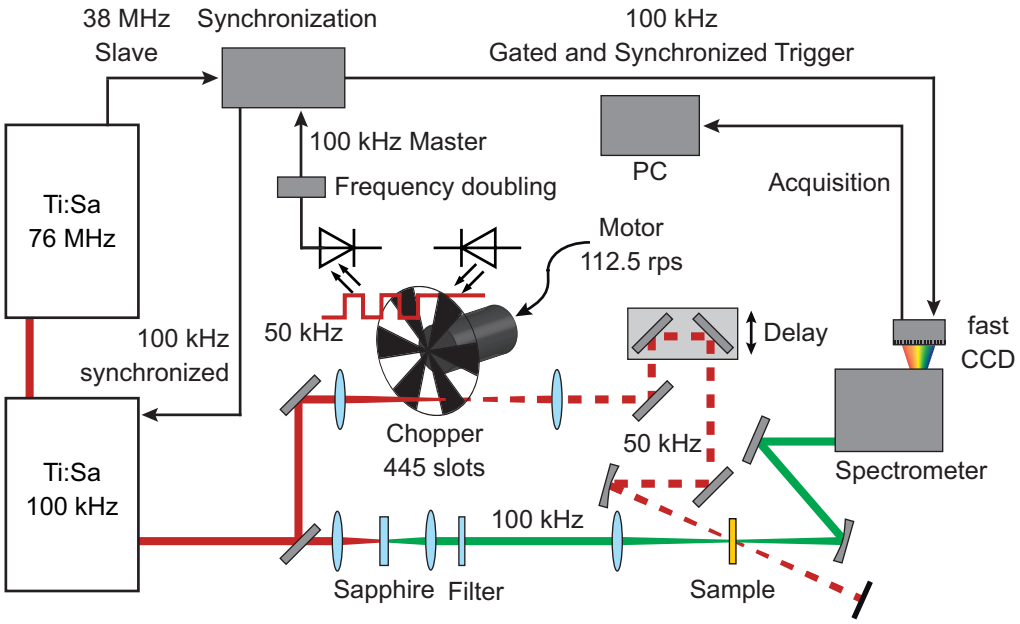

Figure 3.2: Experimental setup for 100 kHz shot-to-shot transient absorption spectroscopy. A light barrier attached to the chopper produces a 100 kHz master trigger which is synchronized to the trigger signal output of the oscillator. The amplifier is triggered by the synchronized trigger to ensure that only pulses matching the chopper wheel rotation are amplified. A detailed explanation is given in the text. A connectivity diagram of the synchronization box can be found in the Appendix A.1. Reprinted with permission from Ref. [4]. Copyright (2014) Optical Society of America.

taneously [98]. AOMs and AOPDFs are restricted to certain wavelength ranges depending on the used crystals. Another disadvantage is their relatively high cost.

For few-kHz lasers the use of commercially available mechanical chopper wheels is well established [15, 86, 99]. They can be triggered externally by the laser trigger. In that case, jitter of the rotation is so small that it does not affect correct chopping. With high motor turning speeds and an adequate number of slots in the chopping wheel chopping rates can be increased up to over 100 kHz. Pulse energy and pulse duration remain unaltered facilitating nonlinear processes for frequency conversion such as noncollinear optical parametric amplification (NOPA) at high repetition rates [100]. Appropriate laser synchronization is critical, however.

During this thesis, a high-speed mechanical chopper based on a brushless DC motor (Nanotec DB42M02) in combination with a programmable motion controller (Trinamic TMCM-171) was developed. The chopper unit is equipped with a commercially available chopper wheel (300D445, Scitec Instruments) with 445 slots of 340 µm in diameter to block every second pump pulse in the transient absorption setup operated with a 100 kHz laser. A detailed overview of the synchronization and detection circuitry is shown in Fig. 3.2. The required turning speed of about 112.5 rotations per second (rps) is set in the motion controller of the motor and controlled by a speed sensor at the rotation axis. Compared to few-kHz repetition rates, at a repetition rate of 100 kHz the jitter of the axis rotation gets critical, i.e., pulses might either be blocked or transmitted wrongly if laser and chopper are not perfectly synchronized. Since the chopper is a mechanically rotating disk, its moment of inertia makes rapid adjustments of

the chopper frequency challenging. Therefore, the laser was synchronized to the rotation frequency of the chopper rather than vice versa. A home-built light barrier at the chopper wheel generates a 50 kHz trigger representing the passage of slots in the chopper wheel. The 50 kHz trigger is doubled in frequency by adding a copy of itself with an adjustable delay resulting in the 100 kHz master trigger. The 38 MHz trigger output provided by the control unit of the Ti:Sa oscillator is electronically reduced to 100 kHz with a double "flip-flop" circuit, picking each first pulse coinciding with the master trigger ("Synchronization" in Fig. 3.2, for a connectivity diagram see Fig. A.1). Thus it is ensured that only oscillator pulses are injected by the cavity dumper of the amplifier which will thereafter pass a slot of the chopper wheel or will be blocked, i.e., pump pulses are neither wrongly blocked nor wrongly transmitted by the chopper wheel. The jitter of the chopper was determined to be below 1 µs. Anyhow, the jitter is not critical for the amplification because a Q-switch prevents lasing of the continuously pumped Ti:Sa crystal as long as no trigger pulse is sent from the chopper, i.e., as long as no oscillator pulse is injected into the amplifier cavity.

As already described above each probe pulse's spectrum is recorded with a fast CCD line camera. With the pump pulse being modulated at half the repetition rate, the change in absorbance ΔA is calculated for pairs of subsequent probe pulse pairs. The difference spectrum for each time delay τ is averaged for n pulse pairs. After acquisition of the averaged difference spectrum the delay stage is moved to the position corresponding to the next delay time τ. After scanning t delay times, the scan is repeated N times, averaging N difference spectra for each τ (Fig. 2.2).

As described in the next section, a transient absorption experiment is typically conducted with $k = 1$, $n = 500$, $t = 200$, and $N = 10$ (Fig. 2.2). For this set of acquisition parameters, the total measurement time is about 30 min, i.e., 3 min for one single transient map which is a measurement speedup by about a factor of > 3 compared to the 1 kHz transient absorption setup described in Section 2.6.2. For $N = 1$ ($i = 2 \times 10^5$) the overall probe pulse acquisition within the employed data acquisition program takes about 80 s. The 200 movements of the linear delay stage take about 90 s. In sum, the calculation and averaging of the change in absorbance in the measurement computer takes about 10 s for one set of delay times.

3.2 High-Repetition-Rate Shot-to-Shot Transient Absorption Spectroscopy

As a benchmark transient absorption spectroscopy on the laser dye IR 140 [101–103] dissolved in ethanol was conducted. When excited with pulses around 800 nm into the main absorption band (Fig. 3.3), IR 140 shows an ESA between 500 and 650 nm [102] whose maximum ($\lambda_{max} = 565$ nm) is attributed to S_1–S_n absorption [101]. The ESA decay is reported to be a biexponential process with a fast time constant of 1.96 ps and a slow time constant of greater than 100 ps [102]. For a monoexponential data analysis a decay time constant of 0.5 ns was obtained [101].

In the experiment presented, the pulse energy of the pump beam was adjusted to 186 nJ, the probe beam had a pulse energy of about 20 nJ. Due to a small remaining transmission of the fundamental beam through the hot mirror, a larger probe pulse energy was detected as the roughly 8 nJ expected from the maximum spectral density of whitelight generated in a

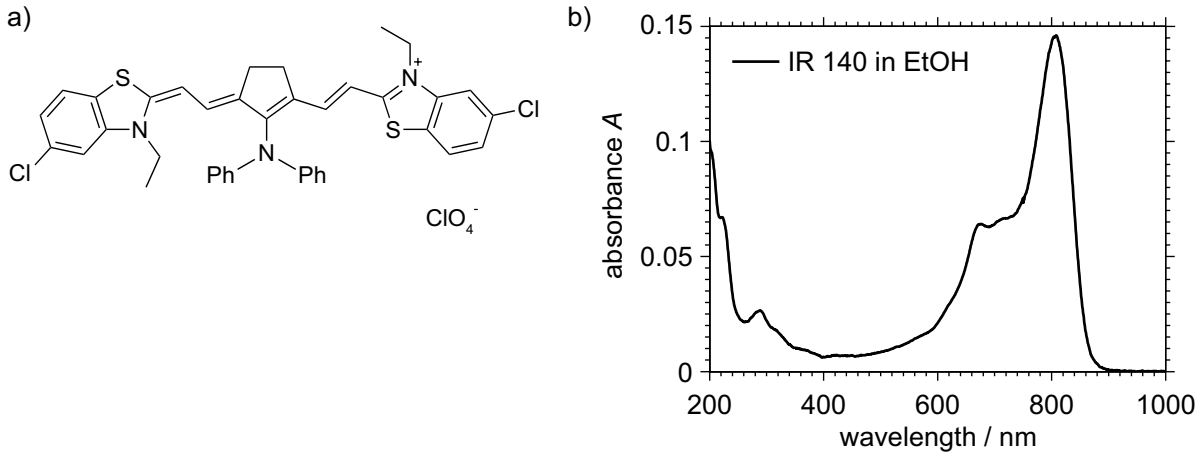

Figure 3.3: Properties of the laser dye IR 140. a) Molecular structure of IR 140. b) Absorption spectrum of IR 140 dissolved in ethanol (100 µg/ml, $d = 200\mu$m).

sapphire crystal [104]. Each recorded transient map consists of $t = 200$ delay time steps, split into 100 time steps of 50 fs from -2 ps to 3 ps and 100 logarithmically increasing time steps from 3 ps to 1.2 ns. The data was averaged for $k = 1$, $n = 500$, $t = 200$, and $N = 10$.

The result of the dynamics in a wavelength range from about 435 to 640 nm is shown in Fig. 3.4a in a delay time interval τ ranging from -0.25 to 1200 ps. For a two-exponential model in a global lifetime analysis a rising lifetime of $\tau_1 = 169$ fs reflecting the pump pulse length and a decaying lifetime of $\tau_2 = 620$ ps were obtained. Considering that in Ref. [102] data was fitted for single wavelengths only and in a limited temporal window of up to 300 ps these results are consistent with the literature [101, 102].

Figure 3.4b shows difference spectra for various delay times. The temporal evolution of the change in absorbance can be seen in Fig. 3.4c for a selection of probe wavelengths at 500, 540, and 565 nm. The recorded data (crosses) and the biexponential global fit (dashed lines) agree very well, demonstrating high signal-to-noise ratio and thus the feasibility of significantly reduced total measurement time using 100 kHz shot-to-shot detection.

In general, for all high-repetition-rate pump–probe experiments—regardless of the detection technique—the exchange of the excitation volume has to be considered for every studied molecular system [91]. Uncomplete sample exchange might lead to an offset signal for decay lifetimes larger than the repetition rate's periodic time (in this case $\tau \geq 10\,\mu$s). If dynamics of chemical reactions are studied, the excitation energy has to be kept low, which is an intrinsic advantage of high-repetition-rate lasers, so that distortion of the measured signal by photoproduct absorption generated by the previous pump pulse is minimized.

3.3 Noise-Level Analysis

In spectroscopic measurements several different noise sources can contribute. Here, electronic noise of the camera, shot noise, and laser fluctuation are considered. Their effects on the error of ΔA are calculated by error propagation and summarized in Table 3.1.

The overall electronic noise contribution of the camera, e.g., basically read-out noise, is 7.7 LSB (least significant bit), corresponding to 7.7 counts. An average count rate at 70% of

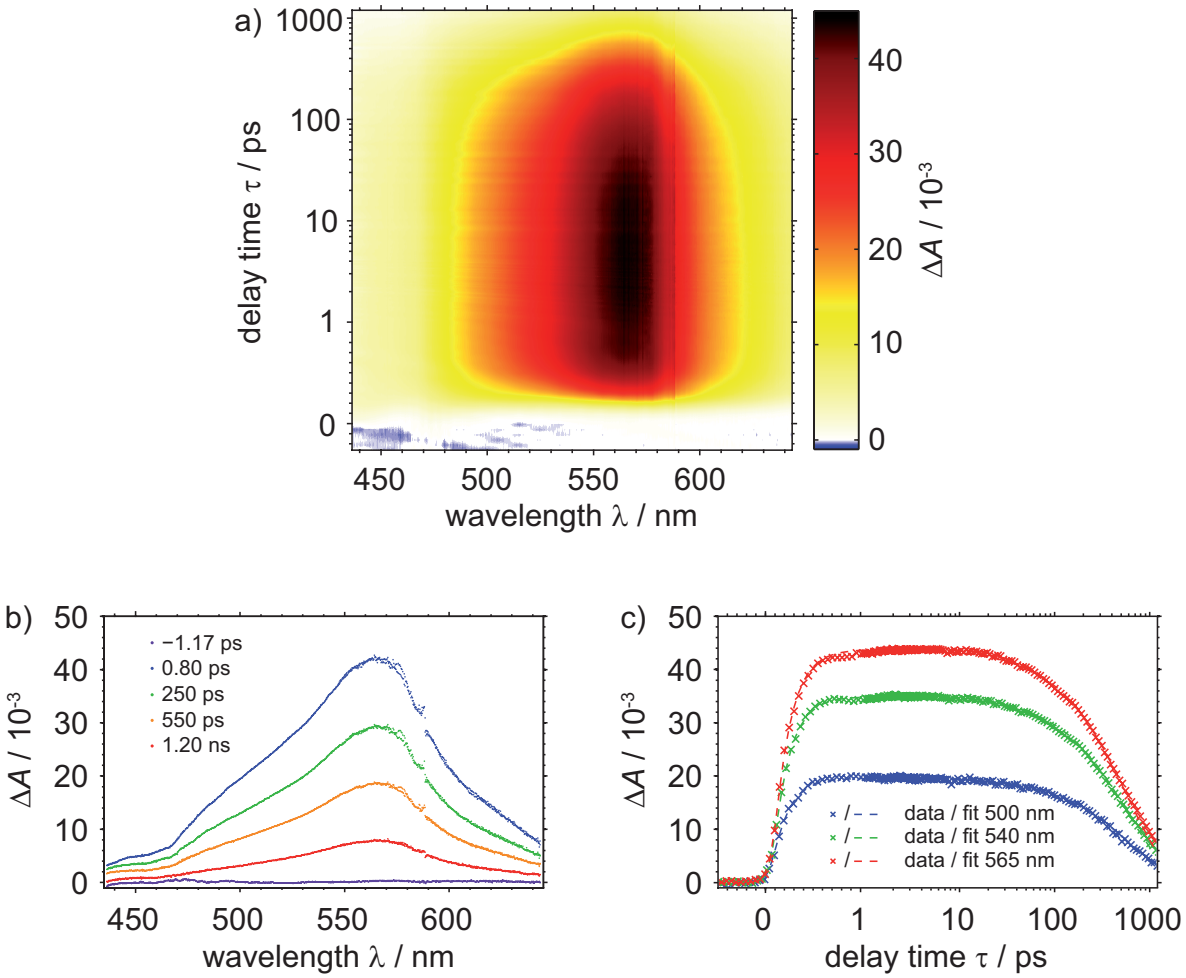

Figure 3.4: Transient absorption data of IR 140 in ethanol measured shot-to-shot at 100 kHz repetition rate. a) The transient map was recorded with excitation at 800 nm and a sapphire whitelight probe continuum. Data was averaged for $k = 1$, $n = 500$, $t = 200$, and $N = 10$. Note that the delay time axis changes from linear to logarithmic scaling for $\tau > 1$ ps. b) The ESA can be seen in the difference spectra for various delay times. The spike in all difference spectra around 590 nm originates from a dip in the whitelight probe spectrum. c) The dynamics of the ESA are shown by transients for three different wavelengths. The dashed lines indicate the results of a global lifetime analysis. Adapted with permission from Ref. [4]. Copyright (2014) Optical Society of America.

the full dynamic range of the 12-bit ADC, i.e., 0.7×2^{12} counts = 2870 counts, is considered. This leads to a relative error of 2.68×10^{-3}. The shot noise due to Poissonian statistics is the square root of the number N_{Ph} of incident photons on the detector. For an average detector quantum efficieny of 0.75 in the wavelength range from 430 to 700 nm and again an exploitation of 70% of the pixels' wells (full well capacity = 2.38×10^5 electrons per pixel), $N_{\mathrm{Ph}} = (0.7/0.75) \times 2.38 \times 10^5 = 2.22 \times 10^5$. Therefore, the relative error due to shot noise (shot-noise limit) is $1/\sqrt{N_{\mathrm{Ph}}} = 2.12 \times 10^{-3}$. To estimate the laser fluctuations, subsequent probe pulse intensities I_0 on one pixel of the fast CCD line camera were recorded at 537.4 nm. The measured intensity values contain errors from the other noise contributions as well. However, as can be seen from Table 3.1, the different noise contributions are significantly smaller

Table 3.1: Noise contributions and error for the calculated change in absorbance ΔA. Adapted with permission from Ref. [4]. Copyright (2014) Optical Society of America.

	noise contribution		
	electronic noise	shot noise	laser fluctuations[a]
value	$I_0 = 2870$ counts	$N_{\mathrm{Ph}} = 2.22 \times 10^5$	$I_0 = 2870$ counts
error	7.7 LSB[b] $\hat{=}$ 7.7 counts	$\sqrt{N_{\mathrm{Ph}}} = 471$	$\Delta I_0 = 35$ counts
relative error	2.68×10^{-3}	$1/\sqrt{N_{\mathrm{Ph}}} = 2.12 \times 10^{-3}$	1.22×10^{-2}
error[c] of ΔA	1.65×10^{-3}	1.30×10^{-3}	7.49×10^{-3}

[a] values for single pulses at 537.4 nm; [b] least significant bit; [c] after error propagation

than the error for the measured intensities, i.e., the intensity fluctuations are a direct measure of the laser fluctuations. For an average count number of 2870, the absolute error of the probe pulse intensity is about 35 counts, i.e., the relative error is 1.22×10^{-2}. Assuming uncorrelated intensity values I and I_0, error propagation of the ΔA calculation according to Eq. (2.3) leads to the absolute errors of ΔA shown in the last row of Table 3.1. The laser fluctuations clearly dominate over the other noise contributions, which has been shown earlier for 1 kHz lasers [105]. For the 12-bit digitizer, the maximal detection sensitivity for ΔA (resulting from a pump-induced change in the probe intensity count rate of 1 bit) at 70% of saturation is $\lg[0.7\times2^{12}/(0.7\times2^{12}-1)] = 1.51\times10^{-4}$ and hence below the noise contributions. Considering the results from Table 3.1, it becomes clear that reducing the influence from laser fluctuations has the strongest impact among the various noise contributions on the overall signal-to-noise level. Thus the order of the averaging and recording procedure (Fig. 2.2) becomes relevant and shot-to-shot detection advantageous.

To test the effect of the reduced shot-to-shot measurement time on the signal-to-noise ratio compared to an acquisition method with $k \gg 1$, a noise-level analysis was performed. Shot-to-shot detection is advantageous for ~1 kHz-repetition-rate lasers because subsequent laser pulses are strongly correlated. For a shot difference greater than one laser pulse the correlation rapidly decreases [106]. In order to find out whether this correlation also holds for whitelight supercontinuum probe pulses at 100 kHz, i intensity values I_0 were recorded on one pixel of the fast CCD line camera corresponding to a wavelength of $\lambda = 537.4$ nm. The noise-frequency contributions f for a series of i pulses are given by the absolute value of the Fourier transform $\mathcal{F}$ of the intensities $I_{0,m}$ with $m = 1, 2, \ldots, i$:

$$f = |\mathcal{F}\{I_{0,1}, I_{0,2}, \ldots, I_{0,i}\}|. \tag{3.1}$$

In this measurement the chopper is only used for generating the master trigger, but neither the pump pulses nor the sample cuvette are used.

It has previously been shown that low-frequency contributions dominate the noise characteristics of few-kHz lasers [105,107]. Also for the 100 kHz laser used here the noise is dominated by low-frequency contributions ranging up to roughly 1 kHz (Fig. 3.5a). Therefore calculation of the change in absorbance by averaging I_p and I_u for $k \gg 1$ probe pulses is unfavorable, and shot-to-shot data acquisition ($k = 1$) should be advantageous also for high-repetition-rate lasers.

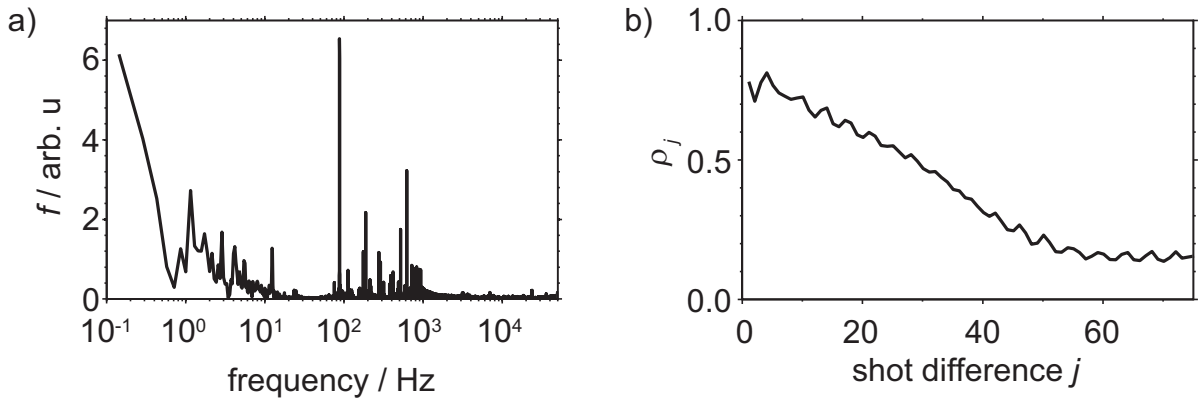

Figure 3.5: Noise and correlation analysis at 537.4 nm. a) The Fourier transform f of $i = 7 \times 10^5$ intensities $I_{0,\,m}$ on one pixel for subsequent probe pulses reveals dominant low-frequency contributions up to roughly 1 kHz. b) The high correlation between probe pulses calculated for $i = 2^{15}$ decreases for greater temporal spacing. Adapted with permission from Ref. [4]. Copyright (2014) Optical Society of America.

The statistic autocorrelation ρ_j was also calculated for a series of i probe pulses,

$$\rho_j = \frac{1}{\sigma^2 i} \sum_{m=1}^{i-j} [(I_{0,\,m} - \mu)(I_{0,\,m+j} - \mu)], \tag{3.2}$$

with $j = 0, 1, 2, \ldots, i-1$, where σ^2 is the variance and μ is the mean value of the intensities $I_{0,\,m}$. The statistic autocorrelation is shown in Fig. 3.5b for a wavelength of 537.4 nm and a sequence of $i = 2^{15}$ probe pulses. It can clearly be seen that with the employed 100 kHz laser successive pulses are strongly correlated. The correlation drops within $\approx$ 50 pulses. This directly shows that measurement with $k = 1$ is superior to $k \gg 1$ and therefore, the estimated error of ΔA from Table 3.1 can be reduced.

To quantify the advantage of shot-to-shot detection ΔA was calculated via Eq. (2.3) for one CCD pixel but without any pump beam present. Ideally this should lead to $\Delta A = 0$, with the remaining signal indicating the noise floor. Two different situations are compared: the "conventional" measurement scheme by emulating a CCD camera with 1 ms readout time via averaging over $k = 100$ shots (Fig. 3.6, blue); and the new shot-to-shot measurement scheme using $k = 1$ (Fig. 3.6, green). As shown above (Table 3.1), laser noise is the limiting factor in the calculation of ΔA and other noise contributions can be neglected for the comparison of different acquisition and averaging schemes. Using just one sequence $n = 1$ for each "time step" (Fig. 3.6a), the standard deviation σ of ΔA is comparable for both scenarios, even though the shot-to-shot technique (green, $\sigma = 2.96 \times 10^{-3}$) uses 100 times fewer pulses than the conventional scheme (blue, $\sigma = 2.34 \times 10^{-3}$). The error of the shot-to-shot detection is about as large as estimated from error propagation in Table 3.1. Shot-to-shot detection thus has the potential to be 100 times faster than $k \gg 1$ averaging at comparable signal-to-noise ratio.

Comparing the same acquisition time, i.e., the same number ($i = 1000$) of acquired pulses (Fig. 3.6b), the standard deviation for shot-to-shot detection ($k = 1$, $n = 500$, green, $\sigma = 1.2 \times 10^{-4}$) over $t = 200$ delay times is about a factor of 3 smaller than for $k = 100$ ($n = 5$,

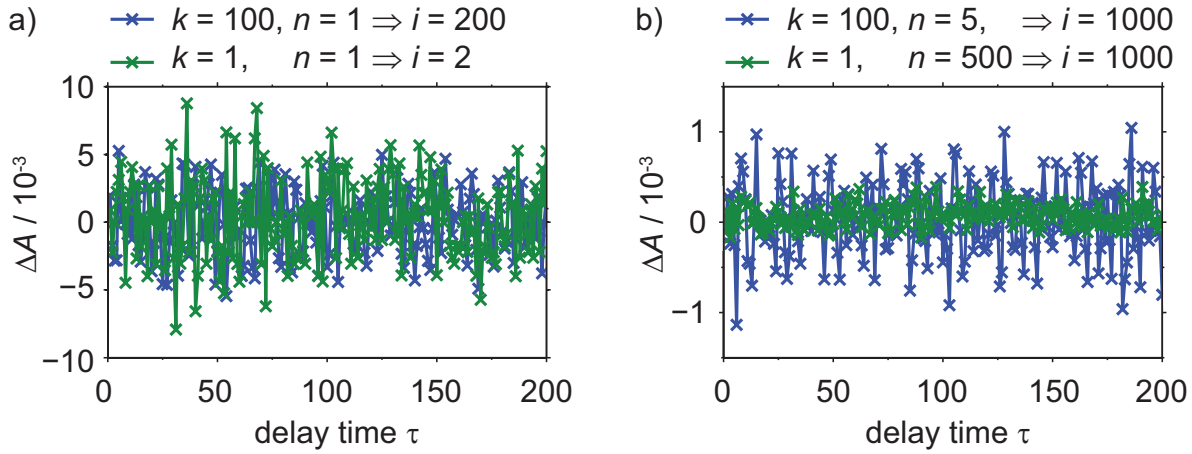

Figure 3.6: Comparative noise-level analysis for $k = 100$ and $k = 1$ (shot-to-shot). a) For a single calculation of ΔA ($n = 1$) for each delay time τ the noise level is equivalent for ($k = 100$, $i = 200$) and ($k = 1$, $i = 2$). b) For the same number of acquired pulses ($i = 1000$) the noise level is about a factor of 3 smaller for $k = 1$ than for $k = 100$. Adapted with permission from Ref. [4]. Copyright (2014) Optical Society of America.

blue, $\sigma = 4.1 \times 10^{-4}$). Additional improvement on the signal-to-noise ratio could be achieved by even shorter measurement times and more efficient averaging for the given pulse correlation in the fast-scan measurement scheme [108,109].

Even though this comparison does not take into account any error contribution from the pump pulse, it is obvious that averaging over shot-to-shot ΔA values results in either significantly reduced total measurement time (Fig. 3.6a) or superior data quality (Fig. 3.6b) for optical pump–probe experiments.

3.4 Conclusion and Outlook

Using a home-built mechanical chopper the pump beam in an optical pump–probe experiment could be modulated with half of the laser's repetition rate of 100 kHz. Synchronization was achieved by using the chopper as a master trigger for the laser amplifier. Hence jitter in the chopper rotation frequency is not critical. A fast CCD line camera made it possible to measure the spectrum of every probe pulse at the rate of 100 kHz. The capabilities of high-repetition-rate shot-to-shot detection was demonstrated on the transient absorption of IR 140 in ethanol.

The high-repetition scheme considerably decreases the total measurement time required for reaching a particular noise level, potentially by two orders of magnitude when changing from 1 kHz to 100 kHz readout. The maximum speedup may be limited by the reaction time of the linear delay stage, but the potential for measuring quickly decomposing or sensitive samples such as biological complexes is obvious [99]. Another advantage is that kinetic processes like aggregate formation or kinetically oscillating reactions could be studied.

With further improvement of fast CCD devices shot-to-shot data acquisition might be possible for repetition rates higher than 100 kHz, e.g., 250 kHz, which is also common for high-repetition-rate amplified lasers. Adapting the scheme for data acquisition in coherent multidimensional spectroscopy should be straightforward.

In addition to the improvement of data acquisition, tandem pumping the amplifier with three independent pump lasers could minimize laser fluctuations leading to even better data quality [91]. Implementation of parallel data acquisition in the employed program environment would allow a continuous movement of the stage while data could be taken on-line [108,110], even faster with a delay stage capable for fast-scan measurements [109]. Hence, the overall measurement time could be further reduced.

As another aspect of speeding up the measurement time, the duty cycle (DC) for the calculation of ΔA from a series of $2n$ probe pulses can be improved. The DC is calculated by the ratio of ΔA values calculated per pulse, i.e., for the presented shot-to-shot approach by $\mathrm{DC} = n/2n = 0.5$. When every third pump pulse is blocked, e.g., with a chopper wheel possessing slots twice as large as the lands, each blocked pump pulse can be used for calculation of ΔA twice by using the preceding and the subsequent pulse [111]. For an averaging scheme with every third pump pulse blocked and a series of $2n + 1$ pulses being a multiple integer of 3, the DC increases to $2/3$.

4 Ultrafast Optically-Induced Electron Transfer in Donor–Acceptor Oligomers

The work presented in this chapter is the fruit of a cooperation with the research group of Prof. Dr. Christoph Lambert. The synthesis of the investigated compounds was described in the Diploma thesis of Han Lu [112]. Steady-state absorption spectra and electrochemical measurements were performed in the group of Prof. Lambert. Calculations except the calculations of activation barriers, free energies and lifetimes were carried out by Dr. Marco Holzapfel. The results have been published in Ref. [5] and are reprinted with permission in Sections 4.1 to 4.6.

Charge transfer (CT) is a process accompanying most chemical reactions and is driving many natural and technological processes. Therefore, CT is interesting to study for gaining insight into reaction mechanisms and functionality, both in natural and artificial systems. The overall aim of this thesis was to gain insight into the underlying processes and dynamics of chemical reactions, i.e., the study of CT processes is among the molecular events with great significance to that issue.

The first section gives an overview of charge and electron transfer (CT and ET) in different donor–acceptor systems from macro- and microscopic points of view. In Section 4.2 the spectral properties of the investigated compounds are discussed. The ultrafast time-resolved CT properties are presented in Section 4.3 and are further discussed in Section 4.4. Theoretical calculations of CT rates and activation barriers are demonstrated in Section 4.5 for a deeper understanding of the basic CT processes in donor–acceptor oligomers. Section 4.6 summarizes the results with indications of possible future experiments.

4.1 Donor–Acceptor Compounds for Charge- and Electron Transfer Studies

Light-induced charge and electron transfer (CT and ET) processes are ubiquitous in nature as well as in technological devices. The most prominent examples are photosynthesis, photovoltaics and optoelectronics. Well-grounded knowledge about the transfer and separation of charges is of utmost importance to understand and design the efficiency and function of these devices. That is why CT is studied in a large number of natural [113–120] and artificial systems [56, 121–127]. Short-living intermediates can be tracked by means of ultrafast femtosecond spectroscopy to study the microscopic dynamics of charge separation, propagation, and recombination [1, 68, 128–130]. The concept of two-dimensional spectroscopy has also been employed to study CT processes [131,132]. Contrary to that, macroscopic measurements of CT can be carried out by charge-carrier mobility measurements [133–136] where a galore of microscopical dynamic steps are averaged over on a longer distance to result in a macroscopic quantity. Up to date, the most challenging part is to close the gap between microscopic ultrafast CT dynamics and macroscopic charge-carrier mobilities. This is even more desirable as then the so far unsuccessful prediction of a device's efficiency from the material's properties could be come closer.

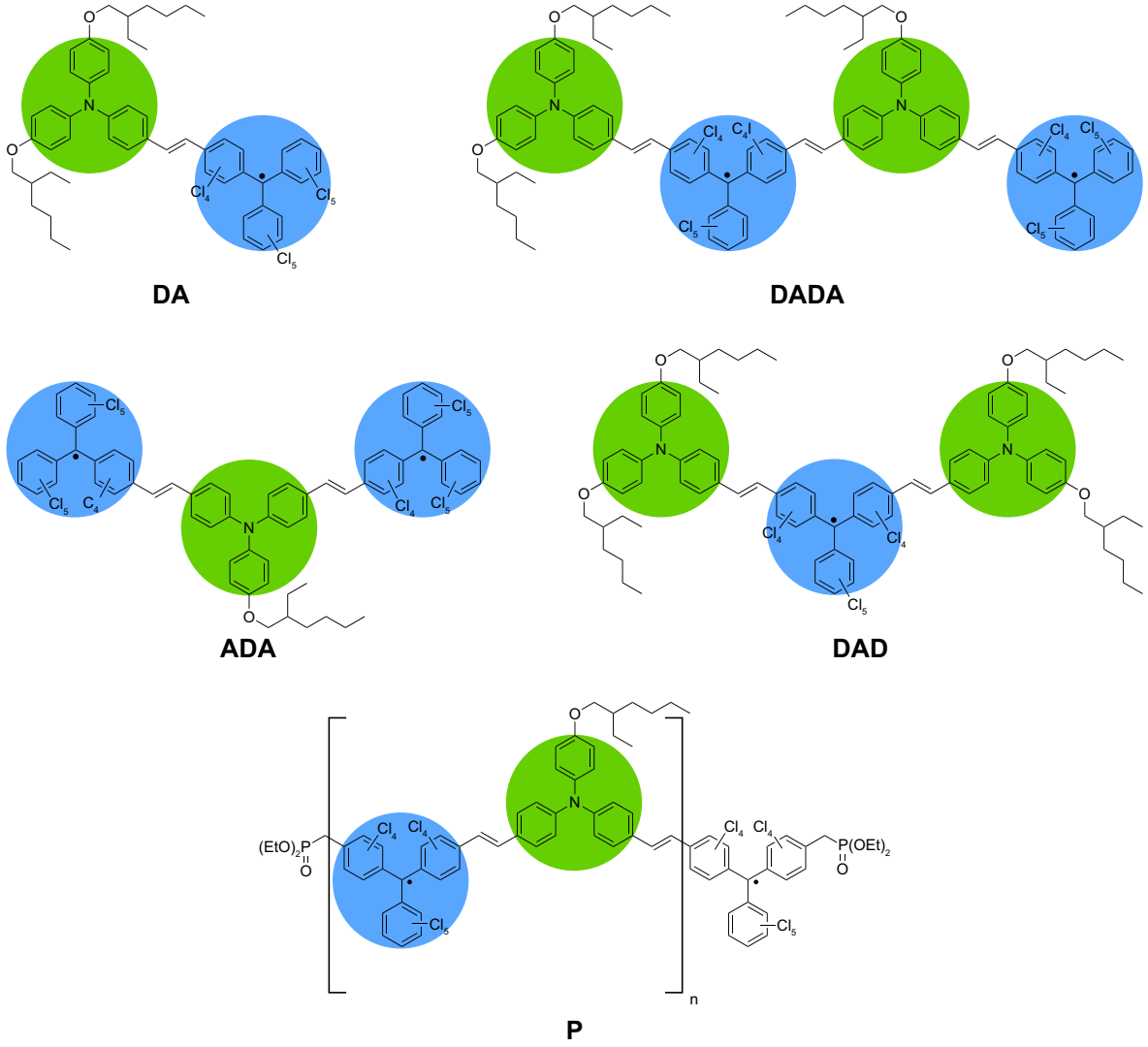

Chart 4.1: Donor (**D**, green)–acceptor (**A**, blue) oligomers and polymer **P** investigated in this work. Adapted with permission from Ref. [5]. Copyright (2014) American Chemical Society.

To address the abovementioned challenge the aim of the work presented here was the determination of charge separation on a longer distance. More precisely, the question was how for apart charges separate on a given linear array of alternating donors (**D**) and acceptors (**A**). In these systems, the initial optically-induced CT occurs from one donor moiety to a neighboring acceptor unit. To find out how far the charges then separate and which processes either lead to charge recombination (CR) or charge transport, several **D**–**A** oligomers [112] were studied as confined one-dimensional arrays by means of transient absorption spectroscopy in solution. The oligomers possess different lengths, i.e., whether charge separation occurs from a certain chain length on should be detectable by a decrease in the CR dynamics for the corresponding compound. Since this observation was made earlier in a polymeric **DA** compound [1,97,137] the outcome of the oligomer measurements is compared to these results.

The studied compounds are depicted in Chart 4.1. The constituting parts are perchlorotriphenyl methyl radicals (PCTM) [138] as acceptor (**A**) units and triarylamines (TAA) [1,69,70,

139] as donor (**D**) units. PCTM units are radicals stabilized by the electron-withdrawing effect of the perchlorination of the aromatic substituents. TAA moieties are synthetically well accessible electron donors whose redox properties can be tuned by the substitution of the aryl rings. The combination of the two building blocks PCTM and TAA results in compounds with a low band gap around 1 eV what makes them interesting materials for all sorts of photovoltaic applications. Belike the most advantageous properties of TAA–PCTM compounds is their charge neutrality compared to numerous other mixed-valence (MV) compounds. This makes them better soluble and more stable compared to their charged analogues [56]. In a number of studies the ET properties of different TAA–PCTM **D–A** systems have been investigated. What they all have in common disregarding the substituent at the donor or the bridge between **D** and **A** is an ultrafast optically-induced ET from the TAA to the PCTM moiety leading to a zwitterionic intermediate consisting of a triarylamine radical cation ($TAA^{+\bullet}$) and a perchlorotriphenyl methyl anion ($PCTM^{-}$) [1,68,128]. This optically-induced charge transfer is called "intervalence charge transfer" (IVCT). The subsequent electron back-transfer is then accomplished thermally. A fast CT with a slower CR is assumed as the inner reorganization energy within TAA–PCTM compounds is rather small (see below). Thus, the fast ET takes place in the normal Marcus region whereas the electron back-transfer is slower due to an enhanced activation energy in the inverted region (Section 2.5.1). A change in the substituents at the donor unit in a directly coupled TAA–PCTM monomer showed that the free energy ΔG^0 decreases with increasing donor strength, i.e., with increasing difference in the cyclovoltammetric redox potentials [56,139].

Linear absorption spectra, cyclic voltammograms, differential pulse voltammetry as well as spectroelectrochemical measurements on the series of the oligomers **ADA**, **DAD**, the reference monomer **DA**, and its dimer **DADA** have been measured in the group of Prof. Lambert and are published in Refs. [5,112]. These data are of great importance for the interpretation of the transient absorption data presented in Section 4.3 and basis of the calculations in Section 4.5.

4.2 Spectral Properties of Donor–Acceptor Oligomers

The series of **DA** compounds studied in this thesis were measured both in dichloromethane (DCM) and toluene. Hence, Figs. 4.1a–c show the steady-state absorption spectra of **ADA**, **DAD**, and **DADA** both in DCM and toluene. The linear absoprtion of all four oligomers can be found in Fig. 4.1d in toluene solution. For all compounds, three bands can be spotted in both solvents. The band around 35000 cm^{-1} (286 nm) can be assigned to transitions localized at the donor moiety [140]. On the other hand, the band around 25000 cm^{-1} (400 nm) is due to transitions on the acceptor moiety [141]. The third band around 12000 cm^{-1} (NIR spectral region) is assigned to an IVCT [55,56]. Spectroelectrochemical measurements show absorption spectra of the oxidized or reduced compound studied and look rather similar for all four **DA** oligomers [5]. Upon oxidation two new absorption bands were detected. The new band around 9000 cm^{-1} (1100 nm) on the red edge side of the IVCT band is attributed to an electron transfer from the acceptor PCTM to $TAA^{+\bullet}$ [69]. The second band around 14200 cm^{-1} (704 nm) stems from a localized transition at the oxidized donor [140]. The reduced donor $PCTM^{-}$ exhibits a localized transition which leads to the appearance of a new band around 18000 cm^{-1} (556 nm) [142,143].

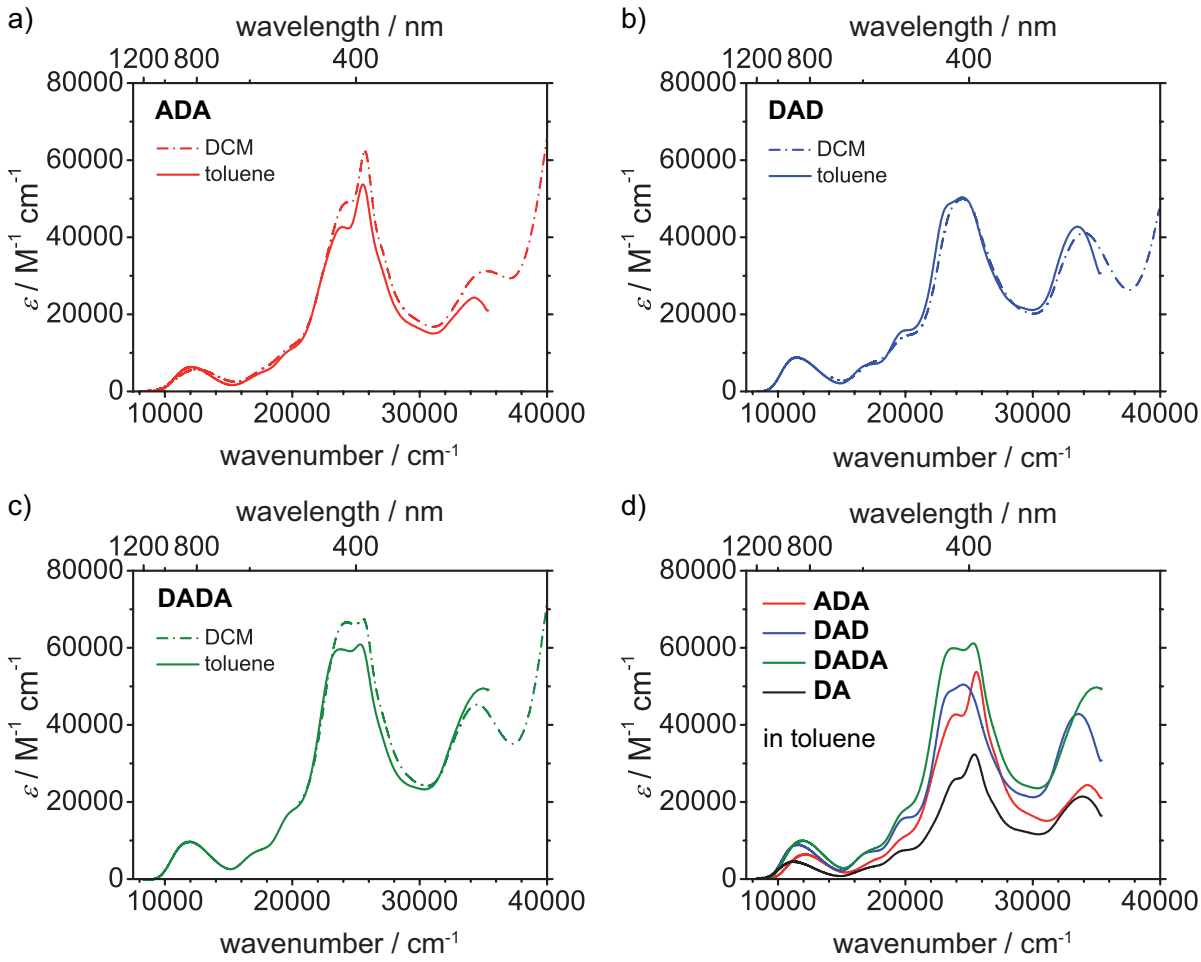

Figure 4.1: Absorption spectra of the oligomers investigated in this study. a) Absorption spectra of **ADA**, (b) **DAD**, and (c) **DADA** in DCM and toluene at room temperature. d) Absorption spectra of **ADA**, **DAD**, **DADA**, and **DA** in toluene. Adapted with permission from Ref. [5]. Copyright (2014) American Chemical Society.

4.3 Transient Absorption Spectroscopy and Global Lifetime Analysis

Excitation at 800 nm pump wavelength leads to direct population of the IVCT state in TAA–PCTM systems ("optical excitation"). Subsequent solvent reorganization leads to an increase of the excited-state absorption (ESA) of the IVCT state. Depending on the solvent's reorganization lifetimes and the CR lifetimes in the **DA**-system under consideration, the combination of solvent relaxation and CR leads to the dynamics described below and discussed in the next section. The thermal CR in TAA–PCTM systems can be observed by measuring the absorption of the transiently formed donor radical cation $TAA^{+\bullet}$ and the acceptor anion $PCTM^{-}$ in the IVCT state. The absorption of $TAA^{+\bullet}$ is reported to be between 14300 cm^{-1} and 12500 cm^{-1} (700 and 800 nm) [144], the absorption of perchlorinated triarylcarbanions around 19050 cm^{-1} (525 nm) [145]. The previously studied monomer **DA** with methoxy-substitution at the donor moiety and various related TAA–PCTM systems with different spacers, as well as polymer **P**

Table 4.1: Lifetimes in DCM and toluene from a sequential global fit. The relative error of the lifetimes is below 3% if not stated otherwise. Reprinted with permission from Ref. [5]. Copyright (2014) American Chemical Society.

		τ_1 / ps	τ_2 / ps	τ_3 / ps	τ_4 / ps	τ_5 / ps
DCM	**DA**	0.45[a]	0.45[b]	1.4	-	-
	ADA	0.29	0.91[c]	0.93[d]	-	-
	DAD	0.49[e]	0.50[f]	1.2	-	-
	DADA	0.54[g]	0.56[h]	1.5	-	-
	P	-	0.63[i]	1.5	69	∞
toluene	**DA**	0.19	2.8	11	-	-
	ADA	0.18	4.7	48	-	-
	DAD	0.16	4.0	20	-	-
	DADA	0.18	3.5	21	-	-
	P	0.25	8.4	27	110	∞

relative error: [a] 13%; [b] 13%; [c] 18%; [d] 17%; [e] 25%; [f] 25%; [g] 14%; [h] 15%; [i] 5%

show transient absorptions of the $TAA^{+\bullet}$ and $PCTM^-$ species formed upon optical excitation into the IVCT state in the abovementioned spectral regions [1,56,68,70,128,139]. Figure 4.2 shows selected difference spectra for various delay times τ after excitation in a spectral probe range from 13800 cm^{-1} (725 nm) to 24000 cm^{-1} (417 nm) for the molecules investigated in this study. The temporal evolution of the transient signals can be seen in Fig. 4.3 for a set of transients in the region of ground-state bleaching (blue), absorption of $PCTM^-$ (green) and $TAA^{+\bullet}$ (red). The EADS (Fig. 4.4) represent the amplitudes of the global-fitting-routine in a sequential model (Section 2.3). The lifetimes associated with the EADS are given in Table 4.1. In the cases where subsequent lifetimes are almost equal, the outcome of the fit was worse for one temporal component less, even if the relative error of these lifetimes gets larger than for the other lifetimes. Additionally, for the sake of consistency the same model was used for all investigated oligomers.

For the monomer **DA** dissolved in DCM one observes two distinct bands around 20000 cm^{-1} (500 nm) and below 15000 cm^{-1} (667 nm) after excitation (Fig. 4.2a). These absorption bands of the IVCT state were assigned to excited-state transitions of the $PCTM^-$ and the $TAA^{+\bullet}$ moiety, respectively. The assignment of the bands to IVCT-state transitions is supported by the spectroelectrochemistry data [5, 112] where the absorption bands of an oxidized donor ($TAA^{+\bullet}$) and reduced acceptor ($PCTM^-$) fit the observed transient absorption bands (see above). The bands in the spectroelectrochemical data [5,112] are slightly shifted toward lower wavenumbers (18000 cm^{-1} [555 nm] and 14200 cm^{-1} [704 nm]) compared to the time-resolved data. This red-shift was also observed for polymer **P** and methoxy-substituted **DA** [1]. The shift might be explained by the influence of the solvent (DCM/tetrabutylammonium hexafluorophosphate) used for the spectroelectrochemistry measurements. The maximum of the $TAA^{+\bullet}$ band cannot unambiguously be determined as for the red-edge part of the recorded spectrum, the bleaching of the PCTM band overlaps with the $TAA^{+\bullet}$ absorption. The ground-state bleaching of **DA** is observed above 23500 cm^{-1} (426 nm). For longer delay times ($\geq$ 1 ps) the $PCTM^-$ absorption band becomes more structured and develops into two slightly separated

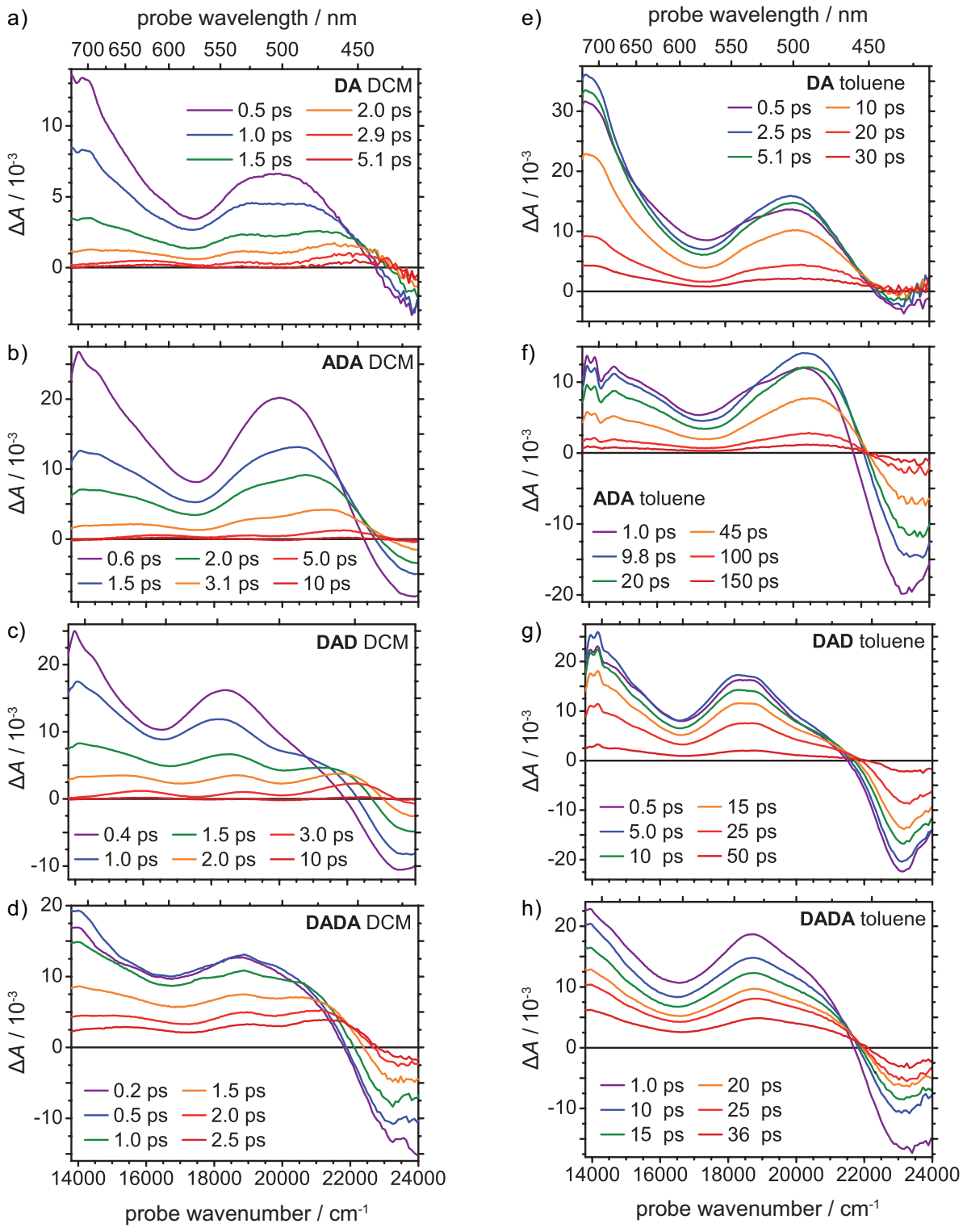

Figure 4.2: Transient difference spectra for various pump–probe delay times. a–d) Experimental data of **DA**, **ADA**, **DAD**, and **DADA** in DCM is shown in different colored lines for delay times $\tau > 0$. e–h) Experimental data of **DA**, **ADA**, **DAD**, and **DADA** in toluene is shown in different colored lines for delay times $\tau > 0$. Adapted with permission from Ref. [5]. Copyright (2014) American Chemical Society.

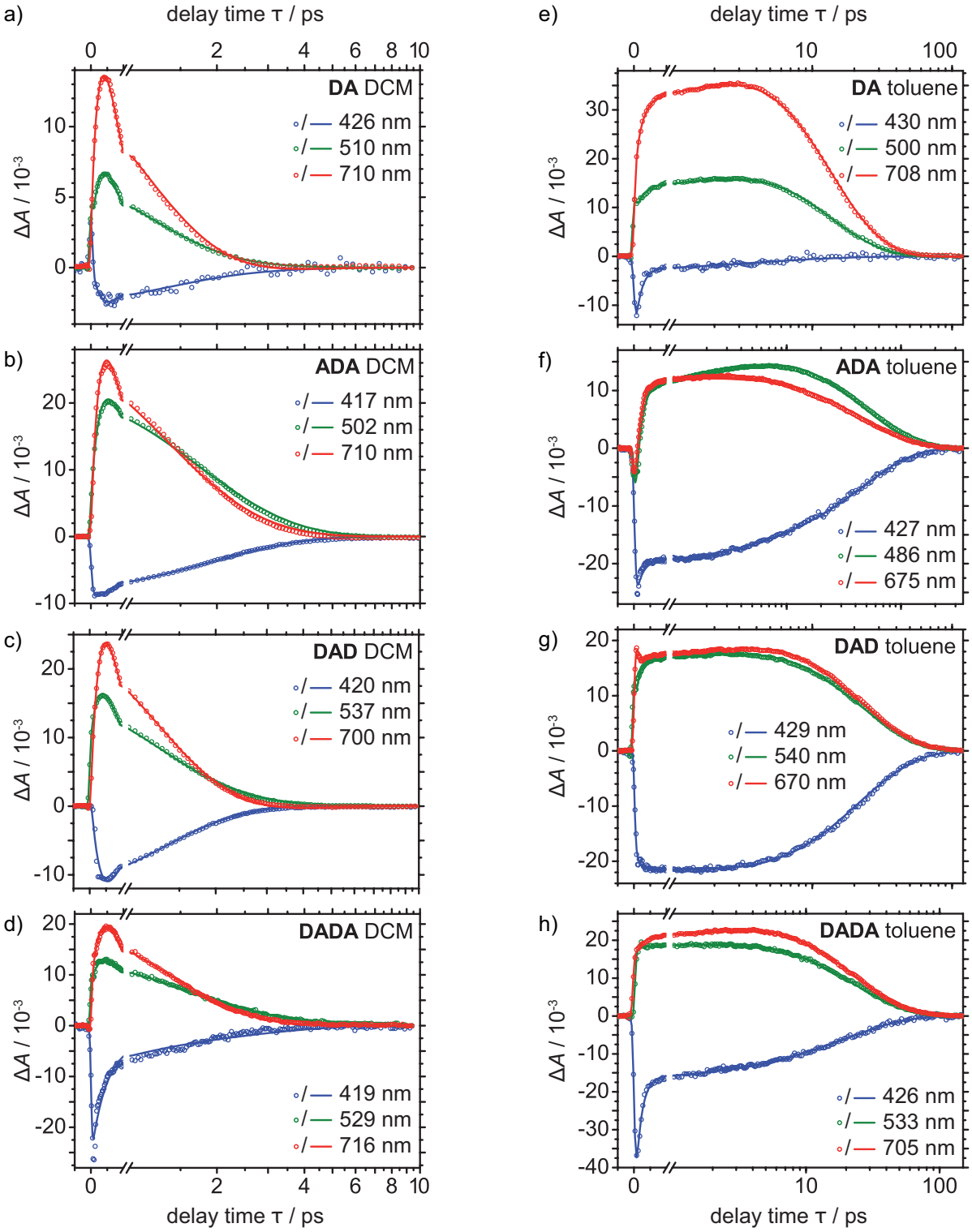

Figure 4.3: Transients for various probe wavelengths and corresponding global fits. a–d) Experimental data of **DA**, **ADA**, **DAD**, and **DADA** in DCM is given in circles, the result of the global fit is depicted with lines. e–h) Experimental data of **DA**, **ADA**, **DAD**, and **DADA** in toluene is given in circles, the result of the global fit is depicted with lines. Note that the delay time axis changes from linear to logarithmic scaling for $\tau = 1$ ps. Adapted with permission from Ref. [5]. Copyright (2014) American Chemical Society.

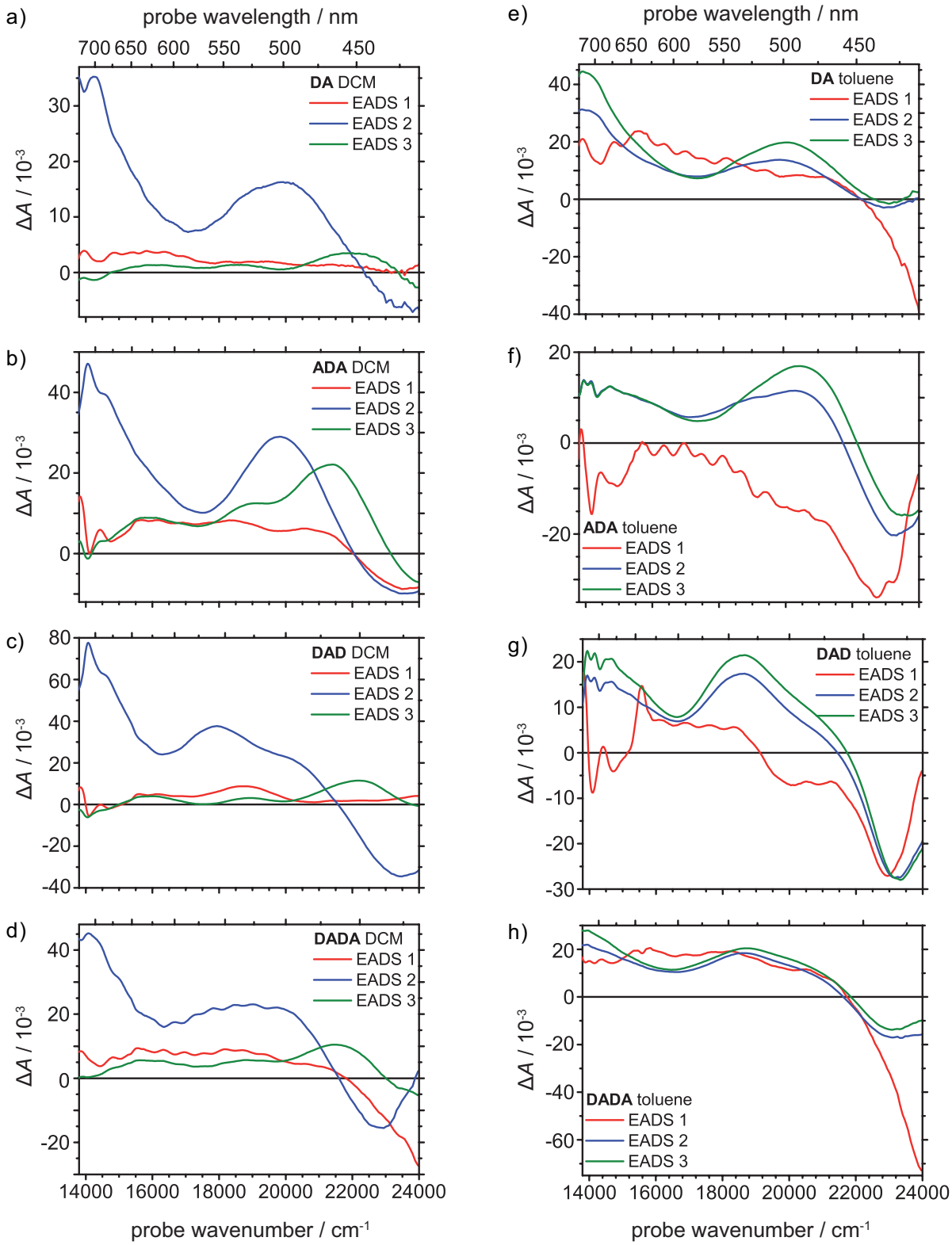

Figure 4.4: Evolution-associated difference spectra. a–d) The amplitudes for the global fitting results with three components in DCM are depicted with red (τ_1), blue (τ_2), and green (τ_3). e–h) The amplitudes for the global fitting results with three components in toluene are depicted with red (τ_1), blue (τ_2), and green (τ_3). The overlap of the coherent artifact with short-lifetime dynamics impedes the global fit and the chirp correction, resulting in wavelength oscillations and large amplitudes for EADS 1. Adapted with permission from Ref. [5]. Copyright (2014) American Chemical Society.

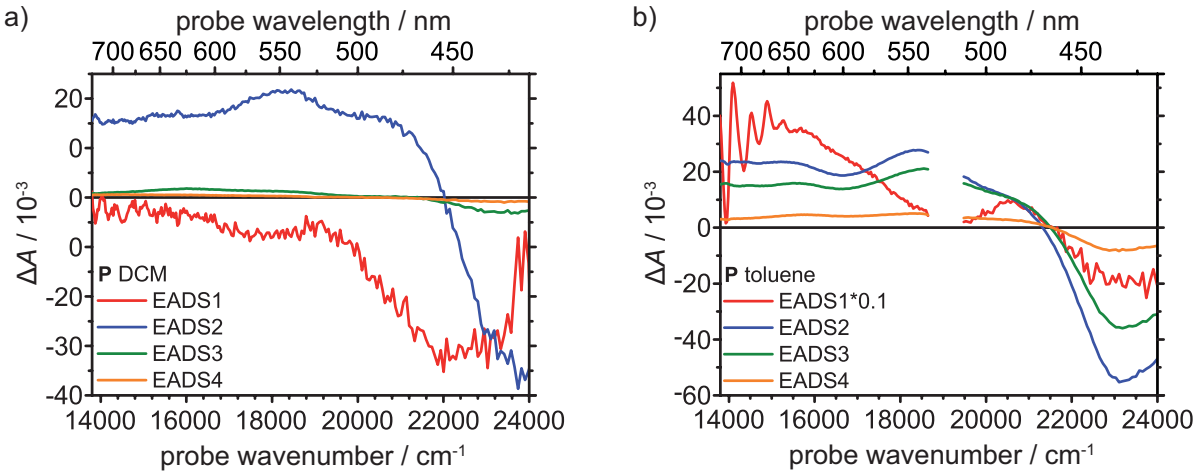

Figure 4.5: Evolution-associated difference spectra of **P**. a) The amplitudes for the global fitting results with four components of **P** in DCM are depicted with red (τ_1), blue (τ_2), green (τ_3), and orange (τ_4). For clarity the small amplitude of the offset lifetime τ_5 is omitted. b) The amplitudes for the global fitting results with five components of **P** in toluene are depicted with red (τ_1), blue (τ_2), green (τ_3), and orange (τ_4). Note that EADS 1 in toluene is multiplied by 0.1 for reasons of clarity. In general, the coarse step size in the polymer measurements complicate the fitting of the coherent artifact and the chirp correction, resulting in the wavelength oscillations and large amplitude of EADS 1. For clarity also the small amplitude of the offset lifetime τ_5 is omitted. Note that in the probe region from 18600 cm^{-1} to 19500 cm^{-1} data is not shown because of the presence of stray light. Adapted with permission from Ref. [5]. Copyright (2014) American Chemical Society.

maxima. The center between both new maxima is around the spectral position of the maximum of the $PCTM^-$ band for a delay time of 500 fs (Fig. 4.2a). Transients (Fig. 4.3a) are shaded by the coherent artifact [146–149] for delay times around time zero, but show a finite rise time for both IVCT-state absorption bands (green and red circles) and the ground-state bleaching (blue circles). All signals decay and recover, respectively, within less than 10 ps. The lifetime of the rise of the transient IVCT absorption bands was determined by the global fitting routine to be 450 fs (τ_1). This lifetime is in accordance with the rise time of the excited-state absorptions observed for the methoxy-substituted **DA** in DCM and methoxy-substituted **DA** without the bridging ethylene unit and corresponds to the previously studied solvent reorganization upon photoexcitation [68]. The decay of the transient absorption signals and the recovery of the ground-state bleaching were modeled with two exponentials resulting in τ_2 = 450 fs and τ_3 = 1.4 ps. The resulting amplitudes of the global fit (DCM) are given in the EADS (Fig. 4.4a). Apart from the small amplitude contribution of EADS 1 (red), EADS 2 (blue) and EADS 3 (green) match the difference absorption for short and longer delay times (Fig. 4.2a). The maximum of the $TAA^{+\bullet}$ band shifts for delay times > 2 ps to approximately 16000 cm^{-1} (625 nm). Even though the CR observed for the methoxy-substituted **DA** was determined to be monoexponential in Ref. [1], the two time constants for the decay of the IVCT-state population in **DA** found in this analysis are consistent with the earlier results as those were not fitted globally but for selected wavelengths only.

The difference spectra of **ADA** (Fig. 4.2b) in DCM strongly resemble the transient absorption of **DA**. The bands of $PCTM^-$ and $TAA^{+\bullet}$ as well as the ground-state bleaching are at the

same spectral position as in **DA**. The shift of the maxima observable for **ADA** is similar to the shift of the band of **DA** as a function of temporal evolution. The lifetime of the rise of the transient IVCT absorption bands (Fig. 4.3b) was fitted with $\tau_1 = 290$ fs and is therefore on the same order of magnitude as in the monomer. The biexponential decay of the IVCT-state absorption bands was fitted with 910 and 930 fs. The EADS of the DCM solution (Fig. 4.4b) are qualitatively equivalent to the EADS of **DA**.

For the **DAD** oligomer the maximum of the $PCTM^-$ absorption band is centered at 18500 cm^{-1} (541 nm) due to a more pronounced overlap with a slightly red-shifted ground-state bleaching compared to **ADA**. The $TAA^{+\bullet}$ absorption band remains maximal below 14500 cm^{-1} (690 nm). The blue-shift of the $TAA^{+\bullet}$ band with temporal evolution is comparable to that in **DA** and **ADA**, whereas the lower-energy maximum of the split $PCTM^-$ band shows only a small shift of about 500 cm^{-1} for longer delay times (Fig. 4.2c). The solvent reorganization dynamics leading to a rise in the IVCT excited-state absorptions was fitted with a lifetime of $\tau_1 = 490$ fs. However, the decay resembles more the **DA** dynamics than the **ADA** dynamics with lifetimes of 500 fs and 1.2 ps (Fig. 4.3c). The EADS slightly differ for the second and third fitting component consistent with the slightly differing transient difference spectra (Fig. 4.4c).

Compared to the other oligomers dissolved in DCM, **DADA** shows a more pronounced ground-state bleaching signal (Fig. 4.2d) due to the slightly red-shifted ground-state absorption with respect to the other oligomers, but is still above 23500 cm^{-1} (426 nm). The $PCTM^-$ band is initially centered at 19000 cm^{-1} (526 nm) and only a marginal blue-shift with time is observed after the second maximum gets visible on the blue edge of the $PCTM^-$ absorption band. Together with the fact that the $PCTM^-$ and the $TAA^{+\bullet}$ absorption bands are rather flat, these observations, which were already made for **P**, indicate that **DADA** starts to show first properties already observed for the polymeric compound. The DCM solution of the dimer **DADA** (Fig. 4.3d) possesses a solvent reorganization lifetime $\tau_1 = 540$ fs and a biexponential decay of the IVCT excited-state absorptions with $\tau_2 = 560$ fs and $\tau_3 = 1.46$ ps. Figure 4.4d displays the EADS for **DADA** in DCM, which have the same qualitative appearance as for the other oligomers.

In the following, the dynamics in toluene are discussed. In the monomer **DA**, two bands can be observed in the visible spectral regime around 20000 cm^{-1} (500 nm) and 14000 cm^{-1} (714 nm) in addition to a ground-state bleaching around 23500 cm^{-1} (426 nm, Fig. 4.2e). Apparently, the less polar solvent toluene does not significantly change the spectral properties of the transient absorption for the $PCTM^-$ and the $TAA^{+\bullet}$ band. Also the ground-state bleaching is only slightly shifted in accordance with the small shift in the steady-state absorption. Like in DCM, the two transient bands are assigned to the absorption of the IVCT state. The coherent artifact again partially disguises the dynamics directly after time zero (Fig. 4.3e). Anyhow, the dynamics of all investigated oligomers change significantly in toluene. The rise of the $PCTM^-$ and the $TAA^{+\bullet}$ signals is slower than in DCM and was fitted biexponentially in toluene. For **DA**, the faster component is given with a lifetime of 190 fs. The slower component has a lifetime of 2.8 ps. Such a biexponential solvent reorganization process has been reported earlier for toluene [150]. Compared to DCM, the charge recombination is a factor of about 10 slower in toluene and also slower than the typical solvent relaxation observed in toluene. Therefore, the absorptions of the $TAA^{+\bullet}$ and the $PCTM^-$ moiety decay monoexponentially (Fig. 4.3e). In addition, no spectral shift in the bands' maxima is observed (Fig. 4.2e). The ground-state

bleaching is centered around 23500 cm^{-1} (426 nm) in accordance with the low-energy shoulder of the linear absorption spectrum (Fig. 4.1). The CR was fitted with a lifetime of 11 ps and is in accordance with earlier results for methoxy-substituted **DA** [1, 128]. This behavior can also be seen from Fig. 4.4e (toluene), where EADS 2 (population of the IVCT state) and EADS 3 (CR) mainly differ in their relative amplitudes but show the same qualitative spectral shape (toluene).

In the case of **ADA**, the solvent relaxation lifetimes were determined to be 180 fs and 4.7 ps (Fig. 4.3f). The $PCTM^-$ absorption around 20500 cm^{-1} (488 nm) does not show a spectral shift with time, neither does the $TAA^{+\bullet}$ band above 17000 cm^{-1} (588 nm, Fig. 4.2f). The $PCTM^-$ and $TAA^{+\bullet}$ bands decay monoexponentially. The ground-state bleaching and the excited-state absorption signal contributions have not completely recovered and decayed, respectively, until a delay time greater than 100 ps. This qualitative finding is quantified in the slowest CR dynamics within all four molecules investigated with $\tau_3 = 48$ ps. The second and third EADS (Fig. 4.4f) in toluene are relatively similar and also coincide in the red part of the spectrum.

For **DAD** the solvent relaxation lifetimes were determined to be 160 fs and 4.0 ps (Fig. 4.3g). The CR is indeed a factor of 2.4 faster ($\tau_3 = 20$ ps) than in **ADA**. The $PCTM^-$ band appears significantly red-shifted around 18500 cm^{-1} (541 nm). Like in **ADA**, both the $PCTM^-$ absorption and the ground-state bleaching signal slightly shift to higher wavenumbers (Fig. 4.2g). The EADS (Fig. 4.4g) in toluene are very similar for the second solvent relaxation component (EADS 2) and the charge recombination (EADS 3).

Finally, the dimer **DADA** shows solvent relaxation lifetimes of 180 fs and 3.5 ps (Fig. 4.3h). The $PCTM^-$ absorption around 19000 cm^{-1} (526 nm) and the $TAA^{+\bullet}$ absorption below 14500 cm^{-1} (690 nm) exhibit no spectral shift with time in toluene (Fig. 4.2h). Like **DA**, **DADA** does not show a shift of the ground-state bleaching. The lifetime of the CR in **DADA** is equivalent to the CR in **DAD** ($\tau_3 = 21$ ps) and the decay of the excited-state absorption is also monoexponential. The EADS associated with the slower solvent relaxation process and the CR in toluene (blue and green in Fig. 4.4h) are very similar in shape and amplitude, indicating the absence of states between the IVCT and the ground state.

For reasons of better comparison a global lifetime analysis was performed for the polymer data [1], resulting in similar results as in Ref. [97] (Table 4.1). In the previous study, the polymer was excited at 525 nm, for which reason a comparison of the oligomer data and the polymer data should only be done for delay times > 1 ps, where possible excess energy in the polymer already has dissipated to the bath. For the dynamics in DCM four time components were fitted. Due to a coarse temporal step size and a higher energetic excitation in the measurements of **P**, the first lifetime τ_1 could not unambiguously be fitted and did not improve the fitting result either, which is the reason why it was not considered in the fit. Therefore, only one short time constant τ_2, assumed to represent the CR lifetime, was determined. The slow solvent reorganization component was again fitted with a lifetime $\tau_3 = 1.5$ ps. Two additional longer lifetimes were necessary to adequately fit the data. The lifetime $\tau_4 = 69$ ps represents the CR of previously completely separated charges (τ_3 in Ref. [1]). The lifetime τ_5 set to infinity represents the permanent offset observed in the previous experiment for a fit of single probe wavelengths. In toluene, the dynamics for **P** were fitted with five temporal components. Due to the rather coarse step size, the short lifetimes are only properly fitted in toluene, whereas in DCM the short dynamics are disguised by the lack of temporal resolution. τ_1 and τ_2 represent the solvent reorganization, τ_3 the CR, τ_4 the charge recombination from a prior completely

charge-separated structure and τ_5 the remaining offset. The EADS of the global fitting results are given in Fig. 4.5a,b (DCM and toluene). This model requires an almost negligible exciton binding energy between positive and negative charges as otherwise charges would not dissociate along the polymer chain. A small exciton binding energy in **P** was indeed found by comparison of electrochemically and optically determined band gaps [1]. However, the extent of charge separation could not be manifested in these experiments.

4.4 Discussion of the Electron-Transfer Dynamics

In case of **ADA** and **DADA**, the ground and the IVCT state might adopt either singlet or triplet spin multiplicity because of the two unpaired electrons at the two PCTM acceptors. These states of different spin multipliticity are assumed to be almost degenerate in energy and not suppossed to show different absorption properties either in the ground and the excited state. Therefore, the following discussion will not consider any effect of the different spin multiplicities on the interpretation of the time-resolved data.

After optically-induced CT from the TAA donor to the PCTM acceptor, the surrounding solvent molecules have to rearrange to the new charge distribution in the IVCT state. In toluene solutions of all four molecules under investigation two time constants for the rise of the transient absorption bands of the IVCT state were determined with the global fitting routine. The signals' evolutions can be described by two processes assigned to a fast librational motion and a slower diffusive contribution of the solvent molecules to adopt to the IVCT charge distribution [151]. From time-resolved fluorescence measurements of coumarin C153 it is known that toluene shows a short component for the solvent reorganization with a lifetime of 370 fs and a longer component of 2.7 ps [150]. As the biexponential risings of the transient absorption bands of all four oligomers show similar time constants (τ_1 = 160–190 fs and τ_2 = 2.8–4.7 ps), these time constants can clearly be assigned to the solvent relaxation after population of the IVCT state because the optically-induced ET takes place at the equilibrium ground-state geometry. The detection of the fast electron transfer—directly populating the IVCT state—is in our case not only limited by the temporal resolution of the setup, but also by the solvent reorganization, which leads to a delayed evolution of the signals' maxima when the solvent has relaxed along an averaged solvent reaction coordinate into the IVCT-state geometry.

The CR, which was determined to occur in the Marcus inverted region for methoxy-substituted **DA** [1,68], is much slower than the initial electron transfer. The present oligomers were constituted from TAA and PCTM moieties which are known to have small inner reorganization energies, anticipating high energy barriers for the electron back-transfer (slower CR) from the optically-induced IVCT state.

Two time constants were reported for the dielectric relaxation process of DCM [63]. The faster one has a lifetime of about 400 fs in accordance with the result of τ_1 = 290–540 fs for the rise of the transient absorptions of $TAA^{+\bullet}$ and $PCTM^{-}$ in the oligomers in DCM. The slower component of 1.5 ps is equivalent or even slower than the third lifetime (τ_3) determined with the global fit. Therefore, the CR is described by the second lifetime from the global fit ranging from 450–910 fs (τ_2) in DCM. With the CR being faster than the slow component of the solvent relaxation, the decays of the excited-state absorptions show biexponential behavior. Using solvents of similar spectroscopic properties like DCM but different solvent relaxation

times could substantiate this assumption. Unfortunately, this approach is restricted for the inspected oligomers due to their limited solubility in solvents other than DCM and toluene. Additionally, one has to take into account that the rise of the transient absorption bands is shaded for short delay times by the coherent artifact. As the CR is ultrafast in DCM, one could also assign the third lifetime to the cooling of a hot ground state within less than 1.5 ps. This assumption seems reasonable if the shapes of EADS 3 (Figs. 4.4a–d) are considered, which show a reduced ground-state bleaching and a broad red-shifted absorption. Within transient absorption spectroscopy, either solvent relaxation or absorption of a hot ground state cannot unambiguously be assigned to EADS 3.

4.5 Electron-Transfer-Rate and Free-Energy Calculations

As for DCM and toluene strongly differing CR dynamics could be observed, this fact was scrutinized in the framework of Marcus theory. For gaining a more detailed insight estimates for the free energies ΔG of the electron transfer processes and for the reorganization energies λ are needed (Section 2.5) . Therefore, the free energies $\Delta G^0_{\mathrm{IVCT}}$ of the IVCT states were calculated from the redox potentials $E^{\mathrm{ox}}_{1/2}$ and $E^{\mathrm{red}}_{1/2}$ (Table 4.2) with the approach of Weller according to Eq. (2.25). The radii $\mathrm{r_D}$ and $\mathrm{r_A}$ of the TAA and PCTM moieties were estimated by radii of spheres with the same surface as the Connolly molecular surface calculated for the single TAA and PCTM subunits within ChemBio3D Ultra [152]. The distance d_{DA} between the donor and acceptor centers—assumed as point charges—were calculated with CAM-B3LYP/6-31G* level of theory using Gaussian09 [153].

The inner and outer reorganization energies λ_{i} and λ_{o} for CR can in principle be extracted from absorption or emission spectra by fitting them with the model of Jortner [71, 154, 155]. However, there are some limitations to this approach which complicate a band-shape analysis. Thus, calculated values for the inner reorganization energies λ_{i} were taken from literature. Density functional theory calculations revealed an inner reorganization energy of λ_{i} = 0.274 eV for a methoxy-substituted TAA and λ_{i} = 0.129 eV for a methyl-substituted TAA [156] and were assumed for terminal and central TAA units, respectively. For the PCTM moiety, λ_{i} was calculated to be 0.22 eV [157]. Combining these values results in inner reorganization energies of [(0.129 + 0.22)/2] eV = 0.175 eV (for processes between the central $\mathrm{TAA^{+\bullet}}$ unit and $\mathrm{PCTM^-}$) and [(0.274 + 0.22)/2] eV = 0.247 eV (between a terminal $\mathrm{TAA^{+\bullet}}$ unit and $\mathrm{PCTM^-}$), respectively, for the CR in the oligomers of this study (Table 4.2). The outer reorganization energies λ_{o} were calculated from Eq. (2.26). The results for the free energy and the reorganization energy calculations are given in Table 4.2.

Table 4.2: Radii of donor and acceptor moieties, donor–acceptor distances, redox potentials, reorganization energies, free energies, and barriers for the **DA** oligomers and **P**. The radii r_A and r_D represent the radii of spheres with the same surface than the Connolly molecular surface (see text). Outer reorganization energies (λ_o) are calculated from Eq. (2.26), inner reorganization energies are taken from literature (TAA) and calculated by DFT (PCTM). Reprinted with permission from Ref. [5]. Copyright (2014) American Chemical Society.

	D^+A^-	AD^+A^-	D^+A^-D	D^+ADA^-		D^+A^-DA	DA^-D^+A	DAD^+A^-	$...D^+A^-...$	$...D^+ADA^-...$	
				bent	stretched					bent	stretched
r_A / Å	5.62	5.62	5.62	5.62	5.62	5.62	5.62	5.62	5.62	5.62	5.62
r_D / Å	4.81	4.81	4.81	4.81	4.81	4.81	4.81	4.81	4.81	4.81	4.81
d_{DA} / Å	12.42	12.44	12.43	26.10	30.91	12.44	12.44	12.44	12.44	26.10	30.91
$E^{ox}_{1/2}$ / V	0.24	0.34	0.20	0.18	0.18	0.18	0.30	0.30	0.34	0.34	0.34
$E^{red}_{1/2}$ / V	−0.69	−0.58	−0.68	−0.68	−0.68	−0.74	−0.74	−0.68	−0.69	−0.69	−0.69
λ_i / eV	0.247	0.175	0.247	0.247	0.247	0.247	0.175	0.175	0.175	0.175	0.175
λ_o(toluene) / eV	0.05	0.05	0.05	0.07	0.07	0.05	0.05	0.05	0.05	0.07	0.07
λ(toluene) / eV	0.30	0.23	0.30	0.32	0.32	0.30	0.23	0.23	0.23	0.25	0.25
ΔG^0_{IVCT}(toluene) / eV	−1.30	−1.29	−1.25	−1.47	−1.51	−1.29	−1.41	−1.34	−1.40	−1.65	−1.68
ΔG^*(toluene) / eV	0.85	1.26	0.76	1.05	1.12	0.83	1.57	1.39	1.54	2.02	2.11
λ_o(DCM) / eV	0.62	0.62	0.62	0.85	0.88	0.62	0.62	0.62	0.62	0.85	0.88
λ(DCM) / eV	0.87	0.80	0.87	1.10	1.13	0.87	0.80	0.80	0.80	1.03	1.06
ΔG^0_{IVCT}(DCM) / eV	−0.80	−0.80	−0.75	−0.79	−0.80	−0.79	−0.91	−0.85	−0.90	−0.97	−0.98
ΔG^*(DCM) / eV	0.00	0.00	0.00	0.02	0.02	0.00	0.00	0.00	0.00	0.00	0.00

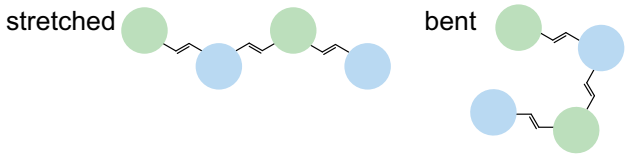

Chart 4.2: Schematic representation of the stretched and bent configuration of **DADA**. Reprinted with permission from Ref. [5]. Copyright (2014) American Chemical Society.

For the dimer **DADA** different possible IVCT configurations (e.g., $\mathbf{D^+ADA^-}$, $\mathbf{D^+A^-DA}$ etc.) were considered but also two different conformers (stretched vs. bent, Chart 4.2) for $\mathbf{D^+ADA^-}$ which differ in the terminal TAA–PCTM distance. The reorganization energy λ was previously determined for the methoxy-substituted **DA** by a Jortner fitting approach to be 0.59 eV in DCM [69] which is the same order of magnitude as the estimated reorganization energy of 0.87 eV of **DA** in DCM, confirming the use of Eq. (2.26) for the calculations. Within Marcus theory, the free energy barrier ΔG^* (Table 4.2) for the electron back-transfer was calculated via Eq. (2.23). All calculations were also performed for the polymer **P**, i.e., for the **DADA** configurations with the properties of central TAA or PCTM units only.

Even though these calculated parameters are rather rough estimates and do not allow a quantitative analysis, the corresponding electron-transfer region in terms of Marcus theory can be predicted by comparing the free energies and the reorganization energies. If for **DADA** only configurations are taken into consideration where the electron and the hole are centered on adjacent TAA and PCTM subunits, i.e., assuming that the CR predominantly occurs from these configurations (see below), the free energies approximately equal the reorganization energies ($-\Delta G^0_{\mathrm{IVCT}} \approx \lambda$ within 0.1 eV) for all oligomers in DCM. Hence, in DCM the electron back-transfer is estimated to take place in the optimal region where the activation barrier ΔG^* approaches zero (Fig. 2.6c). The optimal-region effect is also confirmed by the calculated barriers ΔG^* for the CR in DCM which are zero for all oligomers and possible configurations.

From these findings, one can explain why the CR lifetimes τ_2 in DCM show almost no difference for all four molecules. Although the oligomers possess significant differences in their electron-donor and -acceptor strengths, a CR barrier $\Delta G^* = 0$ leads to the maximal CR rate ($k_{\mathrm{CR}} = 1/\tau_2 = 1.1\text{–}2.2 \times 10^{12}\,\mathrm{s^{-1}}$) in all oligomers.

The CR lifetimes in DCM are about one to two orders of magnitude shorter than in toluene solutions, which indicates that in the latter solvent the activation barrier is significantly larger. The calculated free energies for the CR barrier ΔG^* are shown in Table 4.2. By comparing the free energies and the reorganization energies one sees that $-\Delta G^0_{\mathrm{IVCT}} > \lambda$ in toluene, i.e., the electron back-transfer is clearly in the Marcus inverted region (Fig. 2.6d), i.e., the CR rate is slowed down although the exergonicity of the CR is increased compared to the normal region.

Despite that the calculation of ΔG^* is valuable in an estimation of the Marcus region, the size of the activation barrier does not fully explain the different CR dynamics observed experimentally. In the case of **ADA**, the CR lifetime increases by a factor of ~4 compared to **DA**. This is obvious, as the activation barrier increases significantly for **ADA** ($\Delta G^* = 1.26$ eV) compared to **DA** ($\Delta G^* = 0.85$ eV). Within 0.1 eV, **DAD** ($\Delta G^* = 0.76$ eV) has the same barrier for the CR as **DA**. However, the CR is a factor of 2 slower for **DAD** (Table 4.1). A possible explanation for the discrepancy of τ_3 in **DAD** could be the effect that the estimations of λ_o and ΔG are less reliable in toluene than in dipolar solvents. This is because dipolar solvents are better

described by their permittivity ϵ_s than quadrupolar solvents like toluene, and thus reorganization energies are estimated more reliably by Eq. (2.26) in DCM than in toluene. If dielectric constants ϵ [158] are compared, toluene ($\epsilon = 2.379$) appears to be significantly less polar than DCM ($\epsilon = 9.08$), but if empirical $E_T(30)$ values for polarity [159] are considered, toluene is described about as polar ($E_T(30) = 33.9\,\text{kcal/mol}$) as ethyl ether ($E_T(30) = 34.5\,\text{kcal/mol}$) and therefore shows about a similar value for polarity as DCM ($E_T(30) = 40.7\,\text{kcal/mol}$).

For **DADA**, the CR lifetime in toluene is the same as in **DAD**, but the activation barriers for the different configurations vary from the same barrier size as **DA** to barrier sizes even larger than in **ADA**. The fact that in **DADA** only one CR lifetime is observed and not several different ones—each according to a barrier corresponding to a specific configuration—shows that there must be fast prior equilibrations between the IVCT configurations (Scheme 4.1). These prior equilibria consist of either charge separation (k_{sep1}–k_{sep3}) to the completely charge-separated $\mathbf{D^+ADA^-}$ configuration or charge shifts (k_{EN1}–k_{EN3}). The charge shifts are equal to energy transfers, i.e., exciton diffusion, because the IVCT excitation is transferred to a different donor–acceptor pair via electron and hole transport. These prior equilibria provoke that CR occurs only from the configuration with the smallest CR barrier, i.e., with the shortest CR lifetime. Configuration $\mathbf{D^+A^-DA}$ has the smallest CR barrier and hence the fast prior equilibrations lead to CR only from this **DADA** configuration (k_1, Scheme 4.1) and therefore to suppression of CR from the other configurations (k_2–k_4) as equilibration to the fastest CR channel is faster than the actual CR. Justification for the assumption about the relative speed of these processes can be obtained from calculating barriers for the charge shift. This barrier was calculated in **ADA** ($\mathbf{A^-D^+A}$ to $\mathbf{AD^+A^-}$) and **DAD** ($\mathbf{D^+A^-D}$ to $\mathbf{DA^-D^+}$) for electron transfer between degenerate "donor" and "acceptor" ($\Delta(\Delta G^0_{IVCT}) = \Delta G^0 = 0$, $\Delta G^* = \lambda/4$, see Eq. (2.22) to be 0.06 eV and 0.08 eV, respectively. These values are much smaller than the barriers for CR in all oligomers ($|\Delta G^*| \geq 0.76\,\text{eV}$). Thus indeed charge diffusion is faster than CR. The equilibration between the different IVCT configurations cannot be detected experimentally as the transient absorptions of the equilibrating configurations are equal. It was observed already for **P** that the absorption of the completely charge-separated structure (...$\mathbf{D^+}$...$\mathbf{A^-}$...) does not differ from the configuration with neighboring electrons and holes (...$\mathbf{D^+A^-}$...).

To validate the calculated barriers, the corresponding rates k_{CR} for a thermal electron back transfer and a given electronic coupling integral V were calculated for an absolute temperature $T = 295.15\,\text{K}$. Especially in the inverted region (i.e., in toluene), the Marcus equation [Eq. (2.27)] yields rate constants which underestimate the experimentally observed rate constants by orders of magnitude. Therefore, the semiclassical approach of Eq. (2.31) was used to obtain more reliable results. The longitudinal solvent relaxation times ($\tau_L(\text{DCM}) = 400\,\text{fs}$, $\tau_L(\text{toluene}) = 370\,\text{fs}$) were taken from literature [63, 150] and taken into account within the adiabtic parameter H_A [Eq. (2.30)].

Even though the Jortner model assumes diabatic free energy surfaces, it yields correct results for calculations of adiabatic systems [69–71]. For the calculations, $j = 0$–20 and $V = 2310\,\text{cm}^{-1}$ was used ($V = 2310\,\text{cm}^{-1}$ in acetonitrile [70]). For the averaged vibrational mode a typical value $\tilde{\nu}_v = 1550\,\text{cm}^{-1} \mathrel{\hat{=}} 3.08 \times 10^{-20}\,\text{J} = 0.19\,\text{eV}$ was assumed ($\tilde{\nu}_v = 1550\,\text{cm}^{-1}$ for methoxy-**DA** in DCM [69, 70]). The results of the rate-constant calculations are given in Table 4.3 as the corresponding CR lifetimes $\tau_{CR} = 1/k_{CR}$.

For the optimal region in DCM the calculated lifetimes τ_{CR} (Table 4.3) match the experimentally determined CR lifetimes τ_2 (Table 4.1) quite well, only deviating by a factor of two.

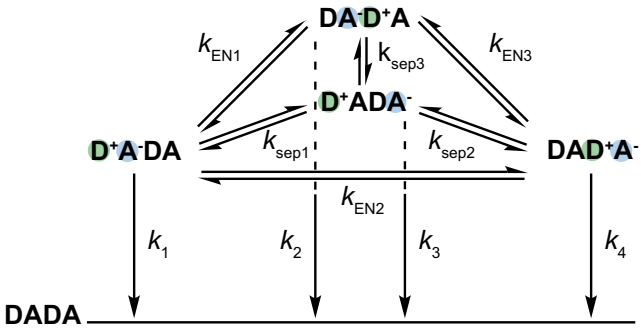

Scheme 4.1: Schematic representation of the equilibration and charge splitting within **DADA**. Energy transfers via charge shifts are depicted with their rates k_{EN1}–k_{EN3}, charge separations with the rates k_{sep1}–k_{sep3}. Note that the equilibrium arrows only represent an averaged rate constant as the rates and the energy of the equilibrated species might differ depending on which **DADA** IVCT configuration was initially excited. The height of the excited species does not represent their relative energies. Reprinted with permission from Ref. [5]. Copyright (2014) American Chemical Society.

Table 4.3: Calculated CR lifetimes τ_{CR} in DCM and toluene from Eq. (2.31). For **DADA** and **P** only the configuration with the smallest barrier is considered. Reprinted with permission from Ref. [5]. Copyright (2014) American Chemical Society.

		DA	**ADA**	**DAD**	**DADA**	**P**
DCM	τ_{CR} / ps	0.26	0.26	0.27	0.26	0.25
toluene	τ_{CR} / ps	6.6	8.7	3.0	6.1	5.8

In toluene, the calculated lifetimes fit well for **DA** but differ for **ADA**, **DAD**, **DADA**, and **P** (τ_3, Table 4.1). For **ADA**, **DAD**, **DADA**, and **P** the lifetimes are significantly underestimated. This deviation is likely due to the quadrupolar nature of toluene, preventing accurate estimates of λ_o [Eq. (2.26)] and thus of k_{CR} [Eq. (2.31)] as explained above.

The dimer **DADA** is the smallest **DA**-based structure which allows complete charge separation along the molecular backbone (**D**$^+$**ADA**$^-$). With the equilibrations (Scheme 4.1) in the structure being significantly faster than the CR, one can explain why charge splitting in **P** leads to the observed additional time constant (Table 4.1), because the single equilibrations sum up to a rate-determining slow process. In the dimer **DADA** the charges cannot separate further apart, i.e., no additional temporal component is observed. In polymer **P**, the separated charges can even migrate further apart, therefore a larger number of fast charge shifts sum up to the overall additional lifetime τ_4. For **P** the calculated CR barriers are even larger than in **ADA**, but **P** exhibits a CR lifetime in between the CR lifetimes of **DAD** and **ADA**, which is again a hint that toluene is not well represented by its dielectric constant in Eq. (2.26).

4.6 Conclusion and Outlook

The transient absorption spectroscopy of three different oligomers and a reference monomer based on TAA electron donors and PCTM electron acceptors was shown in this chapter. After optically-induced electron transfer these systems show charge recombination (CR) dynamics which were unraveled by ultrafast transient absorption spectroscopy. In combination with

electron-transfer-theory calculations of the CR barriers ΔG^*, and the CR lifetimes for the compounds, the experimentally observed CR lifetimes determined from a global fit of the data could be explained.

The CR dynamics in DCM are superimposed by a slow component of the solvent reorganization, yielding a biexponential decay of the IVCT excited-state absorptions. In DCM, the CR is fast ($\sim$ 500 fs) and does not show significant differences among the investigated oligomers. From this experimental finding and the calculated CR barriers being zero for all oligomers, we derive that the CR takes place in the optimal region, i.e., without a barrier the CR reaches the maximal possible rate.

In toluene, however, the solvent relaxation lifetimes show up as a biexponential rise of the IVCT excited-state absorptions. The actual CR is much slower (11 to 48 ps) than the solvent reorganization. Hence the CR is significantly slower than in DCM, taking place in the Marcus inverted region with a much larger CR barrier. The inverted-region effect is also confirmed by the calculated CR barriers being larger than the calculated reorganization energies.

For the dimer **DADA**, only one CR lifetime was observed, and not several ones as expected from the different possible excited IVCT configurations. Therefore, fast prior equilibrations among the IVCT configurations were postulated. One the one hand, these equilibrations explain why only one CR lifetime is observed for **DADA** by fast population of the lowest-barrier configuration outcompeting the slower CR channels. On the other hand, prior equilibrations make clear that already from a length of two **DA** pairs on, charge shifts and splittings exhibit only small barriers, i.e., electron–hole pairs on linear TAA–PCTM compounds already separate in the smallest possible compound allowing a completely charge-separated structure. These fast, small-barrier processes then lead to the migration of charges in larger structures, in sum yielding the slower CR component observed in **P**.

The access to defined longer **DA** oligomers is so far synthetically challenging but would give some additional information about how far mobile charges separate on a given molecular backbone. Power-dependent exciton–exciton annihilation experiments shown previously in molecular aggregates and polymer films [160, 161] would also give some more detailed insight. CR and charge splitting are important processes to study for the understanding of natural light harvesting-systems and low-band-gap materials for optoelectronics. The study of variable-length **DA** oligomers with ultrafast spectroscopy, as demonstrated in the present work, allows determining whether photoinduced charge transfer occurs only to a neighboring subunit or whether the charges split further apart. The latter process is desirable for charge carrier mobility in photovoltaic devices, and thus microscopic evaluations of charge transport are valuable tools.

5 Ultrafast Photolysis of a CO-Releasing Molecule (CORM)

The work presented in this chapter was conducted in cooperation with the group of Prof. Dr. Ulrich Schatzschneider. The content of Sections 5.3 to 5.5 has previously been published in Refs. [2,3]. The TDDFT calculations described in Section 5.3 were performed by Prof. Dr. Ulrich Schatzschneider, the DFT calculations by Dr. Philipp Rudolf. Details on the calculation parameters can be found in Refs. [2,9].

The ultrafast photochemistry of carbon-monoxide-releasing molecules (CORMs) is a subject worth studying for several reasons. So far, knowledge about the primary steps in photochemistry and therefore about the carbon-monoxide release mechanism of CORMs was very limited. Thus, the study presented in this chapter could significantly improve the knowledge about the dynamics and also about the initial quantities of the CO liberation in tpm-CORM. But also investigating such a fundamental chemical reaction such as bond breaking is of great importance within the scope of this thesis. In the previous chapter, the studied molecules remained intact upon photoexcitation and only charges were transferred, i.e., the formal oxidation state of several subunits changed. In contrast, in the following sections, the investigated compound shows dissociation of a certain bond upon excitation. Section 5.1 focuses on the therapeutic potential of CO and especially on its pharmaceutical form as CORMs. After that, Section 5.2 shortly introduces the photochemistry of transition metal complexes. The results of theoretical calculations and linear absorption spectra shown in Section 5.3 are employed to interpret the ultrafast time-resolved spectroscopic findings in Section 5.4. Finally, the results are summarized in the last section with a short outlook on future experiments.

5.1 Therapeutic Relevance of CORMs

This section deals with the physiologic functions and the possible therapeutic applications of carbon monoxide (CO). For detailed reading about cellular and biochemical functions of CO the interested reader is referred to the articles cited in the text and to various reviews like Ref. [162–164]. Carbon monoxide has long been considered as a perilous gas not to be smelled or visibly detected by man. Despite of that harmful property, CO has been identified as an important signaling molecule besides nitric oxide (NO) [165] and hydrogen sulfide (H_2S) with various functions and effects in higher organisms [166–169]. Depending on the local concentration, CO has different effects on the mammalian body. Inhalation of a high systemic concentration turns the detoxification mechanisms of heme into a lethal effect as CO shows a binding affinity to heme about 230 times larger than molecular oxygen [170]. Local concentrations either high or low can have a number of up- or downregulating effects on ion channels [167,169], inflammation, vascular tone and other gasotransmitter-regulated biochemical processes. One of the most interesting properties of high local CO concentrations is its anti-proliferative effect which could lead to efficient treatment of cancerous tissue. However, when CO is administered in its gaseous form, dosage is a challenging task. Therefore, chemical carriers which render possible a controlled release of CO by an adequate trigger are desirable. Different approaches to accumulate theses prodrugs in certain tissues and to trigger the release of CO are followed nowadays. Potential CO carriers have to be soluble

in physiological media and stable under air and in water until the release is triggered. Such prodrugs are called CO-releasing molecules since their potential as safe-to-handle CO carriers has been ascertained [171]. Due to strong binding, good release properties, and better toxicological properties, transition metal complexes are preferred over organic compounds [164]. Nevertheless, there are also promising examples of metal-free CORMs [172,173].

Targeted delivery at certain tissues is tried to be achieved by designing the complex's ligand periphery properly, e.g., by attaching peptides at one ligand [174] or by including the CORM into macromolecular transporter compounds. Several release mechanisms of CO are nowadays tracked. One among them is ligand exchange in solution. Hereby, a CO ligand is exchanged by a nucelophilic ligand with a higher binding affinity, e.g., amino acids [175]. This approach is limited for therapeutic applications as CO is already substituted by constituents of the medium and unspecific tissue, thereby shortening the time for targeted delivery in the desired tissue [164]. Other stimuli for CO release can be enzyme activity [176], magnetic heating mediated by metallic nanoparticles [177], or redox processes at the central metal atom [163]. Probably the most prominent CO release mechanism is photolysis of an appropriate metal–carbonyl complex. Schematically, a transition metal (M) complex with x ligands L attached to it gets photolyzed by a photon,

$$\mathrm{ML}_x(\mathrm{CO})_y \xrightarrow[-\mathrm{CO}]{h\nu} \mathrm{ML}_x(\mathrm{CO})_{y-1} \xrightarrow{\mathrm{L}'} \mathrm{ML}_x\mathrm{L}'(\mathrm{CO})_{y-1}, \tag{5.1}$$

releasing one of the y CO molecules attached. The ligand L'—which can also be a solvent molecule or a free moiety of a chelating ligand—is filling the free coordination site afterwards. These CO prodrugs are called photo-CORMs [178,179]. A short overview of the photochemistry of such CO complexes (Section 5.2) is given as the basis for the experiments presented in Section 5.3 to 5.4 in which the results of time-resolved spectroscopy on a Manganese–carbonyl complex are presented.

A great advantage of light as a CO-release trigger is that it can conveniently be focused with intensities high enough to start the CO release. Therefore, photo-CORMs should allow precise disposal of CO in the irradiated tissue. With that comes the question of penetration depth of light into tissue and especially skin. As most metall-centered photo-CORMs mainly absorb in the UV where low skin transparancy makes in vivo photoactivation challenging, it is desirable to develop photo-CORMs absorbing in the visible or near-infrared spectral regime [173,180–182]. Another approach is to stimulate the CO release by absorption of two photons. During the supervision of a Bachelor thesis, a setup for measuring the two-photon absorption (TPA) with a mid-infrared detection was developed [9, 183]. Two-photon absorption is not only advantageous over one-photon absorption because of the higher penetration depth in tissue but also since the risk of photodamages is much smaller due to off-resonance [164].

One recent invention in photo-CORMs are *i*CORMs, i.e., CORMs with a chelating ligand which saturates the free coordination site intramolecularly to result in an *inactivated* CORM (*i*CORM) which will not trigger unspecific reactions [184]. Their investigation is advantageous as with normal photo-CORMs anti-proliferation effects of the cleaved metal complex cannot be excluded unambiguously. Especially the remaining complexes after CO liberation are difficult to analyze and to characterize.

5.2 Photochemistry of CORMs

Metal carbonyls are a class of compounds known for over 100 years. Their photochemical behavior has been extensively studied. Hence, the photoproducts are often well known and the photochemical reactions are used in plenty of preparative conversions. The following section gives a short introduction to metal–carbonyl photophysics and -chemistry. For detailed description the reader is referred to textbooks [185,186] and the cited literature in this section.

Several electronic transitions are in principle possible in organometallic complexes. In a simplified picture, one classifies these transitions depending on which part of the complex the involved molecular orbitals are located [185, 186]. Transitions mainly centered at the central metal atom are called ligand-field excitations or d–d transitions as in the case of transition metals mainly d-orbitals are involved. As in organometallic chemistry the metal–ligand binding is of covalent nature, metal–ligand bonds will also be altered by a d–d excitation [185]. Due to this, it is sometimes challenging to differentiate between d–d transitions and metal-to-ligand excitations mentioned below. In contrast to that, $n \rightarrow \pi^*$ and $\pi \rightarrow \pi^*$ transitions located on a ligand are called intraligand transitions. Whether a transition in the ligand changes significantly upon complexation or not depends on the perturbation induced by the binding, i.e., which and to what extent ligand orbitals are involved in the binding to the central atom [185]. Transitions between the metal atom and the ligand sphere are called according to their sense of direction either metal-to-ligand charge transfer (MLCT) or ligand-to-metal charge transfer (LMCT) transition. As in general metal d-orbitals are relatively high in energy, this kind of transition is observed only rarely. It should be mentioned for the sake of completeness that optical excitation of metal-to-solvent charge transfer and metal-to-metal transitions (at least for bimetallic complexes) are possible in organometallic compounds [185].

Independent from the excitation wavelength, $CpMn(CO)_3$ (Cp = cyclopentadienyl) shows a quantum yield of unity for the photochemical CO release in cyclohexane with acetone or diphenylacetylene as added donor molecules D [187]. In *i*-octane the quantum yield drops to 0.65. Upon further irradiation, the photochemically formed dicarbonyl $CpMn(CO)_2D$ with an additional donor molecule, e.g., a solvent molecule, can be further photolyzed [188]. For $CpMn(CO)_3$ (with Cp = cyclopentadienyl and derivates thereof) in alkane solution, the $\pi \rightarrow \pi^*$ intraligand transition ($\sim$ 250 nm) is higher in energy than the metal-to-ligand transition (325–350 nm) [185].

For some metal carbonyls, ultrafast dynamics have been studied. The photodissociation of $Fe(CO)_5$ has been investigated in a large number of studies in the gas phase as well as in solution. Gas phase experiments were elaborated by transient ionization including different excitation wavelengths [189–191] and by electron diffraction [192]. Whether only one or up to all CO ligands are photolyzed off in the gas phase depends on the selected excitation wavelength. Quantum control with shaped femtosecond pulses was carried out allowing for the enhancement of one dissociation channel [193, 194]. $Fe(CO)_5$ has also been studied in the liquid phase by transient absorption both in the infrared [195–198] and X-ray [199, 200] spectral regime. Depending on the solvent, either one or two CO ligands are liberated upon UV excitation [196–198]. Another well-studied metal carbonyl is $Mn_2(CO)_{10}$ (CORM-2) which shows two different dissociation products both in the gas phase [201] and in the liquid phase [202–204] upon UV irradiation. In solution, the ratio between the metal–metal dissociation [$^{\bullet}Mn(CO)_5$ + $^{\bullet}Mn(CO)_5$] to the metal–CO dissociation [$Mn_2(CO)_9$ + CO] depends on the

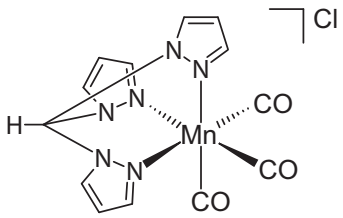

Figure 5.1: Molecular structure of tpm-CORM. The symmetry group is C_{3v} due to the *facially*-ligated octahedral complex structure.

excitation energy. Both photoproducts show geminate recombination to a certain extent [204]. Excitation at the red edge of the metal-centered ligand-field absorption band at 400 nm leads mainly to the monometal fragment $^{\bullet}Mn(CO)_5$ [205].

Changes in hapticity to fill free coordination sites [206] as well as chelation upon CO liberation [184,207] is a common intramolecular photochemical process in carbonyl complexes. The dynamics of carbonyl complexes with chelating ligands similar to those which are used as *i*CORMs (see above) has already been studied for manganese tricarbonyl complexes with different chelating ligands [208–210].

Although the dynamics of CO complexes have been studied in a large variety of solvents, water as the most relevant solvent for physiological studies and applications has been addressed only recently (see Refs. [2] and [3] as well as Sections 5.3 to 5.4). The only exceptions were the experiments of CO release from heme proteins [211,212] and the study of CO vibrations in $Mn_2(CO)_{10}$ [213–215]. A mechanistic question which is of importance for CORMs is whether several CO ligands are liberated in a sequential or concerted manner. Towards a better understanding of the CO release mechanism, the ultrafast photochemistry of a Manganese tricarbonyl CORM is outlined in the following sections.

5.3 Spectral Properties of tpm-CORM

The molecular structure of $[Mn(CO)_3(tpm)]Cl$ [216] with a facially-ligating tris(2-pyrazolyl)-methane (tpm) ligand is depicted in Fig. 5.1. The compound is termed tpm-CORM in this thesis due to reasons of better readability. The following subsections describe the steady-state absorption spectra of tpm-CORM as well as femtosecond time-resolved experiments for one and two identical pump pulses with mid-infrared probe detection.

The cytotoxic properties due to light-activated CO release of tpm-CORM have been shown earlier [216,217]. Depending on these studies it was concluded that two [217] or three [218] equivalents of CO per mole of tpm-CORM with hexafluorophosphate as counterion were liberated upon UV irradiation in myoglobin assays. The experimetal findings outlined below indicate that initially only one CO ligand is photochemically released. The normalized UV/Vis absorption spectrum and the absorption in the MIR absorption spectrum of tpm-CORM dissolved in heavy water (D_2O) are both shown in Fig. 5.2a,b.

The UV absorption spectrum (Fig. 5.2a) shows a strong absorption in the far UV as well as two distinct bands around 265 and 350 nm which will be assigned below. In the transient absorption experiments described in Subsection 5.4 both bands are excited making use of two different pump wavelengths. The mid-infrared absorption (Fig. 5.2b) shows two features at-

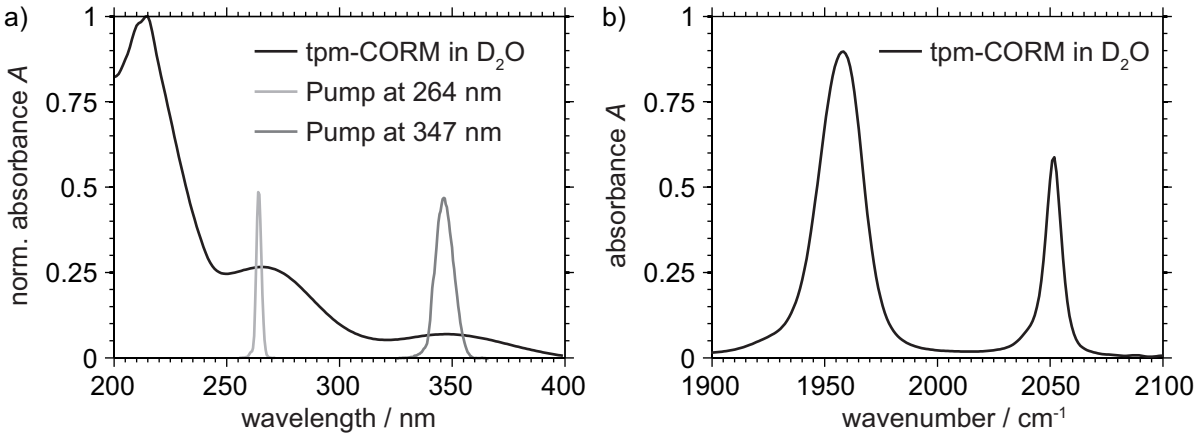

Figure 5.2: UV/Vis and infrared absorption spectra of tpm-CORM in D_2O. a) The normalized UV/Vis spectrum of tpm-CORM dissolved in D_2O shows three major contributions. The band around 260 nm is attributed to a MLCT excitation with both contributions of the tris(pyrazolyl) and the CO ligands. The band around 350 nm is assigned to a transition from the metal center to a delocalized state on the metal and the CO ligands. The spectra of the pump pulses (see Section 5.4) are centered around 264 and 347 nm, respectively. b) The infrared absorption shows two CO stretching bands. The absorptions at 2051 and 1958 cm^{-1} corresponds to the symmetric and the antisymmetric stretching mode of CO, respectively. With tpm-CORM possessing C_{3v} symmetry, the antisymmetric stretching mode is degenerated. Adapted with permission from Ref. [3]. Copyright (2013) American Chemical Society.

tributed to the symmetric (2051 cm^{-1}) and antisymmetric CO stretching modes (1958 cm^{-1}), respectively. tpm-CORM posseses C_{3v} symmetry, hence the antisymmetric stretching mode is degenerated. Heavy water was preferred over H_2O in this study as in the mid-infrared region where the CO stretching modes are located (Fig. 5.2b) D_2O shows less absorption than its lighter isotopologue [219]. Water and heavy water show no significant absorptions above wavelengths of 200 nm [220], i.e., the resonant absorption of the solvent can be neglected in the following considerations.

Time-dependent density-functional theory (TDDFT) calculations of the cationic complex in the gas phase carried out with ORCA 2.6 [221] revealed the nature of the transitions induced with the UV pump pulses used in Section 5.4. Both pulses are centered at the two separated absorption bands of the electronic absorption spectrum of tpm-CORM [2]. The highest occupied molecular orbitals (HOMOs) and the lowest unoccupied molecular orbitals (LUMOs) are shown in Fig. 5.3.

The electron densities of all three HOMOs highest in energy (HOMO−2, HOMO−1, HOMO, see lower row Fig. 5.3) are mostly localized at the Manganese atom corresponding to three doubly filled 3d orbitals of the $3d^6$ low spin complex with some contributions from the bonding of CO to the central atom. Whereas LUMO and LUMO+1 (Fig. 5.3, upper row, left part) show localized electron density on the tpm ligand, LUMO+5 (Fig. 5.3, upper row, middle) shows electron density at all CO ligands. The corresponding transitions at 264 nm excitation suggest that part of the excitation will not result in a CO liberation but in an intraligand excitation. Anyhow, the excess energy of a UV photon of 264 nm wavelength is sufficing for cleaving a Mn–C bond [222]. In case of the lower-energy excitation at 347 nm, where the final LUMO+2 and LUMO+3 (Fig. 5.3, upper row, right part) exhibit electron density delocal-

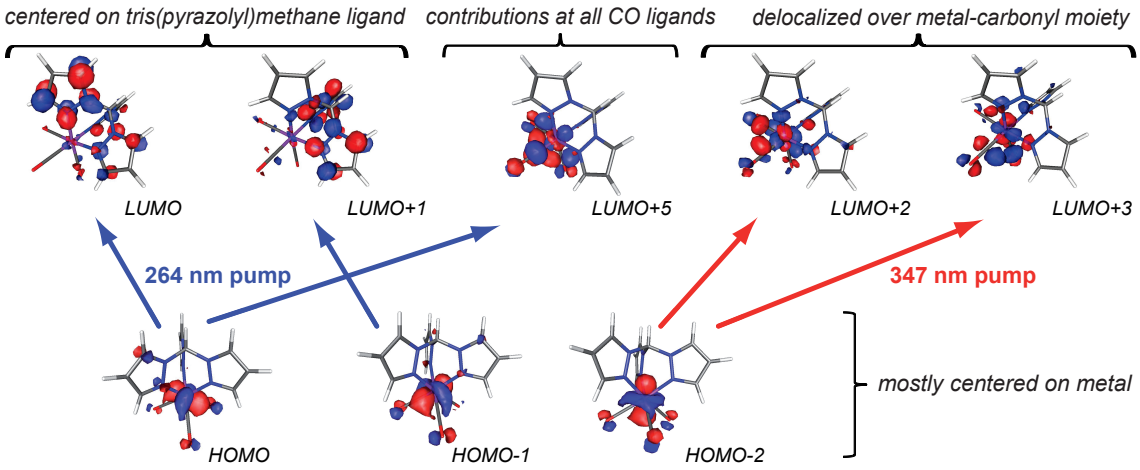

Figure 5.3: TDDFT calculations for the dominating electronic transitions induced with the employed pump pulses. Whereas the three involved HOMOs exhibit an electron density mostly located at the manganese atom, the character of the accessible LUMOs varies strongly. Reprinted with permission from Ref. [2]. Copyright (2013) American Chemical Society.

Table 5.1: Calculated CO stretching wavenumbers $\tilde{\nu}$(CO) for presumable CORM photoproducts. The subscript sym or asym denotes whether the CO stretching mode is symmetric or asymmetric. Data reprinted with permission from Ref. [2]. Copyright (2013) American Chemical Society.

molecule	scaled DFT wavenumber / cm^{-1} (assignment)		
$[Mn(CO)_3(tpm)]^+$	1943 ($\tilde{\nu}_{asym}$),	1943 ($\tilde{\nu}_{asym}$),	2036 ($\tilde{\nu}_{sym}$)
$[Mn(CO)_2(tpm)]^+$	1885 ($\tilde{\nu}_{asym}$),	1975 ($\tilde{\nu}_{sym}$)	
$[Mn(CO)_2(tpm)(D_2O)]^+$	1864 ($\tilde{\nu}_{asym}$)	1955 ($\tilde{\nu}_{sym}$)	
$[Mn(CO)(tpm)]^+$	1875		
$[Mn(CO)(tpm)(D_2O)]^+$	1833		
$[Mn(CO)(tpm)(D_2O)_2]^+$	1821		
$[Mn(CO)_3(\kappa\text{-C-tpm})]^+$	1915 ($\tilde{\nu}_{asym}$),	1920 ($\tilde{\nu}_{asym}$),	1978 ($\tilde{\nu}_{sym}$)

ized over the metal and all or two carbonyl groups, one might assume increased antibonding character of the Mn–CO bond and therefore CO release upon irradiation.

In order to relate the spectral signatures shown in Section 5.4 with possible photochemical intermediates formed from tpm-CORM after irradiation, Table 5.1 lists calculated CO stretching wavenumbers $\tilde{\nu}$(CO) of the intact CORM cation, dicarbonyl and monocarbonyl products with and without additional D_2O ligands attached, as well as the isomerization product, where one pyrazolyl ring of the tpm ligand is ligating with a C instead of an N atom ("carbene isomer" $[Mn(CO)_3(\kappa\text{-C-tpm})]^+$) [2]. The DFT calculations were carried out with Gaussian 09 [223]. The correlation functional B3LYP was employed with the basis set 6-311+G-(d,p). To account for the solvent, the polarizable continuum model (PCM) was included into the calculations. The obtained vibrational wavenumbers were scaled with a factor from Ref. [224]. Details on the calculations can be found in Refs. [9,225].

It can be seen from Table 5.1 that the position of both CO stretching bands shift to lower wavenumbers for the dicarbonyl photoproducts with or without a D_2O molecule attached. For

the monocarbonyl species, the absorption shifts to lower energies the more solvent molecules coordinate the central atom, as σ-donation of electron density strengthens the π-backbonding from Manganese to CO and therefore tightening the metal–CO bonding. The vibrational wavenumbers of the carbene isomer are shifted to even lower wavenumbers and more remarkably, the difference between the symmetric and the antisymmetric CO stretching band gets significantly smaller compared to the intact CORM. The abovementioned orbital contributions as well as the CO stretching wavenumbers of probable photoproducts will be used to assign the spectral signatures to molecular processes and intermediates in the following experimental section.

5.4 Transient Absorption Spectroscopy of CORMs

For monitoring the CO release dynamics of CORMs probing in the mid-infrared spectral region is the method of choice. Especially in metal carbonyls, the CO stretching mode is a sensitive probe for binding situations and number of CO ligands attached to the central metal atom. The following subsections describe the experiments performed on tpm-CORM with excitation by a UV pump pulse and probing the molecular dynamics with MIR pulses. Additionally, pump–repump–probe experiments are presented with double-pulse excitation in the UV.

5.4.1 UV-Pump–MIR-Probe Spectroscopy

In the presented work, tpm-CORM was excited with different pump wavelengths, namely with pump pulses centered around 264 nm and 347 nm (see pump spectra in Fig. 5.2a). The transient maps of the time-resolved experiments are shown in Fig. 5.4a and 5.4b for excitation at 264 and 347 nm, respectively. In principle, dynamics for both excitation wavelengths are similar, the only difference being a slightly more distinct signal of the excited but intact CORM above 2060 cm^{-1} for the 264 nm pump pulse (see below).

Both data sets show an oscillatory feature at the spectral positions of the absorptions of the CO streching mode for $\tau < 0$. This pattern arises from the free induction decay which is due to a pump interaction with the polarization induced by the probe [226, 227]. For delay times $\tau \approx 0$, there are strong positive contributions along the entire probing range which last for a few hundred femtoseconds. These signals are due to the absorption of hydrated electrons present in water for two-photon UV excitation [228]. Another contribution to this signal might be a short-living increased absorption of the probe pulse by the CaF_2 window of the sample cell due to a pump-induced change in transmission [229]. The short signal around time zero disguises the dynamics over the whole probing range, complicating quantitative statements about dynamics for short delay times. For detailed interpretations transients at selected probing wavenumbers are depicted in Fig. 5.5.

For excitation at both pump wavelengths the ground-state bleachings of the CO stretching modes can be seen around 1958 and 2051 cm^{-1}, corresponding to the two steady-state absorption bands in Fig. 5.2b. The ground-state bleaching does not recover within a delay time up to nanoseconds what can be seen in the transients for a probe wavenumber of 1951 and 2052 cm^{-1} (Fig. 5.5a,b). The persistent ground-state bleaching signals are a clear indicator that at least one CO ligand has been released from tpm-CORM and that the free coordination

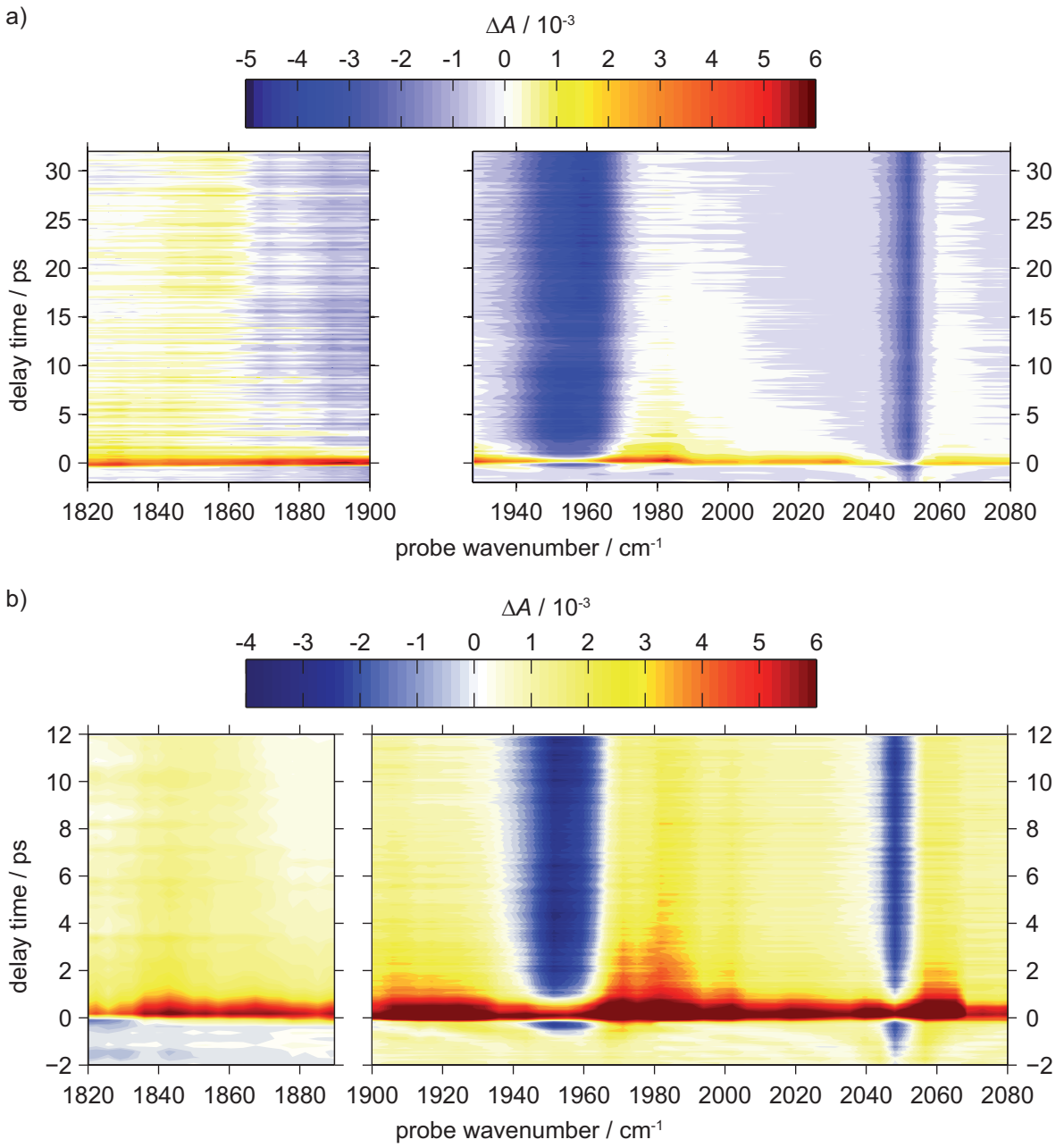

Figure 5.4: Transient absorption maps of the tpm-CORM for different pump wavelengths. a) Transient absorption of the CORM, recorded with 264 nm pump and MIR probe pulses. Adapted with permission from Ref. [2]. Copyright (2013) American Chemical Society. b) Transient absorption of the CORM, recorded with 347 nm pump and MIR probe pulses. Transients for selected wavenumbers after 347 nm excitation are analyzed in Fig. 5.5 to explore the involved dynamic processes. Adapted with permission from Ref. [9]. Copyright (2014) Dr. Philipp Rudolf.

site has been filled by D_2O. The CO liberation and photoproduct solvation occurs within the first few picoseconds where the difference signal is blurred by the hydrated electron signal.

Around probe wavenumbers of 1980 and 1850 cm^{-1} positive signals are visible ranging up to several nanoseconds (Fig. 5.5c,d). These two product absorption (PA) bands match the

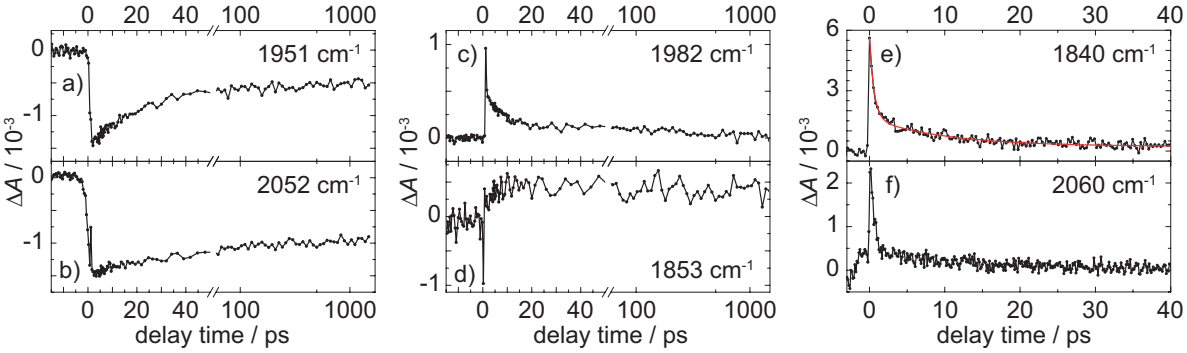

Figure 5.5: Single transients for exemplary wavenumbers; Panels a) to d) were recorded for delays of up to 1.5 ns and with 347 nm pump pulses; note the change from a linear (-15 to 50 ps) to a logarithmic abscissa (>50 ps). Negative (a and b) and positive (c and d) signals persist for the full delay; Panels e) and f) show a shorter time scale to visualize cooling contributions that decay within the first 20 ps; f) was recorded with 264 nm excitation. Adapted with permission from Ref. [2]. Copyright (2013) American Chemical Society.

wavenumbers of the CO stretching of long-living dicarbonyl species. Although the energy for cleaving a Mn–CO bond is overcome several times by a UV photon of 264 or 347 nm wavelength, there is no evidence on ultrafast time scales that more than one CO ligand is photolyzed off. Hence, when the excess energy of the pump pulse does not lead to further CO liberation the energy must be transferred fast to vibrational modes of the dicarbonyl photoproduct. The transferred excess energy is large enough to excite several vibrational quanta of the CO stretching modes. Whereas several hexacarbonyls are known to possess vibrationally hot carbonyl stretching bands [230], dicarbonyls do not show formation of vibrationally hot bands upon photolysis [229]. Hence, it can be deduced that the excess energy is distributed among low-energy frequencies of the dicarbonyl photoproduct. These low-energy modes couple to the CO stretching before the excited molecule has relaxed by dissipation of the excesss energy to the bath. The PA bands around 1850 and between 1980 and 2000 cm^{-1} are initially broadened and narrow within the first few picoseconds upon vibrational cooling. To quantify the cooling, an isolated product band at 1840 cm^{-1} was fitted with the sum of two decaying exponential functions [cf. Eq. (2.11)]. The result are two lifetimes of (0.6 ± 0.1) ps and (10 ± 1) ps (see red line in Fig. 5.5e). Although the signal at short delay times is disguised by the processes discussed above, the first lifetime matches the solvent reorganization time scale of water [231]. The second contribution clearly corresponds to the cooling of the hot dicarbonyl. The hexacarbonyls mentioned above show vibrational cooling of low-energy modes within a few tens of picoseconds in alkaneous solutions [230, 232] whereas vibrational relaxation in water and heavy water is reported to be on the order of some picoseconds [213, 214]. Hence, reorientational dynamics and the highly flexible solvent shell of water assist the fast cooling of the dicarbonyl photoproduct due to the high receptivity of energy mediated via vibrations.

Another aspect of CORM-photochemistry is the number of released CO ligands. On ultrafast time scales no formation of a photoproduct with less than two CO ligands is observed. Furthermore, not every excitation leads to CO release as some of the cleaved complexes might reform by geminate recombination [232]. The actual amount of CORMs which undergo CO liberation cannot be determined as the different contributions which obscure the signal for

short delay times (see above) prevent a comparison of the bleaching recovery with the initial ground-state bleaching. The geminate recombination can be analyzed by the signals stemming from the unviolated CORM. For short delay times τ a partial recovery is observed in the ground-state bleaching of the antisymmetric stretching band (Fig. 5.5a). Since geminate recombination occurs within a few hundred femtoseconds with a simultaneous broadening of the absorption, the recovery is in fact due to cooling and not due to recombination dynamics [232]. Part of the recovery might also arise from the cooling dynamics of the dicarbonyl photoproduct at the high-energy side of the ground-state bleaching. Hence above 2000 cm^{-1} no photoproduct absorption can be detected, the line broadening due to geminate recombination is better visible in the region of the symmetric stretching mode around 2050 cm^{-1}. Upon coupling of the vibrationally hot CO stretching to low-frequency modes a positive signal arises around 2060 cm^{-1} which remains as long as the recombined CORM is vibrationally still excited (Figs. 5.5b and 5.5f, although transient f was recorded for a different pump wavelength it is similar for both pump pulses).

A third issue that has to be taken into account is excitation which does not lead to CO liberation at all. As could already be seen from the TDDFT calculations in Fig. 5.3, some transitions do not lead to transfer of electron density to CO ligands. From transient absorption spectroscopy one cannot differentiate between uneffective excitations and geminate recombination. Yet, several observations substantiate the probability of non-dissociative excitations. The transitions attainable with the pump pulse at 264 nm are located predominantly on the tpm ligand, implying less release of CO for this pump wavelength. This is also confirmed experimentally as the transient absorption of intact tpm-CORM around 2060 cm^{-1} is less pronounced for the lower-energetic excitation pulse at 347 nm. When the UV/Vis absorption spectrum of tpm-CORM (Fig. 5.2a) is considered, the quantum yield for CO release should be three times higher for the 264 nm pump pulse than for 347 nm excitation as the absorption is about three times lower for the lower-energy band. However, such a difference in CO release is not observed experimentally.

5.4.2 UV-Pump–UV-Repump–MIR-Probe Spectroscopy

Whether tpm-CORM can be further photolyzed or not can be addressed by carrying out pump–repump experiments. With the interferometric setup described in Section 2.6.2 tpm-CORM was excited with two copies of the pump pulses at 264 and 347 nm, respectively. The delay time between the pump and the repump pulse was adjusted to τ_{PR} = 200 ps. The repump–probe delay time was set to τ_{RPr} = 200 ps where cooling processes of doubly excited CORMs can be regarded as completed. Even at pump energies high enough to excite about one quarter of the probed sample volume with one pump pulse, i.e., that at least a few percent of the tpm-CORM should be excited twice with the pump and the repump pulse, no significant new absorption of monocarbonyl photoproduct species could be detected. Possible explanations of the lack of a monocarbonyl species are as follows. Although dicarbonyls can in principle be photolyzed [229] and also dicarbonyl photoproducts can be further photolyzed [188] it might be the case that the dicarbonyl from the parent tpm-CORM does not show sequential CO liberation at all. Indeed, for manganese centered carbonyls the dissociation energy is about 50% higher for the cleavage of another CO ligand when water filled the free coordination site after release of one CO ligand [233]. Nonetheless, the excess energy of a UV photon should also be sufficient for

another dissociation process. An explanation might be that instead of a second CO ligand the coordinated D_2O ligand is detached again as it was observed for solvated pentacarbonyl complexes photochemically obtained from $M(CO)_6$ (M = Cr, Mo, W) [187]. As the recombination of D_2O with the remaining complex after repumping is faster than the experiment's temporal resolution, this process cannot be distinguished from ineffective bond cleavage. Another possible explanation might be a shift in the absorption spectrum of the dicarbonyl in the ultraviolet spectral regime so that absorption of a repump photon is more unlikely. This hypothesis is assured as e.g., in case of $CpMn(CO)_3$, a strong red-shift is observed for the photochemical CO release [234]. In addition to that, for another CORM similar to the tpm-CORM a shift in the lowest-lying absorption band by 25 nm was reported under soft irradiation conditions, i.e., when only one CO ligand should be released [235]. Therefore, non-degenerate pump–repump spectroscopy with another repump wavelength should be carried out in future experiments.

5.5 Conclusion and Outlook

In conclusion, the UV-induced photolysis dynamics of tpm-CORM dissolved in heavy water were studied. Whereas excitation with different pump wavelengths leads to CO liberation with the free CO ligand going to the solvent and a D_2O molecule saturating the free coordination site, not every excitation leads to cleavage of a Mn–CO bond. Also, some dissociated complexes undergo geminate recombination leading to formation of broadened CO-stretch absorption bands due to coupling of low-frequency modes of the intact CORM to the hot CO stretching modes. Relaxation of the low-frequency vibrations occurs quickly via a water-assisted cooling mechanism in about 10 ps.

In the future, the fact that the quantum yield of CO release from tpm-CORM is smaller than unity could be confirmed by experiments where photolysis excitation spectra are recorded by measuring the amount of released CO with respect to the excitation wavelength. In pump–repump–probe experiments no clear indication for the photolysis of the dicarbonyl was detected. One reason for that might be a shift of the UV absorption of the dicarbonyl CORM. Therefore, UV probe-pulse experiments should be employed in addition to the studies presented here.

Since tpm-CORM is a potential candidate for biological and therapeutical CO release in vivo, for reasons of higher penetration depth and less photodamage upon excitation in the visible spectral regime excitation by two-photon absorption (TPA) should be considered. A possible experimental setup to investigate the time-resolved two-photon absorption properties with detection in the mid-infrared was co-developed in the course of this thesis and presented in Refs. [9, 183].

6 Ultrafast Photochemistry of a Tetrazolium Salt

The experiments presented in this chapter were carried out in a cooperation with Prof. Dr. Patrick Nürnberger. Some of the results were already presented in the Bachelor thesis [236] of Domenik Schleier who was supervised during the project that resulted in this thesis. Parts of the text and the figures in the following chapter will be used and modified in publications currently in preparation [6,7].

Since the first synthesis in 1894 [237], tetrazolium salts have been utilized in a multitude of applications, from chromatographic sugar determination [238,239] to biological assays for quantifying cell growth and viability [240,241], widely used in cancer research [242,243] and agriculture [244, 245]. Tetrazolium salts furthermore exhibit a rich photochemical behavior. In this chapter, the focus will be on the tetrazolium salt photochemistry, especially on an ultrafast time scale. For a more detailed overview on tetrazolium salts, their properties, and their applications in chemistry and biology the interested reader is referred to textbooks [246–248], reviews [249–251], and the cited references in the text.

In the scope of this thesis, the photochemistry of tetrazolium salts combines both reaction sequences from Chapters 4 and 5, namely ultrafast electron transfer in combination with the cleaving and the formation of a molecular bond. Therefore, tetrazolium salts are suitable exemplary systems which combine different light-induced reaction steps in a complex reaction sequence.

Section 6.1 gives an overview of the photochemistry of tetrazolium ions both from literature and results obtained in this thesis. Apart from steady-state absorption measurements, also irradiation experiments were performed to confirm and establish the photoproducts of tetrazolium salts in different solvents. Transient-absorption measurements are presented in Section 6.2 to compare the long-term conversion of a tetrazolium salt with its ultrafast dynamics and possible short-living intermediates. Finally, in Section 6.3 the experiments are summarized and future experiments concerning the photoinduced dynamics of the photoproducts itself are outlined.

6.1 Photochemistry and Spectral Properties of Tetrazolium Salts

Apart from their complex redox behavior, tetrazolium salts show a multifaceted photochemistry as well. Since the pioneering photochemical studies on tetrazolium salts in the 1940s and 1950s [252–256], there have been some studies on the photochemistry of tetrazolium ions. So far, few time-resolved studies exist but only with a temporal resolution of microseconds [257]. Time-resolved studies of tetrazolium salts with femtosecond time resolution are shown in Section 6.2.

The work on the photochemistry of the tetrazolium salt 2,3,5-triphenyl-tetrazolium chloride (**TTC**, Scheme 6.1) by Hausser et al. [254] showed that the final photoproducts depend on the solvent environment (Scheme 6.1). In water, both the ring-open 1,3,5-triphenyltetrazolium formazan (**TPF**) and the polycyclic biphenylene product 2-phenyl-benzo[*c*]tetrazolo[2,3-*a*]-cinnolin-4-ium (**PTC**) are formed upon irradiation with UV light (Scheme 6.1). However, in alcoholic solutions only **PTC** is formed. Several studies [246] concluded that a disproportionation reaction involving two **TTC** molecules is responsible for this difference, yet without

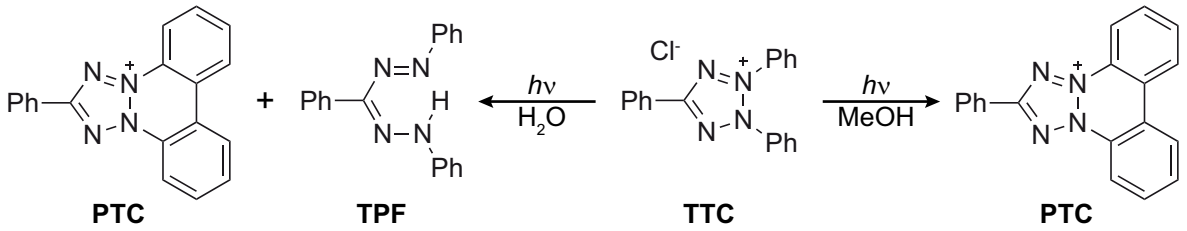

Scheme 6.1: Solvent-dependent photochemistry of **TTC**. Depending on the solvent, either **PTC** (alcoholic solution) or a mixture of **PTC** and the ring-open formazan **TPF** (aqueous solution) is formed upon irradiation with UV light.

identifying the intermediates. Electron spin resonance (ESR) experiments later disclosed that a cyclic tetrazolinyl radical (**TTC**$^{\bullet}$, Scheme 6.2) is involved in the process [258–260], which was confirmed by electrochemistry [261–263]. The decay of the tetrazolinyl radical **TTC**$^{\bullet}$ could be followed in flash-photometry [257] and pulsed-radiolysis studies [264] with microsecond time resolution. Despite the prevalent applications of tetrazolium salts, the reaction mechanism leading towards the formation of the intermediate tetrazolinyl radical **TTC**$^{\bullet}$ has not been addressed.

Figure 6.1a shows the absorption spectrum of **TTC** in water (orange), acidic phosphate-buffered solution at pH 5 (green) and in methanol (blue). The intensity profile of the UV pump pulse (see below) is shown in violet. The absorption of the photoproducts **PTC** (green) and **TPF** (red) in methanolic solution are compared to the absorption of **TTC** (blue) in Fig. 6.1b. The photoproduct **PTC** with absorption maxima at 260 and 350 nm is obtained in situ in methanol after irradiation of a **TTC** solution (see below) and shows cerulean fluorescence [254] upon excitation at 375 nm (Fig. 6.1c).

The photochemical behavior of **TTC** known from literature is reproduced by irradiation experiments of **TTC** solutions. Figure 6.1d shows the absorption spectra of **TTC** solutions in water (red) and methanol (green), respectively, after irradiation with an array of UV light-emitting diodes (central emission at $\lambda = 369$ nm). For the methanolic solution, the absorption shows a shift of the main absorption band from about 250 to 260 nm and an absorption band around 350 nm. Both absorption bands are assigned to **PTC** [254]. No formation of formazan can be observed in this case. The irradiated aqueous solution shows the formation of **PTC** as well (Fig. 6.1d). A weak absorption between 450 and 600 nm can be detected on top of an offset particularly for wavelengths above 300 nm. The new absorption band corresponds to the formation of **TPF** which shows a low solubility in water. Therefore, scattering of light by precipitated formazan particles leads to a broadband absorption (Fig. 6.1d).

6.2 Transient Absorption Spectroscopy of TTC

This section presents the first ultrafast investigations of a tetrazolium salt in different solvents. The ultrafast dynamics of **TTC** are studied in water, various alcohols, in acidic buffered solution, and in DCM. The usage of different solvents, an advanced data-fitting procedure, and correlation of the results to various solvent parameters unravel the nature of the intermediates of **TTC** photochemistry.

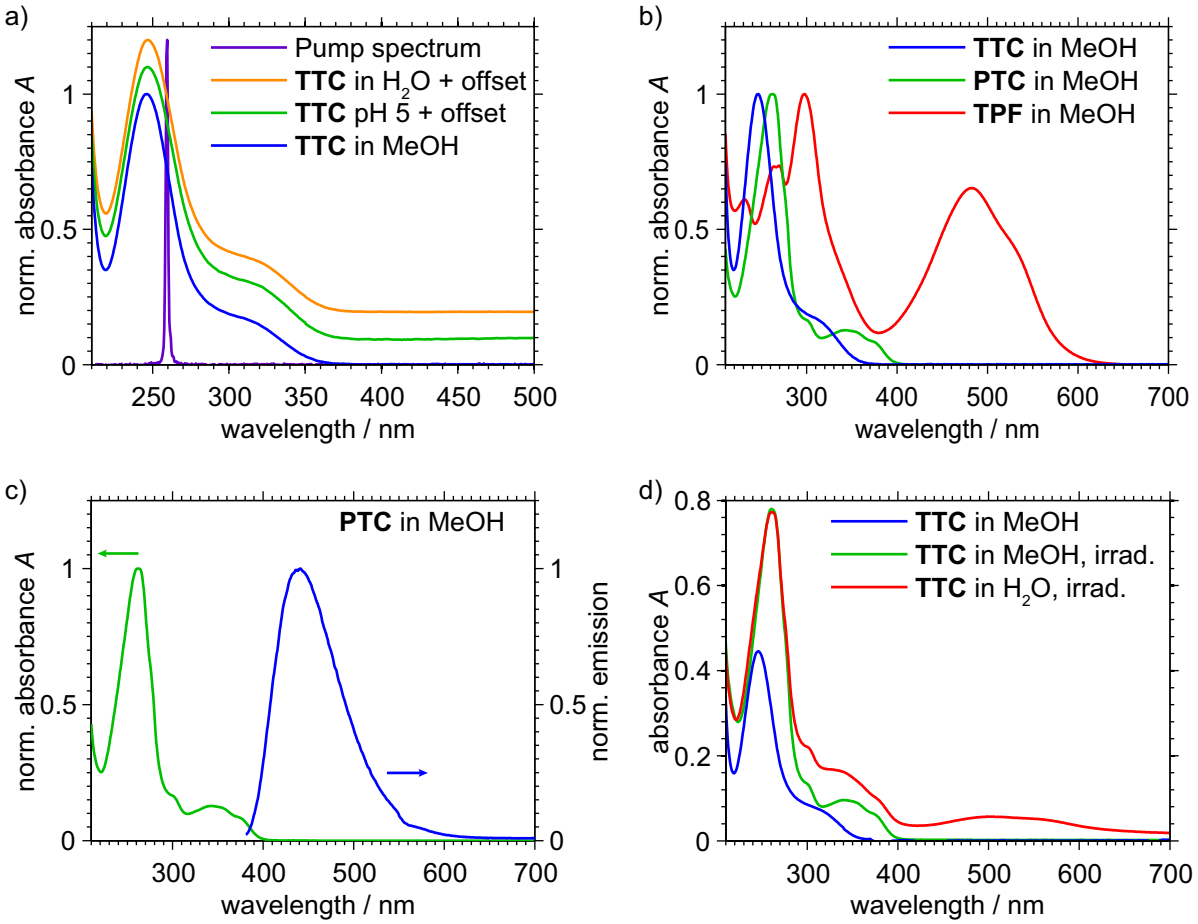

Figure 6.1: Absorption spectra of the studied compounds. a) The normalized absorbance of **TTC** is depicted in orange and blue for solutions in water and methanol, respectively. The absorbance of **TTC** at pH 5 in buffered solution is given in green. Note that a vertical offset was added for clarity. The spectrum of the femtosecond pump pulse centered at 260 nm (Section 6.2) is given in violet. b) The normalized absorbance of **PTC** in methanol is indicated in green, the one of formazan **TPF** in red. For comparison, the absorbance of **TTC** in methanol is given in blue. c) Excited at the lowest-energy absorption band at 375 nm (green), **PTC** shows fluorescence emission centered at 440 nm. d) When a methanolic solution of **TTC** (blue) is irradiated, only **PTC** (green) is formed. Irradiated aqueous solutions of **TTC** (red) yield both **PTC** and **TPF**, with a broad onset for wavelengths $\lambda \geq 300$ nm. The onset stems from precipitated formazan particles leading to scattering of light. In both irradiation experiments the irradiation time was 80 min.

While solutions of **TTC** and of **PTC** do not exhibit any absorption in the visible spectral regime, the formazan **TPF** has a characteristic absorption centered around 490 nm (see Fig. 6.1). Hence, any absorption signals in the visible which do not match the absorption spectrum of **TPF** originate from excited species or reaction intermediates. For the transient absorption experiments the excitation-pulse energy is set to 200 nJ at 260 nm.

The ultrafast photodynamics within the first 100 ps after UV excitation of **TTC** are displayed as transient difference spectra in Fig. 6.2 for water (panel a) and methanol (panel b), disclosing that the behavior is remarkably similar in both solvents. Initially, a broad and in-

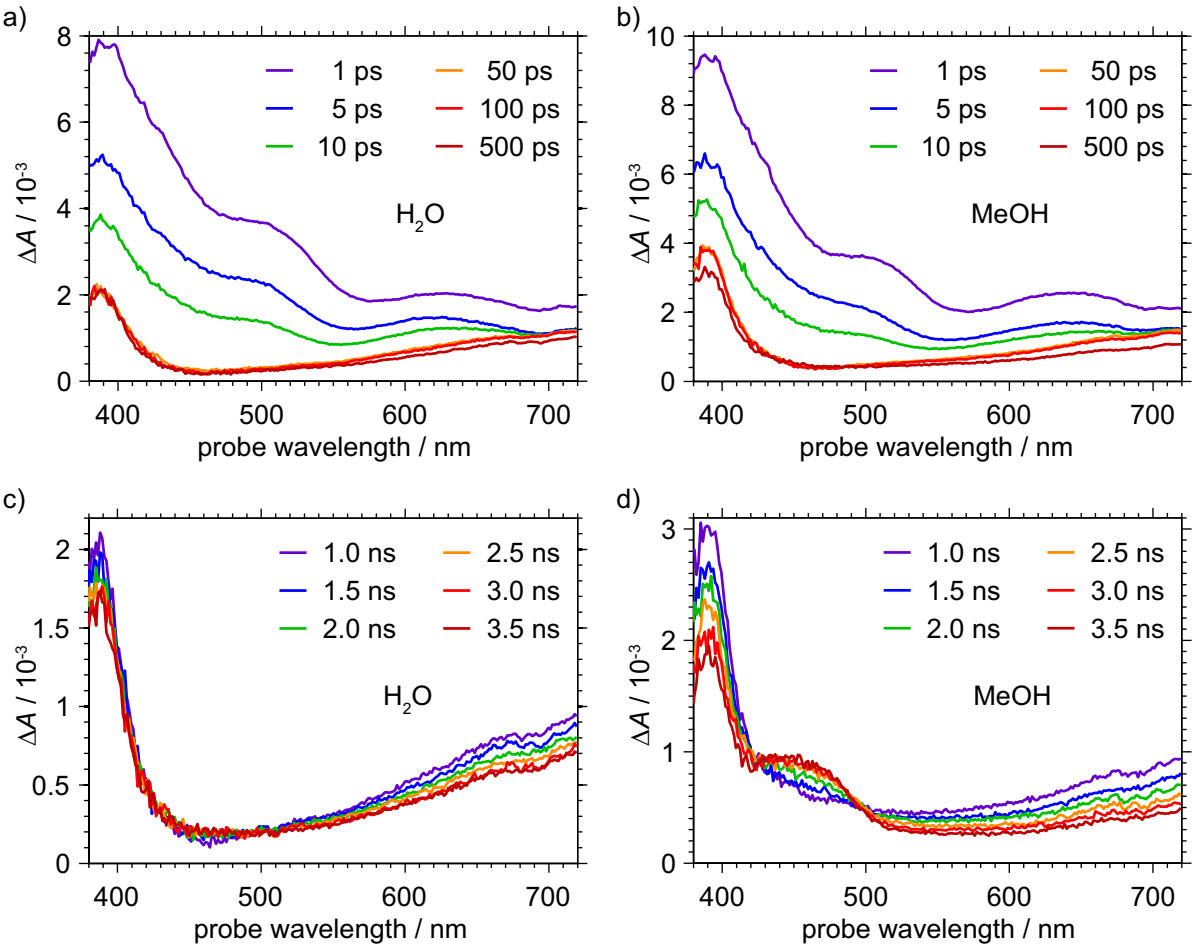

Figure 6.2: Difference spectra for UV excitation of **TTC**. The pump wavelength is centered at 260 nm. For short delay times $\tau \leq 500$ ps almost no difference can be seen between the aqueous (a) and the methanol solution (b). Whereas the change in absorbance ΔA remains almost constant in water for delay times larger than 500 ps (c), a new band rises around 460 nm in the alcoholic solution (d).

tense absorption band with maxima located around 400, 520, and 625 nm is observed, which originates from an intermediate **1** that will be identified below. This signal decays on a 10 ps time scale, subsequently turning into an absorption profile with a maximum at 390 nm and a broad contribution extending beyond 720 nm, which is attributed to an intermediate **2**. Whereas the dynamics are rather independent of the solvent during the first 100 ps, the further reaction of intermediate **2** differs drastically for aqueous and alcoholic solution. In methanol (Fig. 6.2d), an absorption around 460 nm grows in on a nanosecond time scale, which neither matches the steady-state spectra of **PTC** nor of **TPF** and hence is assigned to an intermediate **3**. Note that the absorption of intermediate **3** increases at the expense of **2**, with an isosbestic point close to 500 nm, indicating a sequential process. In water (Fig. 6.2c), the formation of intermediate **3** is much slower, yet already becomes evident within the experimental time window of a few nanoseconds.

For the aqueous as well as the methanolic solution of **TTC**, the resulting lifetimes from a global fit assuming a sequential model are given in Table 6.1. For a sufficient description of

Table 6.1: Lifetimes resulting from a global fit of transient-absorption data of **TTC** in water and methanol for a pump wavelength of 260 nm assuming a sequential model.

solvent	τ_1 / ps	τ_2 / ps	τ_3 / ns	τ_4 / µs
H_2O	1.0	9.3	6.3	-
MeOH	0.44	7.1	2.0	1.0

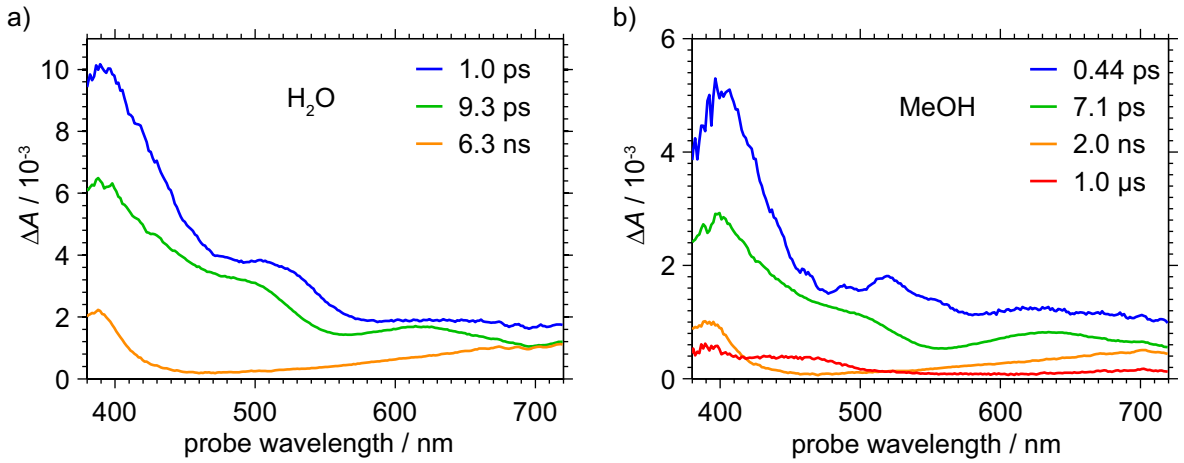

Figure 6.3: Evolution-associated difference spectra (EADS) of **TTC**. a) The dynamics in water are described with three lifetimes (corresponding to EADS 1–3). b) In methanol an additional time constant (corresponding to EADS 4) representing the rise of the absorption band around 460 nm assigned to intermediate **3** is needed to sufficiently describe the data in the global fit.

the dynamics in aqueous solution three lifetimes are needed. In contrast, for the solution of **TTC** in methanol, four lifetimes are needed for an adequate fitting result whereas the lifetime τ_4 was fixed to 1 µs. The amplitudes corresponding to the lifetimes of the global fit (EADS) are shown in Fig. 6.3a,b for aqueous and methanol solutions.

To further investigate the solvent dependence of these intermediates, transient difference spectra of **TTC** in various alcohols R-OH were measured (R = methyl, Me; ethyl, Et; *i*-propyl, *i*-Pr; and *i*-butyl, *i*-Bu). To avoid differences which just arise from slightly different solute concentration in the respective solvent, transient difference spectra were normalized by a factor corresponding to the integrated difference spectrum at τ = 100 ps for each respective solvent (Fig. A.2). For all measured solvents the difference spectra up to about 500 ps look very similar (see Fig. 6.4a for τ = 100 ps, for a series of delay times see Appendix A.2, Fig. A.2). Hence, the dynamics associated with the formation of intermediates **1** and **2** are not very sensitive to the solvent. By contrast, the reaction towards intermediate **3** (see Fig. 6.4b for τ = 3 ns) becomes faster for the larger alcohols.

These measurements provide insight into how and at what time scale the cyclic tetrazolinyl radical **TTC**$^{\bullet}$ is formed. The time constants as well as the solvent dependence of the observed dynamics, together with spectral characteristics allow an identification of the underlying photoreaction which proceeds in a sequential manner. Electron transfer from solvent to solute requires solvent rearrangement which cannot proceed instantly [265], so that due to the femtosecond time resolution a radical formation right after excitation can be excluded.

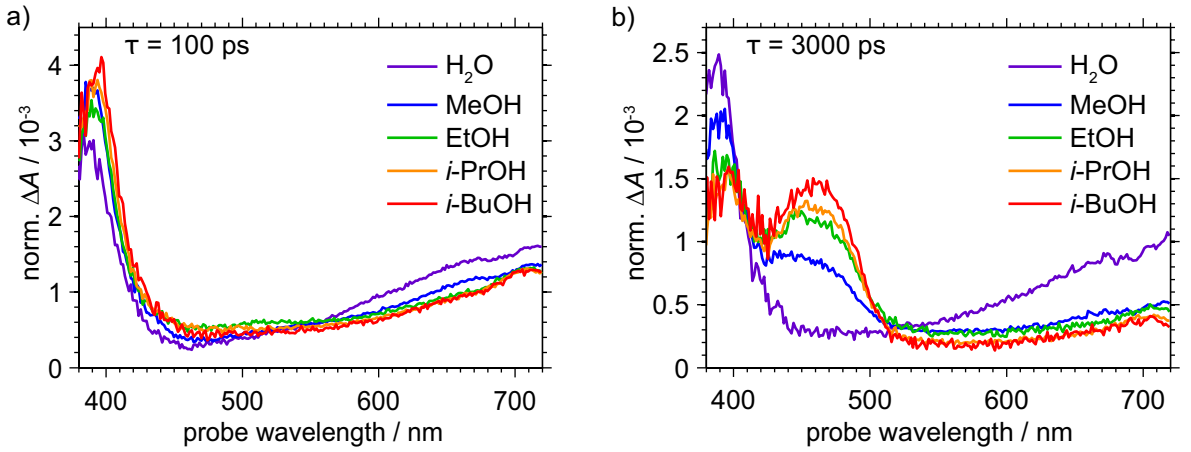

Figure 6.4: Normalized difference spectra of **TTC** in water and various alcohols. a) The normalized difference spectra for a delay time of $\tau = 100$ ps look rather similar for water and all alcohols employed in this study. b) For a delay time of $\tau = 3000$ ps, the formation of the absorption band of intermediate **3** is stronger the larger the alcohol is.

In the following, the origin and structure of the observed intermediate species are discussed. Since eventually species **PTC** is formed, an ultrafast electrocyclization similar to the dihydrophenanthrene formation in the photochemistry of *cis*-stilbene [266,267] might occur. Such a mechanism was already excluded earlier due to an unfavorable charge distribution in the dihydro product (2-phenyl-8a,8b-dihydrobenzo[*c*]tetrazolo[2,3-*a*]cinnoline-4,13-diium-1-ide) of **TTC** [268]. After excitation, the tetrazolium ring can open up on an ultrafast time scale, similar to 1*H*-benzotriazole for which the ring opens within 2 ps in aqueous solution [269]. Quantum-chemical calculations of the LUMO of **TTC** [270] support the possibility of a ring-opening at the same position as necessary for the formation of **TPF**, because of zero electron density right at the center of this bond. This bond also exhibits the lowest ground-state bond order in the tetrazolium ring [271]. If the ring is opened, the conjugation is interrupted by going from the initially aromatic **TTC** to ro-**TTC** (Scheme 6.2), so that the absorption characteristics will drastically change. The absorption around 520 nm observed for intermediate **1** resembles the absorption of a tetraaza pentadienium cation [272] for which the N-N=C-N=N$^+$ backbone is identical to ro-**TTC**. Therefore, it is concluded that upon photoexcitation, **TTC** will open the central ring and turn into ro-**TTC**.

The absorption of intermediate **1** (i.e., ro-**TTC**) diminishes with a decay constant that is found to be $\tau_2 = 9.3$ ps in water and 7.1 ps in methanolic solution. For the other alcohols employed in this study, the decay is on a similar time scale (Fig. A.2, see subfigures for 1 and 10 ps). Species ro-**TTC** turns into intermediate **2** which is formed within tens of picoseconds but reacts on within a nanosecond time scale. Tetrazolium salts are known to be excellent electron acceptors, while typical rates for electron transfer from the solvent are in the picosecond regime [265], suggesting that intermediate **2** is the result of an electron uptake to form ro-**TTC**$^\bullet$ (Scheme 6.2). This assignment is corroborated by the shape of the corresponding transient-absorption signal which matches the absorption of the triphenylverdazyl radical [273, 274]. The latter compound is an open-shell 7π-electron system in which an additional carbon atom compared to **TTC** is included to form a six-membered ring, caus-

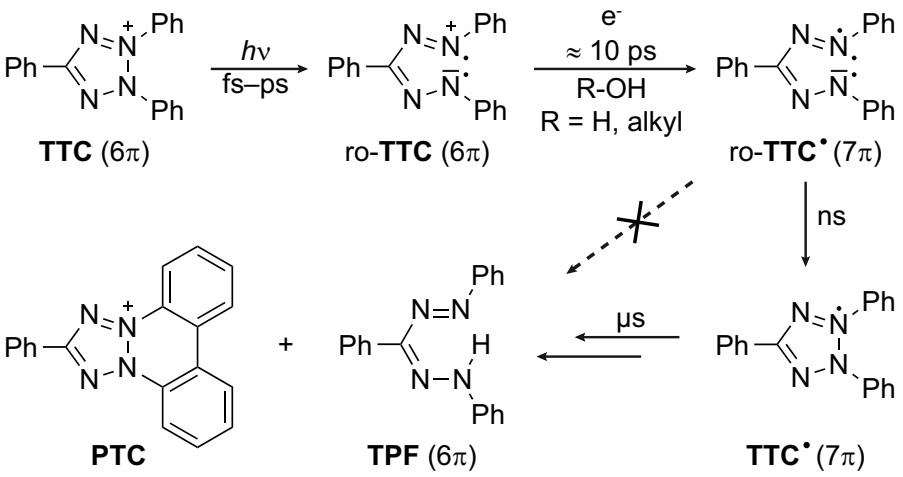

Scheme 6.2: The photochemical reaction pathway of **TTC** as identified in this study, together with the molecular structures of the products **TPF**, **PTC**, as well as the intermediates ro-**TTC**, ro-**TTC**•, and **TTC**•. The number of π electrons in the central entity is indicated.

ing a non-planar and non-aromatic NNCNN sequence with a delocalized unpaired electron, as also present in ro-**TTC**•. Several studies have pointed out the close relation of these radicals [260, 272, 275, 276]. Hence, intermediate **2** is assigned to the tetraaza pentenyl radical ro-**TTC**•.

Cyclic radicals containing four nitrogen atoms are much more stable than the linear analogues [275]. Furthermore, ESR studies identified the cyclic tetrazolinyl radical **TTC**• to be formed upon photoexcitation of tetrazolium salts [259, 260]. The radical ro-**TTC**• therefore closes the ring, forming the cyclic **TTC**•. Direct evidence is found that this indeed is the case. Intermediate **2** (i.e., ro-**TTC**•) with its broad absorption turns into intermediate **3** which exhibits a rather sharp absorption at 460 nm. Both the spectral position and width are in agreement with the characteristic signal of the tetrazolinyl radical **TTC**•, as identified in flash-photolysis studies of the slow dynamics of the TTC photoreaction [257]. Pulse radiolysis studies of **TTC** [264] and electrochemical studies of ditetrazolium salts [263] substantiate the assignment by absorption signatures of tetrazolinyl radicals that are similar to the transient difference spectra of **TTC** in alcohols for nanosecond delay times in Fig. 6.4b. Therefore, in ro-**TTC**• the ring closes to form **TTC**•, with the rise of intermediate **3** directly revealing the formation rate of the cyclic **TTC**•.

To determine the decay of the ro-**TTC**• intermediate, the change in absorbance was fitted with a single exponential decay function for individual probe wavelengths,

$$\Delta A = a_{\text{decay}} \times \exp\left[-k_{\text{ind}}(\tau - t_{0,\text{decay}})\right], \tag{6.1}$$

with a decay rate k_{ind}, the amplitude a_{decay} and the time-zero point $t_{0,\text{decay}}$ (only included in cases where slight misalignments in between experiments cause a shift of temporal overlap, which however is negligible as confirmed by the fit results, Table 6.2).

At a delay time of 100 ps no signal from the ro-**TTC** cation is observed anymore, but only the absorption of intermediate **2** (i.e., ro-**TTC**•), and the product formation of **TTC**• is still not visible. Hence, the fit was restricted to data points associated with delay times $\tau \geq 100$ ps.

Table 6.2: Averaged fitting parameters from Eqs. (6.1) and (6.2) for a wavelength range between 570 and 719 nm (a_{decay}, k, k^{-1}, $\lg(k/\mathrm{ps}^{-1})$, and $t_{0,\mathrm{decay}}$) and for the whole probe wavelength range (t_0), respectively.

solvent	a_{decay} / 10^{-3}	k / $10^{-4}\,\mathrm{ps}^{-1}$	k^{-1} / ns	$\lg(k/\mathrm{ps}^{-1})$	$t_{0,\mathrm{decay}}$ / 10^{-5} ps	t_0 / 10^{-4} ps
H_2O	1.17	1.65	6.06	-3.78	2.38	-4.16
MeOH	0.969	3.30	3.03	-3.48	-5.04	-6.57
EtOH	0.940	3.39	2.95	-3.47	-6.15	-7.75
i-PrOH	0.905	4.07	2.46	-3.39	-7.52	-9.10
i-BuOH	0.886	4.14	2.42	-3.38	-8.22	-6.29

As the transient difference spectra do not show any contributions from **TTC•** at wavelengths above 570 nm, the fit was also restricted to wavelengths between 570 and 719 nm. Figure 6.5a shows the rates k_{ind} of the fit for water and the alcohols in the selected probe-wavelength range. The averaged decay rates k are indicated with horizontal lines and are given in Table 6.2.

After fitting the rate for the reduction, the complete probe-wavelength range for delay times larger than 100 ps was fitted with a function describing the sum of the concentrations of two sequential intermediates with the averaged rate k obtained from Eq. (6.1) in the previous step,

$$\Delta A = a \times \exp[-k(\tau - t_0)] + b \times \{1 - \exp[-k(\tau - t_0)]\}. \tag{6.2}$$

This cyclization reaction is strongly solvent-dependent. As is evident from Fig. 6.4b, **TTC•** appears faster in the larger alcohols. To quantify the stabilizing influence of the solvent on the linear ro-**TTC•**, an empirical polarity scale of the solvent can be an appropriate measure [277].

The first-order rate k for cyclization of ro-**TTC•** to the tetrazolinyl radical **TTC•** has been obtained in a variety of solvents. To determine which solvent property is responsible for the observed rates, correlations between the logarithm of the rate and characteristic parameters of the solvent are investigated. Besides the gas-phase ionization potential IE of each solvent molecule, the solvent's viscosity η, autoprotolysis constant $\mathrm{p}K_{\mathrm{auto}}$, and several empirical polarity parameters are considered (see Table A.1). For the empirical polarity scales, the solvatochromic parameters of Kamlet and Taft, α, β, and π^*, describing hydrogen bond donating (α) and accepting (β) ability and solvent dipolarity/polarizability (π^*), respectively [278] were chosen. Furthermore, the $E_{\mathrm{T}}(30)$ scale of Dimroth and Reichardt [277], as well as the Kosower Z-value, which are measures for the ionizing power [279] or solvent polarity are considered. The data is not compared to further scales, like the Kagiya $\Delta\nu_D$ value which is a measure of electron-donating power [280] of a solvent, both because these empirical polarity scales are closely related [277, 280, 281] and since for some of them no number was available in the literature for the larger alcohols.

Correlating the logarithm of the first-order rate k for going from intermediate **2** to **3** (i.e., from ro-**TTC•** to **TTC•**) to the Kamlet–Taft parameter π^* describing solvent dipolarity/polarizability [278] confirms that a more polar solvent slows down the cyclization compared to a less polar one (Fig. 6.5b). The error bars correspond to the standard deviation σ of k. It also becomes evident from Fig. A.4 that the rate of cyclization of the tetrazolinyl radical is governed by the solvent polarity, which is expressed in the good correlation with the different

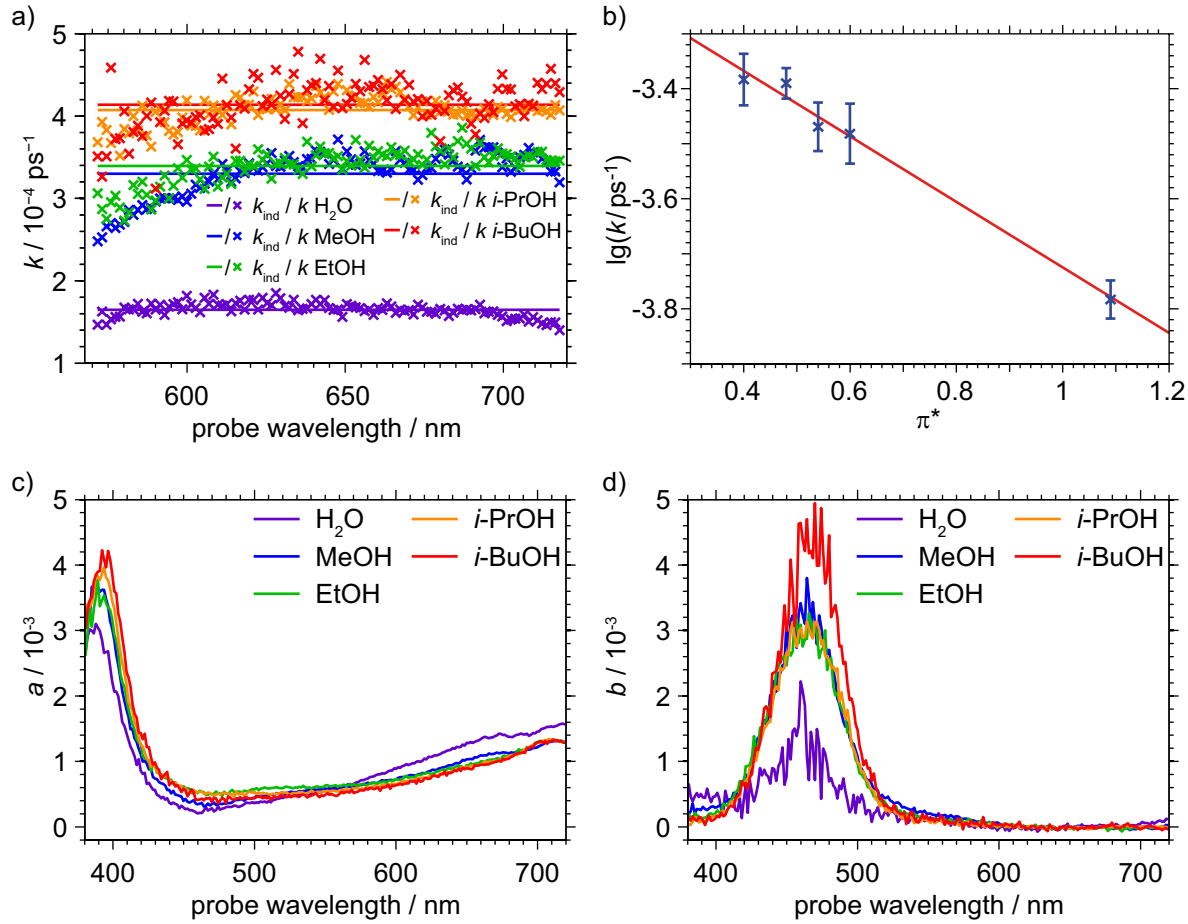

Figure 6.5: Results for the fits according to Eqs. (6.1) and (6.2). a) The rate k_{ind} for the fit of the data with Eq. (6.1) applied to the data subset with 100 ps $\leq \tau \leq$ 3.5 ns and 570 nm $\leq \lambda \leq$ 719 nm. b) The logarithm of the first-order rate k plotted against the solvent parameter π^* (Table A.1). The amplitudes a (panel c) and b (panel d) from a fit according to Eq. (6.2) in water and all investigated alcoholic solutions (for delay times $\tau \geq$ 100 ps).

solvent polarity scales π^* (Fig. 6.5b), $E_{\mathrm{T}}(30)$ (Fig. A.4b), and Z (Fig. A.4c). Plots against viscosity and further empirical solvent polarity parameters result in more pronounced deviations from a linear behavior (see Fig. A.4).

The amplitudes a and b for the decay of ro-**TTC**$^\bullet$ and the rise of the cyclic **TTC**$^\bullet$ radical are shown in Fig. 6.5c,d. Whereas the amplitude a, representing the decay, strongly resembles the difference spectra at 100 ps for all solvents, the amplitude b shows only contributions around 460 nm where the tetrazolinyl-radical band rises on the nanosecond time scale. The amplitude b for the rise of **TTC**$^\bullet$ is largest for the solution in *i*-butanol, similar for the other alcohols, and smallest for water. While from the raw data, the formation of **TTC**$^\bullet$ is least evident for water due to the smallest rate, the formation of **TTC**$^\bullet$ can be nicely deduced from the decomposition of the fit into amplitudes a and b.

A number of tests were performed to validate the assignment of the transient intermediates. DCM shows a small relative permittivity and is often used as solvent for electrochemical reductions and oxidations [282], hence, for **TTC** dissolved in DCM, no electron transfer is ex-

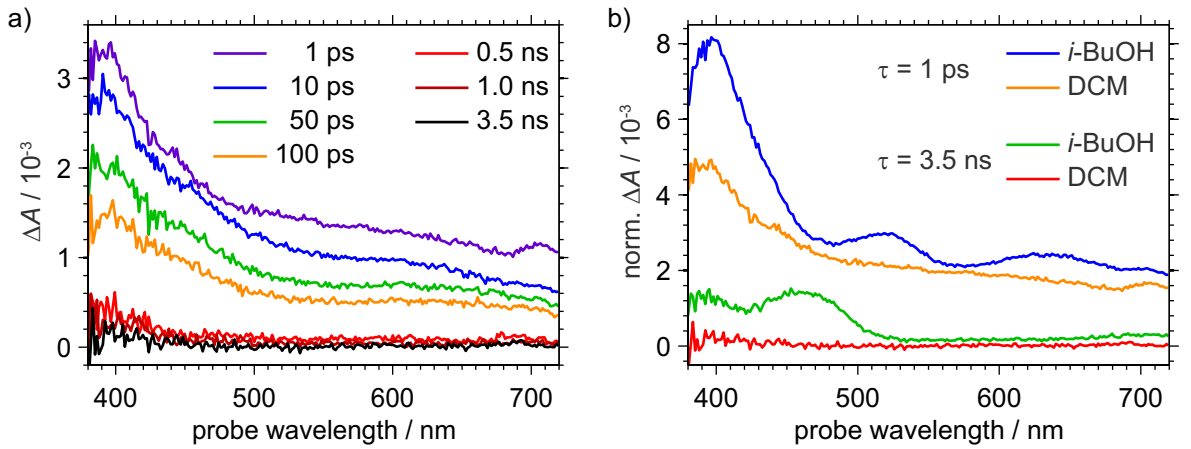

Figure 6.6: Transient difference spectra for **TTC** upon 260 nm excitation. a) Data in DCM for delay times from 1 ps to 3.5 ns. b) In contrast to the alcoholic solutions, the comparison of the normalized spectra in DCM and in *i*-BuOH for the two time delays 1 ps and 3.5 ns shows that no formation of radicals can be observed in DCM. The difference spectra were normalized to the integrated difference spectrum at a delay time of 100 ps. Note that the lifetime of ring-open ro-**TTC** is larger compared to alcohols and water, where it vanishes due to the electron uptake and the formation of the ro-**TTC**$^{\bullet}$ radical.

pected. The difference spectra of **TTC** in DCM for time delays from 1 ps to 3.5 ns, (Fig. 6.6a) substantiate this, because neither intermediates **2** nor **3** (assigned to radical species) are observed, but rather only a broad absorption of intermediate **1** is found. In the aprotic solvent DCM, the absorption assigned to the ring-open cation ro-**TTC** is observed, although without the three pronounced maxima in aqueous and alcoholic solutions. This absorption then decays and no other intermediate is observed, indicating that no radical is formed. After several nanoseconds, no transient absorption is detected anymore, showing that the molecules have relaxed back to the **TTC** ground state instead of forming radicals. Figure 6.6b compares the normalized data for delay times of 1 ps and 3.5 ns in the two solvents DCM and *i*-butanol.

In the following, the results in aqueous solution are discussed and the differences in product formation for different solvents are elucidated. In pure water, both **TPF** and **PTC** are found as final photoproducts, whereas in alcohols only the latter is formed [254]. It has been shown above that the rate of **TTC**$^{\bullet}$ formation is much smaller in water compared to alcohols. Therefore, the differing photoproduct distribution might originate from a competition between cyclization of ro-**TTC**$^{\bullet}$ to **TTC**$^{\bullet}$ and protonation of ro-**TTC**$^{\bullet}$ eventually leading to **TPF**. To test this hypothesis, experiments in phosphate-buffered aqueous solution at acidic pH value were performed (Fig. 6.7). No significant differences can be observed neither in the dynamics nor in the signal contributions compared to aqueous solution for picosecond (Fig. 6.7a) up to nanosecond (Fig. 6.7b) delay times. For the picosecond delay times, the transient difference spectra exhibit the three maxima around 400, 520, and 625 nm, as found in all aqueous and alcoholic solvents used in this study, but not in DCM (Fig. 6.6). After 100 ps, the difference spectrum corresponds to the ro-**TTC**$^{\bullet}$ radical. For nanosecond delay times, the absorption of the tetrazolinyl radical **TTC**$^{\bullet}$ at 460 nm is hardly visible, which grows at the expense of the broad absorption of the first intermediate. The behavior is in accordance with the dynamics

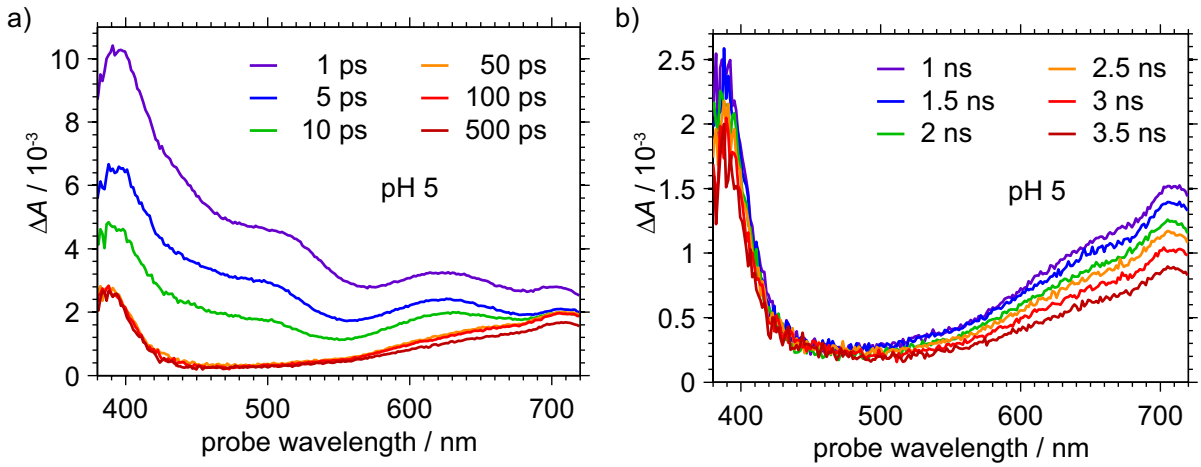

Figure 6.7: Transient difference spectra of **TTC** in acidic solution at pH 5. The graph shows the transient difference spectra of **TTC** for picosecond (a) and nanosecond (b) delay times.

at pH 7, suggesting that the higher proton concentration does not affect the ultrafast dynamics up to the **TTC**• formation.

It should be mentioned that in basic solution it is known that already in the absence of light tetrazolium salts can lead to the formation of the formazan **TPF** [246] and that it can react with hydroxide anions to yield hydroxy-tetrazole and hydroxy-formazan compounds [248]. Therefore, it was further investigated if the observed transient absorption spectra contain any contribution originating from the photodynamics of **TPF**. Further experiments investigating the ultrafast photodynamics of the final photoproduct **TPF** in solution (Appendix A.2, Fig. A.3) prove that no spectral signature of **TPF** is contained in the time-resolved absorption data obtained with **TTC** as reactant, confirming that the signals labeled intermediates **1** to **3** solely originate from transient species formed upon the photoexcitation of **TTC**.

Further supported by the presence of an isosbestic point in Fig. 6.2c which indicates that no bifurcation in the reaction mechanism occurs, it can be concluded that protonation does not play a role on the time scale of **TTC**• formation. Hence, the results substantiate earlier studies which suggested that **TTC**• can undergo a bimolecular reaction involving an additional **TTC** cation on a much longer time scale [257]. Bimolecular disproportionation steps have also been evidenced in the electrochemical formation of the formazan anion **TPF**$^-$ from **TTC**• [261, 262, 283–285]. Together with these earlier findings, the observation that there is no difference in the photoreaction pathway towards **TTC**• supports the explanation for the photoproduct distribution given by Jámbor [246], namely that both **TPF** and **PTC** are formed in water and alcohols, but **TPF** is photo-oxidized back to **TTC** in alcohols where **TPF** is highly soluble, in contrast to the situation in water. Scheme 6.2 summarizes the ultrafast reaction steps towards the formation of **TTC**• unraveled in this study. No decision on the final photoproducts is made on an ultrafast time scale. Nevertheless, the photoreaction pathway via **TTC**• towards **TPF** may have an impact on the interpretation of tetrazolium assays, since light from fluorescence lamps [286] can be sufficient for initiating a photochemcial rather than an enzymatic reduction of **TTC**.

6.3 Conclusion and Outlook

In summary, for **TTC** the known photochemistry could be confirmed and from ultrafast time-resolved measurements, evidence was presented for the direct observation of the formation of the cyclic tetrazolinyl radical **TTC**$^\bullet$ after photoexcitation of **TTC** in solution. The results allow an assignment of the reaction sequence triggered by photoexcitation of **TTC**. Initially, the central ring is opened yielding intermediate ro-**TTC**, from which the ring-open radical ro-**TTC**$^\bullet$ is formed in about 10 ps in aqueous and alcoholic solution (but not in DCM) via uptake of an electron from the solvent. Subsequently, a cyclization from the much less stable ro-**TTC**$^\bullet$ to the **TTC**$^\bullet$ radical occurs. A series of experiments disclosed that more polar solvents slow down this ring-closure process in the radical compared to less polar ones. The results further show that despite different photoproduct distributions reported for aqueous and alcoholic solutions, the primary photoreaction up to the **TTC**$^\bullet$ formation is the same, supporting the interpretation that the differences originate from a bimolecular disproportionation and back-reaction on much longer time scales.

Future experiments on the light-induced dynamics of **TTC**$^\bullet$ could be facilitated by pump–repump–probe spectroscopy with non-degenerate pump pulses [85–87]. To gain even better insight in the ring-opening reaction the implementation of shorter pump pulses allowing a higher temporal resolution is desirable.

Apart from the photochemistry of tetrazolium salts other than **TTC**, another interesting aspect is the photochemistry of the photoproducts itself. Both aspects will be focussed on in a future publication [7]. Formazans show a strong solvatochromism which is assigned to configurational rearrangements in the formazan skeleton [254, 287, 288]. Since several photo-initiated steps are supposed to be responsible for the rearrangement [289], not only transient-absorption but pump–repump–probe experiments would be beneficial to gain insight into the formazan photochemistry. The strong fluorescence of **PTC** makes it an interesting candidate for time-resolved emission studies. Thus, details of its dynamics not available by transient absorption spectroscopy could be unraveled in future experiments, e.g., by fluorescence up-conversion.

7 Summary

Photoinduced processes are nowadays studied with a huge variety of spectroscopic methods. In the liquid phase, transient absorption spectroscopy is probably the most versatile pump–probe technique used to study light-induced molecular phenomena. Optical time-resolved spectroscopy is established in a large number of laboratories and is still further being developed with respect to many technical aspects. Nevertheless, the full potential of shortening the data-acquisition time—necessary for the investigation of rapidly photodegrading samples and observation of macroscopically fast processes—achievable with high-repetition-rate laser systems and shot-to-shot detection was not fully exploited. Especially, shot-to-shot detection is highly beneficial due to the high correlation of subsequent laser pulses.

The development and implementation of 100 kHz broadband shot-to-shot data acquisition was presented in Chapter 3. For an established laser dye as a benchmark system, ultrafast excited-state dynamics were measured for the first time with broadband shot-to-shot detection at 100 kHz. An analysis of both the noise characteristics of the employed laser and the correlation of subsequent pulses quantified the advantage of shot-to-shot data acquisition. In the utilized software environment, the time for measuring a complete data set could be sped up by a factor of three or even higher compared to a laser system working at 1 kHz. So far, the limiting factor is the data processing and the movement of the mechanical delay stage. Nevertheless, the new shot-to-shot detection has the potential to shorten the measurement time up to a factor of 100. The data quality is improved by a factor of three when the hitherto conventional averaging scheme is compared to shot-to-shot acquisition for the same number of laser pulses. The expansion of shot-to-shot data acquisition for high repetition rates will allow studies on sensitive samples as exposure times can strongly be reduced to achieve the same signal-to-noise ratio. In addition, multidimensional spectroscopy can also be extended to high-repetition shot-to-shot readout allowing an efficient recording of data. Therefore, in future experiments, dynamics and couplings in sensitive samples and kinetic processes could be studied in more detail.

Complex photophysical and photochemical phenomena are subject of many fields of research. Many of these multifaceted processes are not yet fully understood. Therefore, a possible approach is the elucidation of single reaction steps with the combination of transient absorption spectroscopy and a suitable, less complex model system. The systematic variation of the model system's properties and environments, e.g., by chemical substitution or adequate choice of the solvent allows the determination of essential entities and reactivities thereof. Proper knowledge of an individual intermediate step and its determining factors can enhance the understanding of the complete photoreaction process.

The application of transient absorption spectroscopy was shown for the optically-induced electron transfer in a series of donor–acceptor oligomers in Chapter 4. In general, the solvent relaxation times were isolated from the back-electron-transfer dynamics by a global lifetime analysis. For the smallest oligomeric structure where complete charge separation is possible, an ultrafast equilibration leads to charge recombination from the configuration showing the lowest barrier for recombination. The back-electron transfer strongly depends on the utilized solvent. Whereas in dichloromethane the back-electron transfer occurs with the maximum rate in the barrierless optimal region, the dynamics in toluene are governed by a Marcus inverted-region effect. The experimentally observed rates were also estimated by theoreti-

cal calculations of the respective barriers. The study did not only successfully unravel charge transfer in the oligomeric systems but also improved the understanding of the electron-transfer properties of larger polymers from an earlier study. Therefore, the combination of length variation and time-resolved spectroscopy is an important step towards the correct prediction of charge-carrier dynamics in macroscopic devices, e.g., for photovoltaics.

The bond dissociation of a carbon-monoxide-releasing molecule in aqueous solution was studied in Chapter 5 as a prototype reaction for the photo-triggered breaking of a bond. It was shown that upon excitation only one carbon-monoxide ligand of the tricarbonyl complex is dissociated. A fraction of the photolyzed molecules restore the intact initial complex by geminate recombination within the temporal resolution of the experiment. However, the recombination could be detected by the hot ground-state infrared absorption of the complex. The detectable dicarbonyl formed upon CO release distributes excess energy from the absorbed photon into low-frequency modes which result in broadened absorption bands like for the recombined tricarbonyl. The free coordination site in the ligand sphere is filled with a solvent water molecule. Despite numerous studies of metal carbonyls studied in alkaneous solutions, the elucidation of the dynamics of a CORM in aqueous solution added another important detail to the photochemistry of this class of compounds. Experiments employing a second ultraviolet pump pulse did not trigger further CO dissociation and hence no formation of a monocarbonyl species; this might either be due to a different release mechanism without a further photochemical step or a strong spectral shift of the dicarbonyl's absorption. Both reasons could explain why degenerate pump–repump–probe spectroscopy is inefficient. However, further experiments with ultraviolet probe pulses could substantiate whether the intermediate dicarbonyl reacts further photochemically or not. Apart from the model-system character of the CORM for bond dissociation, the study could determine exactly how many CO ligands are initially photolyzed off. Detailed knowledge of the release mechanism will affect the previous use and application as well as the further development of CORMs as therapeutic prodrugs to deliver high local concentrations of CO in cancerous or pathological tissue. Hence, the study of two-photon absorption properties which are important for in vivo applications of CORMs should be the main focus in further spectroscopic experiments.

In Chapter 6, both abovementioned molecular phenomena—electron transfer and bond dissociation—were studied in combination. The photochemistry of a tetrazolium salt was studied in detail in a variety of different solvents. Being a relatively small molecule, the studied tetrazolium cation shows a multifaceted photochemistry and is therefore a textbook example for the combination of ultrafast molecular phenomena studied in different environments. Within femtoseconds, the tetrazolium ring is opened. The biradicalic species is then reduced via uptake of an electron from the solvent. The formation of the ring-open formazan photoproduct from this point of the reaction sequence on was excluded by experiments with acidic pH value of the solution. The ring-open radical is stabilized by ring-closure. The resulting tetrazolinyl radical was already observed in experiments with microsecond time resolution. However, its formation was observed in real time for the first time in this study. Irradiation of a tetrazolium-salt solution yields different photoproduct distributions depending on the solvent. However, it was shown that all photoproducts have a tetrazolinyl radical as a common precursor on an ultrafast time scale. In combination with studies from the literature, the complete photochemical conversion of a tetrazolium salt was clarified in this study. Apart from the prototype character of the reaction sequence, the reaction mechanism will have impact on research associated with

life science where tetrazolium assays are used on a daily basis without taking into account of photochemical conversion of the indicating tetrazolium ion and its photochemically formed reactive intermediates. On the basis of the tetrazolium-ion photochemistry, the rich photochemistry of the formazan photoproduct, including structural rearrangements and subsequent reformation of the tetrazolium ion, might be the subject of future studies.

This thesis shows a method advancement and application of transient absorption spectroscopy to exemplary molecular model systems. The insights into each respective field did not only enlighten singular aspects, but have to be seen in a much larger context. Understanding complex photoinduced processes bottom-up by learning about their constituting steps—microscopically and on an ultrafast time scale—is an ideal method to approach understanding and prediction of phenomena in large molecular systems like biological or artificial architectures as for example used in photosynthetic light-harvesting and photovoltaics.

Zusammenfassung

Photoinduzierte Prozesse werden heutzutage mit einer Vielzahl spektroskopischer Methoden untersucht. In der flüssigen Phase ist die transiente Absorptionsspektroskopie die wohl vielfältigst verwendete Anrege-Abfrage-Technik um lichtinduzierte molekulare Phänomene zu untersuchen. In vielen Forschungsgruppen ist die zeitaufgelöste optische Spektroskopie eine etablierte Methode und wird bezüglich vieler technischer Aspekte weiterentwickelt. Dennoch ist das volle Potential der für die Untersuchung photoempfindlicher Proben und die Beobachtung schneller makroskopischer Prozesse notwendigen Verkürzung der Datenaufnahmezeit, erreichbar mit hohen Laserwiederholraten und Schuss-zu-Schuss-Detektion, noch nicht vollständig ausgeschöpft worden. Die Schuss-zu-Schuss-Detektion ist insbesondere aufgrund der hohen Korrelation aufeinanderfolgender Laserpulse vorteilhaft.

Die Entwicklung und technische Umsetzung der breitbandigen Schuss-zu-Schuss-Datenaufnahme mit 100 kHz wurde in Kapitel 3 vorgestellt. An einem bekannten Laserfarbstoff als Referenzsystem wurden zum ersten Mal Dynamiken des angeregten Zustands mit breitbandiger Schuss-zu-Schuss-Detektion mit 100 kHz gemessen. Durch eine Analyse sowohl der Rauschcharakteristika des verwendeten Lasersystems als auch der Korrelation aufeinanderfolgender Pulse konnten die Vorzüge der Schuss-zu-Schuss-Datenaufnahme quantitativ bestimmt werden. In der verwendeten Softwareumgebung konnte die Messzeit, verglichen mit einem Lasersystem mit einer Wiederholrate von 1 kHz, um mindestens einen Faktor drei beschleunigt werden. Zum jetzigen Zeitpunkt sind die Datenverarbeitung und das Verfahren des mechanischen Lineartisches zur Zeitverzögerung die limitierenden Faktoren der Messzeitverkürzung. Dennoch hat die neue Schuss-zu-Schuss-Detektion das Potential die Messzeit um einen Faktor bis zu 100 zu verkürzen. Die Datenqualität wurde um einen Faktor drei verbessert, wenn das bisher verwendete konventionelle Mittelungsverfahren mit der Schuss-zu-Schuss-Aufnahme für die gleiche Anzahl an Laserpulsen verglichen wird. Die Ausweitung der Schuss-zu-Schuss-Datenaufnahme für hohe Wiederholraten wird die Untersuchung empfindlicher Proben erlauben, da die Belichtungszeit zur Erreichung desselben Signal-zu-Rausch-Verhältnisses stark reduziert werden kann. Des Weiteren kann das Schuss-zu-Schuss-Auslesen auf die multidimensionale Spektroskopie ausgeweitet werden, was auch hier eine effiziente Datenaufnahme erlaubt. Aufgrund dessen werden in künftigen Experimenten Dynamiken und Kopplungen in empfindlichen Proben und kinetischen Prozessen genauer untersucht werden können.

Komplexe photophysikalische und photochemische Phänomene sind Gegenstand vieler Forschungsgebiete. Etliche dieser vielschichtigen Prozesse sind noch nicht gänzlich verstanden. Eine mögliche Herangehensweise an dieses Problem ist die Aufklärung einzelner Reaktionsschritte mittels der Kombination von transienter Absorptionsspektroskopie mit geeigneten, weniger komplexen Modellsystemen. Die systematische Änderung der Eigenschaften und Umgebungen der Modellsysteme, beispielsweise durch chemische Substitution oder die Wahl eines geeigneten Lösungsmittels, erlaubt die Bestimmung wesentlicher Bestandteile und deren Reaktivitäten. Fundierte Kenntnis einzelner Zwischenschritte und deren bestimmende Faktoren können das Verständnis des lichtinduzierten Gesamtprozesses verbessern.

Die Anwendung der transienten Absorptionsspektroskopie auf den optisch-induzierten Elektronentransfer in einer Reihe von Donor-Akzeptor-Oligomeren wurde in Kapitel 4 gezeigt. Durch globale Datenanalyse wurden die Relaxationszeiten des Lösungsmittels von den Raten des Elektronenrücktransfers getrennt. In der kleinsten oligomeren Struktur welche eine

vollständige Ladungstrennung erlaubt, führt eine ultraschnelle Gleichgewichtseinstellung zur Ladungsrekombination in der Konfiguration mit der kleinsten Rekombinationsbarriere. Der Elektronenrücktransfer hängt stark vom verwendeten Lösungsmittel ab. Während der Elektronenrücktransfer in Dichlormethan mit der maximalen Rate in der optimalen Region ohne Barriere stattfindet, ist die Dynamik in Toluol vom Effekt der Marcus-invertierten Region bestimmt. Die experimentell beobachteten Raten wurden durch theoretische Berechnung der jeweiligen Barrieren abgeschätzt. Diese Arbeit hat nicht nur erfolgreich den Ladungstransfer in den oligomeren System entschlüsselt, sondern auch das Verständnis der Elektronentransfereigenschaften größerer Polymere aus vorherigen Studien erweitert. Aus diesem Grund ist die Kombination der Längenvariation mit der zeitaufgelösten Spektroskopie ein wichtiger Schritt in Richtung der korrekten Vorhersage von Ladungsträgerdynamiken in makroskopischen Bauteilen, wie sie beispielsweise in der Photovoltaik verwendet werden.

Die Bindungsdissoziation eines Kohlenmonoxid-freisetzenden Moleküls (CORM) in wässriger Lösung wurde in Kapitel 5 als prototypische Reaktion für die lichtinduzierte Spaltung einer Bindung untersucht. Es konnte gezeigt werden, dass nach Anregung nur ein Kohlenmonoxid-Ligand des Tricarbonyl-Komplexes abgespalten wird. Ein Teil der photolysierten Moleküle stellt den intakten Anfangskomplex durch paarweise Rekombination innerhalb der Zeitauflösung des Experiments wieder her. Dennoch konnte die paarweise Rekombination durch die Grundzustandsabsorption des schwingungsangeregten Komplexes im Infraroten detektiert werden. Das nach CO-Freisetzung beobachtete Dicarbonyl verteilt die Überschussenergie des absorbierten Photons auf Schwingungsmoden niedriger Frequenz, was zum Auftreten verbreiterter Absorptionsbanden führt. Die freie Koordinationsstelle in der Ligandensphäre wird mit einem Wassermolekül aufgefüllt. Trotz zahlreicher Studien zu Metallcarbonylen in alkanischen Lösungsmitteln fügt die Aufklärung der Dynamiken des CORMs in wässriger Lösung ein wichtiges Detail der Photochemie dieser Verbindungsklasse hinzu. Experimente mit einem zweiten ultravioletten Anregepuls lösten keine weitere CO-Freisetzung und somit keine Bildung einer Monocarbonyl-Spezies aus. Der Grund hierfür mag entweder ein anderer Freisetzungsmechanismus ohne weiteren photochemischen Schritt oder eine große spektrale Verschiebung der Absorption des Dicarbonyls sein. Beide Gründe erklären, warum die Anrege-Wiederanrege-Abfrage-Spektroskopie keinen Effekt zeigt. Jedoch könnten weitere Experimente mit ultravioletten Abfragepulsen ergründen, ob das Dicarbonylintermediat photochemisch weiterreagiert oder nicht. Abgesehen vom Modellsystem-Charakter des CORMs für die Bindungsdissoziation konnte diese Untersuchung bestimmen, wie viele CO-Liganden ursprünglich freigesetzt werden. Die genaue Kenntnis des Freisetzungsmechanismus wird die bisherige Benutzung und Anwendung, sowie die zukünftige Entwicklung der CORMs als therapeutische Vorstufe zur Verabreichung hoher lokaler Konzentrationen an CO in karzinogenem und pathologischem Gewebe beeinflussen. Daher sollte die Untersuchung der Zweiphotonenabsorptionseigenschaften, welche für die in vivo Anwendung von CORMs eine wichtige Rolle spielen, in zukünftigen spektroskopischen Experimenten in den Vordergrund rücken.

In Kapitel 6 wurde eine Kombination aus beiden oben erwähnten molekularen Phänomenen, Elektronentransfer und Bindungsspaltung, untersucht. Die Photochemie eines Tetrazoliumsalzes wurde detailliert in einer Auswahl unterschiedlicher Lösungsmittel untersucht. Als relativ kleines Molekül zeigt das untersuchte Tetrazoliumkation eine vielfältige Photochemie und ist daher ein Paradebeispiel für die Untersuchung kombinierter ultraschneller Phänomene in unterschiedlichen Umgebungen. Innerhalb von Femtosekunden wird der Tetrazoliumring

geöffnet. Die biradikalische Spezies wird dann durch Elektronenaufnahme aus dem Lösungsmittel reduziert. Die Bildung des ringoffenen Formazan-Photoprodukts an dieser Stelle der Reaktionssequenz wurde durch Experimente in saurer Lösung ausgeschlossen. Das ringoffene Radikal wird durch einen Ringschluss stabilisiert. Das daraus entstehende Tetrazolinyl-Radikal wurde bereits in Experimenten mit Mikrosekundenzeitauflösung beobachtet. Die Bildung in Echtzeit wurde jedoch in dieser Arbeit zum ersten Mal beobachtet. Die Beleuchtung einer Tetrazoliumsalzlösung führt in Abhängigkeit des Lösungsmittels zu unterschiedlichen Photoproduktverteilungen. Auf einer ultraschnellen Zeitskala haben indessen alle Photoprodukte das Tetrazolinyl-Radikal als gemeinsame Vorstufe. In Verbindung mit literaturbekannten Studien wurde in dieser Arbeit die gesamte photochemische Umsetzung eines Tetrazoliumsalzes aufgeklärt. Abgesehen von dem prototypischen Charakter der Reaktionssequenz wird der entschlüsselte Reaktionsmechanismus Einfluss auf die Forschung in den Lebenswissenschaften haben, in welchen Tetrazoliumsalz-basierte Prüfverfahren täglich zur Anwendung kommen, wobei bislang die photochemische Umsetzung und die photochemisch gebildeten reaktiven Intermediate außer Acht gelassen werden. Auf Grundlage der Photochemie des Tetrazoliumions kann die vielschichtige Photochemie des Formazan-Photoprodukts, welche Umlagerungen und erneute Bildung des Tetrazoliumions beinhaltet, Gegenstand zukünftiger Untersuchungen sein.

Diese Arbeit stellt die Methodenverbesserung und Anwendung der transienten Absorptionsspektroskopie auf beispielhafte Modellsysteme vor. Die Einblicke in die jeweiligen Forschungsgebiete beleuchteten nicht nur einzelne Aspekte, sondern müssen in einem wesentlich größeren Zusammenhang gesehen werden. In großen molekularen Systemen wie biologischen oder künstlichen Architekturen, welche beispielsweise in photosynthetischen Lichtsammelkomplexen und der Photovoltaik Anwendung finden, kann man sich dem grundsätzlichen Verständnis komplexer photoinduzierter Vorgänge und deren Vorhersage durch Untersuchung der zugrundeliegenden Teilschritte – mikroskopisch und auf ultraschnellen Zeitskalen – annähern.

Appendix

A.1 Synchronization for 100 kHz Shot-to-Shot Detection

Figure A.1 shows the connectivity diagram of the "Synchronization" electronics from Fig. 3.2 used to synchronize chopper, laser, and CCD acquisition.

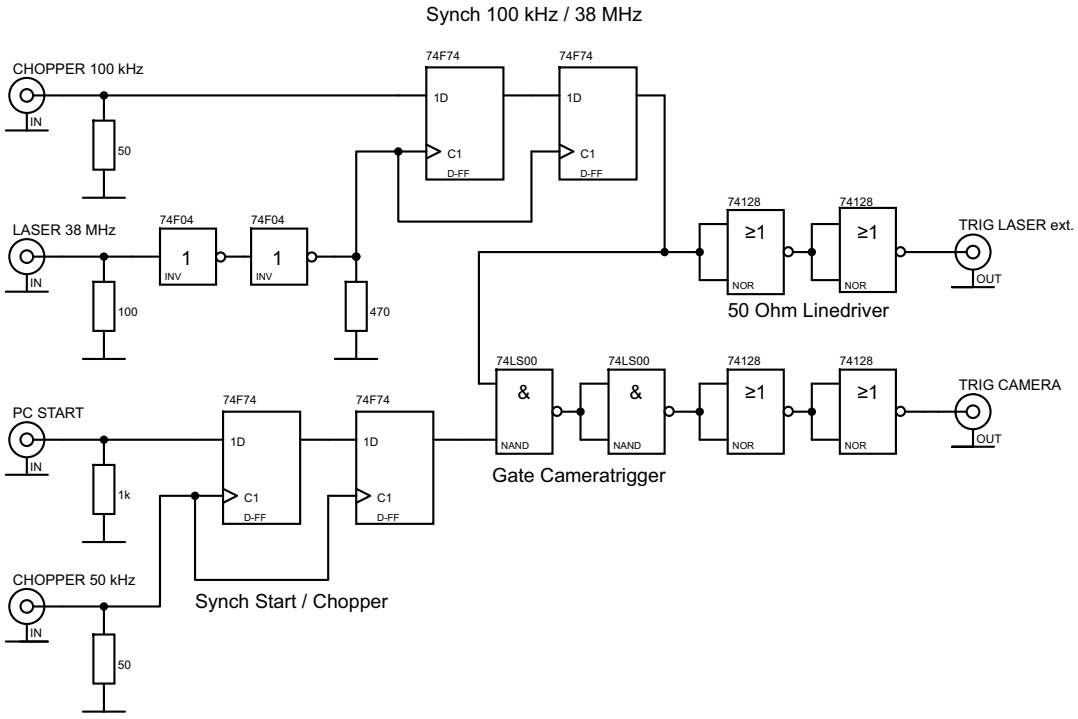

Figure A.1: Connectivity diagram of the synchronization electronics. Reprinted from Ref. [4] with permission from the Optical Society of America. Copyright (2014) Optical Society of America.

A.2 Transient Absorption Spectra of TTC and TPF and Data Fitting Results of TTC

Figure A.2 allows a direct visual comparison of the photodynamics of **TTC** in water and various alcohols. To avoid differences from slightly different solute concentrations, the difference spectra were normalized by a factor corresponding to the integrated change in absorbance at $\tau = 100\,\text{ps}$ for each respective solvent.

The steady-state absorption spectra of the **TTC** samples already show that no **TPF** is contained initially. Since it is however formed during the run of a transient-absorption experiment, although in extremely small concentrations compared to the reservoir solution pumped perpetually through the cuvette, it should be excluded that formazan traces contribute to the observed transient-absorption signals. Hence, transient difference spectra for UV excitation at 296 nm were recorded of **TPF** in methanol for different delay times (Fig. A.3a,b). A ground-state bleaching signal at 490 nm is most prominent, together with an ESA most prominent on

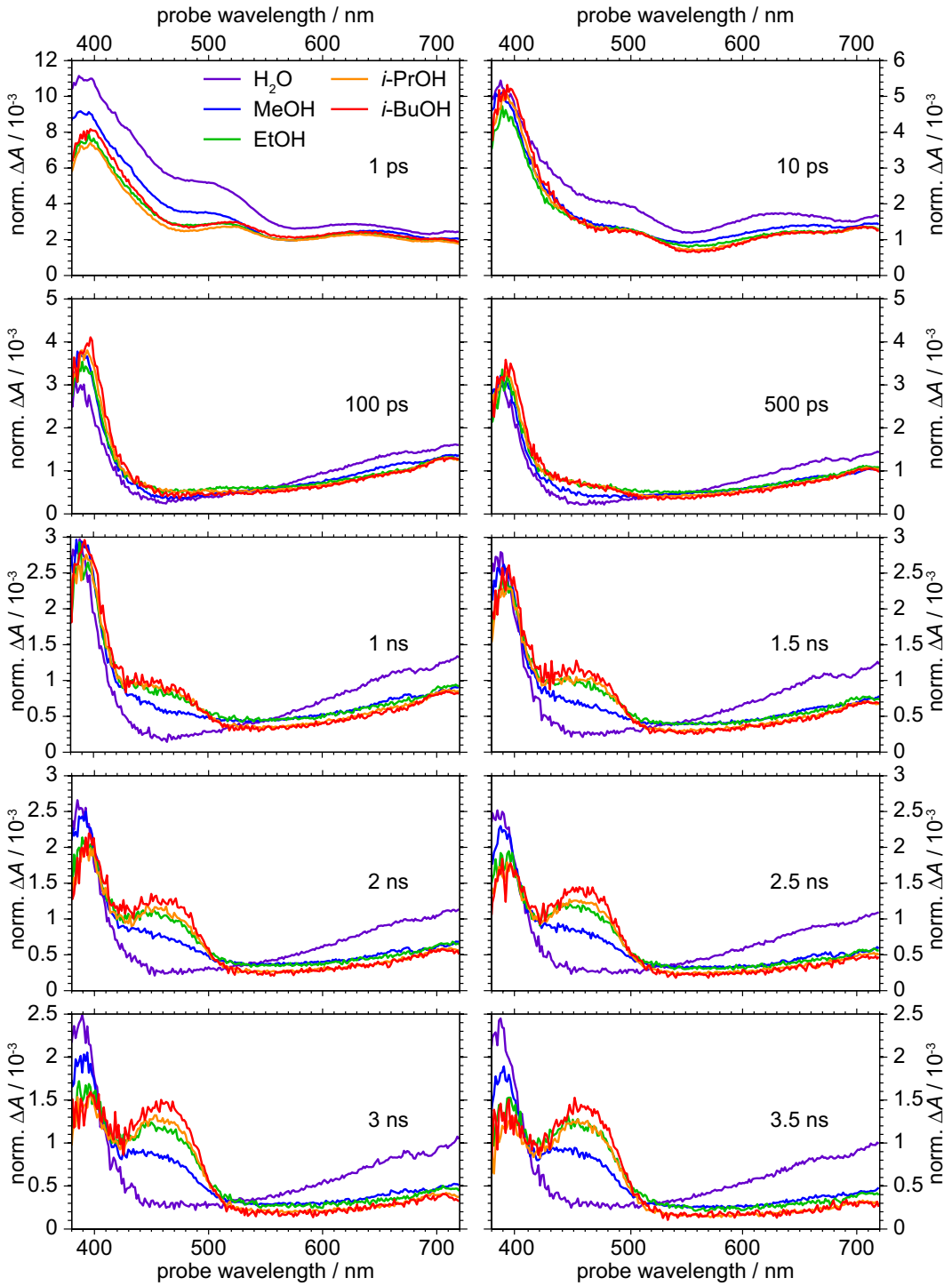

Figure A.2: Transient difference spectra of **TTC** in water and different alcohols. The delay time from 1 ps to 3.5 ns is labeled in each subfigure, the different curves correspond to water (violet), methanol (blue), ethanol (green), *i*-propanol (orange), and *i*-butanol (red).

the long-wavelength side (Fig. A.3a). No further signals appear on a nanosecond time scale Fig. A.3b) in the probed wavelength range, with a remaining ground-state bleaching signal indicating that part of the **TPF** reactant molecules have undergone a photoreaction, possibly

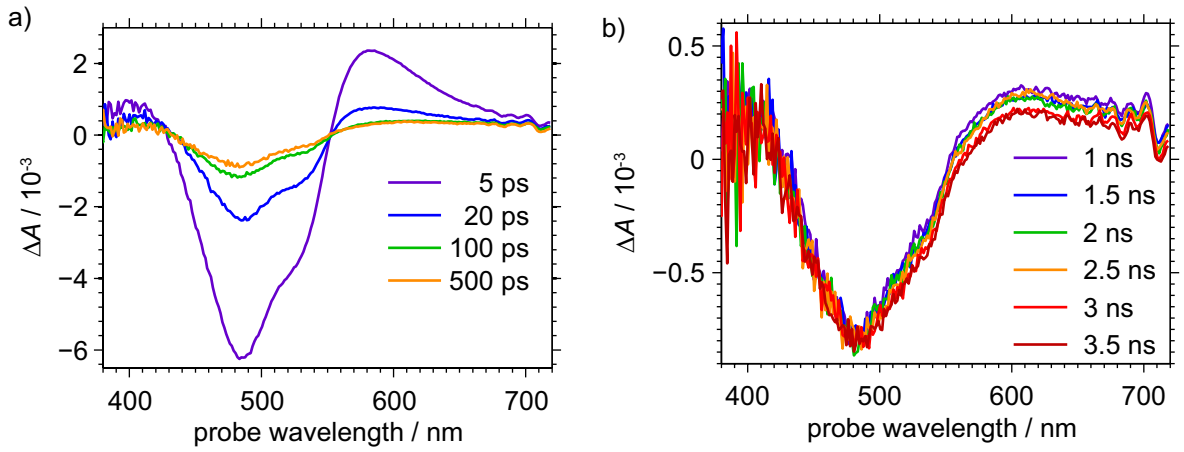

Figure A.3: Difference spectra of **TPF** in methanol for excitation at 296 nm. a) Difference spectra for a set of picosecond delay times. b) Difference spectra for long delay times up to 3.5 ns.

along a reaction path eventually leading to **TTC** again. It is important to note that the photodynamics of **TPF** clearly differ from the ultrafast signatures observed upon **TTC** in Section 6.2. Hence it can be excluded that **TPF** contributes in the latter experiments.

Table A.1 lists different solvent parameters for all used solvents. In Figs. 6.5 and A.4 the logarithmic rate of formation of **TTC•** is plotted against these parameters.

Table A.1: Solvent parameters of water and different alcohols and logarithmic rate of the formation of **TTC•**.

solvent	IE / eV	$E_T(30)^a$ / kcal/mol	Z^b / kcal/mol	α^b	β^b	π^{*b}	viscosity^c / mPa·s	pK^d_{auto}	lg(k/ps^{-1})
H_2O	12.65^e	63.1	94.6	1.17	0.47	1.09	0.89	14.00	-3.78
MeOH	10.85^f	55.4	83.6	0.98	0.66	0.60	0.54	16.91	-3.48
EtOH	10.41^g	51.9	79.6	0.86	0.75	0.54	1.07	19.10	-3.47
i-PrOH	10.15^h	48.4	76.3	0.76	0.84	0.48	2.04	21.08	-3.39
i-BuOH	10.02^i	48.6	77.7	0.79	0.84	0.40	3.40^j	21.08	-3.38

^{a}Ref. [277] Table 7-3, ^{b}Ref. [290] , ^{c}Ref. [291] , ^{d}Ref. [292] , ^{e}Ref. [293] , ^{f}Ref. [294] , ^{g}Ref. [295] , ^{h}Ref. [296] , ^{i}Ref. [297] , ^{j}Ref. [298]

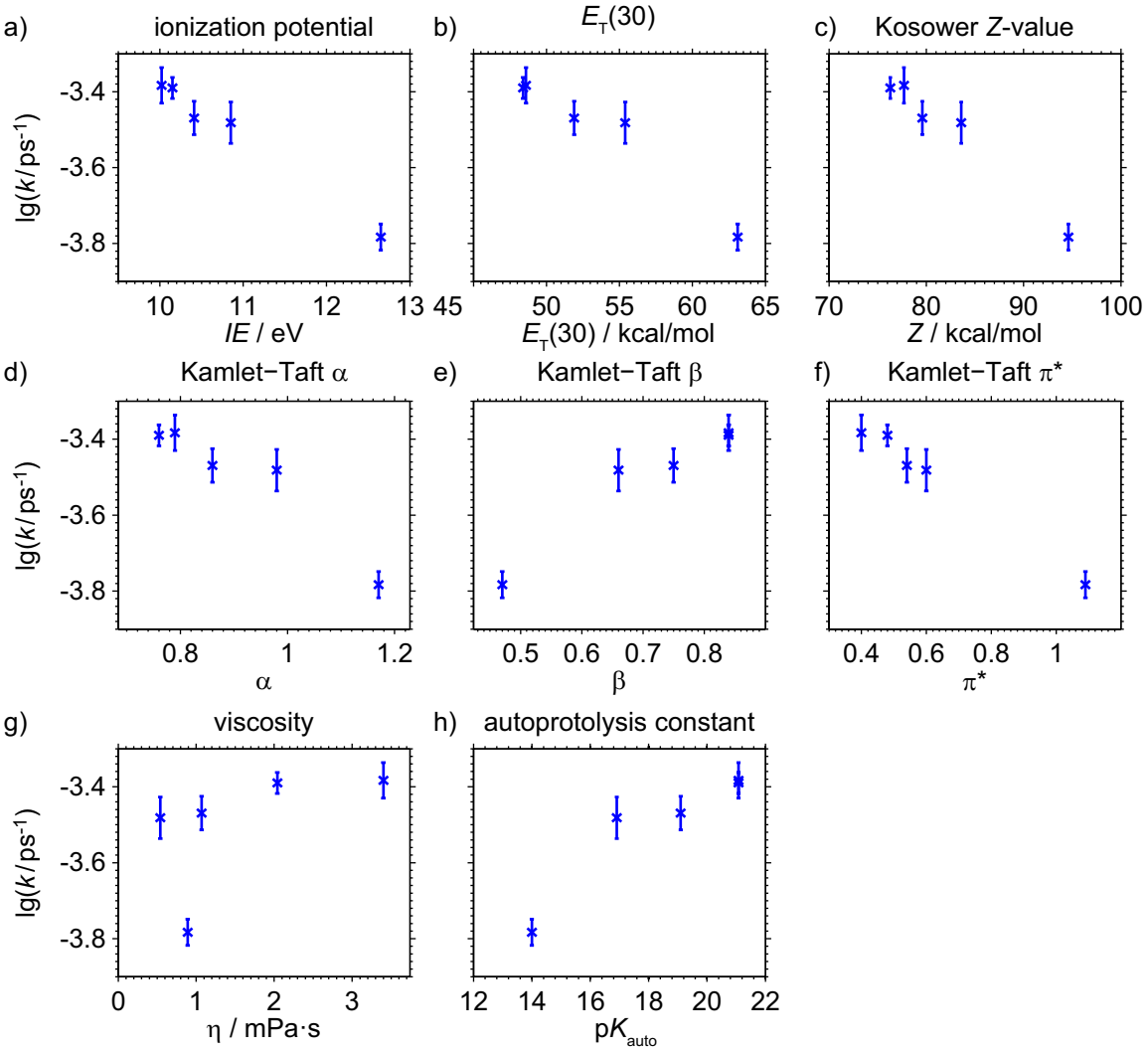

Figure A.4: Logarithm of the rate of formation of **TTC•** plotted against the solvent parameters given in Table A.1.

List of Abbreviations

UV	ultraviolet
Vis	visible
MIR	mid-infrared
τ	pump–probe delay time
NIR	near-infrared
A	absorbance
ΔA	change in absorbance
VC	vibrational cooling
IC	internal conversion
ISC	intersystem crossing
Fl	fluorescence
Ph	phosphorescence
GSB	ground-state bleaching
SE	stimulated emission
ESA	excited-state absorption
PA	product absorption
DADS	decay-associated difference spectrum
IRF	instrument response function
EADS	evolution-associated difference spectrum
Ti:Sa	titanium-doped sapphire
cw	continuous wave
τ_{P}	pulse length
FWHM	full width at half maximum
NLC	nonlinear crystal
SHG	second-harmonic generation
OPA	optical parametric amplification/amplifier
NOPA	noncollinear optical parametric amplification/amplifier
DFG	difference-frequency generation
SFG	sum-frequency generation
BBO	β barium borate
SPM	self-phase modulation
SCG	supercontinuum generation
ET	electron transfer
CT	charge transfer
MV	mixed valence
D	donor
A	acceptor

CR	charge recombination
PES	potential energy surface
NICG	neutral in cation geometry
FTIR	Fourier-transform infrared
LED	light-emitting diode
EOM	electro-optic modulator
Nd:YLF	neodymium-doped yttrium lithium fluoride
HM	hot mirror
CCD	charge-coupled device
MA	magic angle
HgCdTe	mercury cadmium telluride
τ_{PR}	pump–repump delay time
AOM	acousto-optic modulator
AOPDF	acousto-optic programmable dispersive filter
ADC	analog-to-digital converter
LSB	least significant bit
DC	duty cycle
PCTM	perchlorotriphenyl methyl radical
TAA	triarylamine
IVCT	intervalence charge transfer
DCM	dichloromethane
CO	carbon monoxide
CORM	CO-releasing molecule
TPA	two-photon absorption
MLCT	metal–ligand charge transfer
LMCT	ligand–metal charge transfer
Cp	cyclopentadienyl
tpm	tris(2-pyrazolyl)methane
TDDFT	time-dependent density functional theory
HOMO	highest occupied molecular orbital
LUMO	lowest unoccupied molecular orbital
DFT	density functional theory
PCM	polarizable continuum model
τ_{RPr}	repump–probe delay time
TTC	2,3,5-triphenyl-tetrazolium chloride
TPF	1,3,5-triphenyltetrazolium formazan
PTC	2-phenylbenzo[*c*]tetrazolo[2,3-*a*]cinnolin-4-ium
ESR	electron spin resonance
MeOH	methanol
EtOH	ethanol
***i*-PrOH**	2-propanol
***i*-BuOH**	2-methylpropan-1-ol

Bibliography

[1] D. Reitzenstein, T. Quast, F. Kanal, M. Kullmann, S. Ruetzel, M. S. Hammer, C. Deibel, V. Dyakonov, T. Brixner, and C. Lambert, "Synthesis and electron transfer characteristics of a neutral, low-band-gap, mixed-valence polyradical", Chem. Mater. **22**, 6641–6655 (2010).

[2] P. Rudolf, F. Kanal, J. Knorr, C. Nagel, J. Niesel, T. Brixner, U. Schatzschneider, and P. Nuernberger, "Ultrafast photochemistry of a manganese-tricarbonyl CO-releasing molecule (CORM) in aqueous solution", J. Phys. Chem. Lett. **4**, 596–602 (2013).

[3] P. Rudolf, F. Kanal, D. Gehrig, J. Niesel, T. Brixner, U. Schatzschneider, and P. Nuernberger, "Femtosecond mid-infrared study of the aqueous solution photochemistry of a CO-releasing molecule (CORM)", EPJ Web of Conferences **41**, 05004 (2013).

[4] F. Kanal, S. Keiber, R. Eck, and T. Brixner, "100-kHz shot-to-shot broadband data acquisition for high-repetition-rate pump–probe spectroscopy", Opt. Express **22**, 16965–16975 (2014).

[5] F. Kanal, S. Ruetzel, H. Lu, M. Moos, M. Holzapfel, T. Brixner, and C. Lambert, "Measuring charge-separation dynamics via oligomer length variation", J. Phys. Chem. C **118**, 23586–23598 (2014).

[6] F. Kanal, D. Schleier, and P. Nuernberger, "The ultrafast photogeneration of the tetrazolinyl radical", in preparation (2015).

[7] F. Kanal and P. Nuernberger, "Ultrafast spectroscopy on tetrazolium salts, formazans, and Photo-TTC", in preparation (2015).

[8] S. Rützel, "Pulse-sequence approaches for multidimensional electronic spectroscopy of ultrafast photochemistry", Dissertation, Universität Würzburg (2014).

[9] P. B. Rudolf, "Uncovering photoinduced chemical reaction pathways in the liquid phase with ultrafast vibrational spectroscopy", Dissertation, Universität Würzburg (2014).

[10] A. Mokhtari, P. Cong, J. L. Herek, and A. H. Zewail, "Direct femtosecond mapping of trajectories in a chemical reaction", Nature **348**, 225–227 (1990).

[11] A. H. Zewail, "Femtochemistry: recent progess in studies of dynamics and control of reactions and their transition states", J. Phys. Chem. **100**, 12701–12724 (1996).

[12] A. H. Zewail, "Femtochemistry: atomic-scale dynamics of the chemical bond", J. Phys. Chem. A **104**, 5660–5694 (2000).

[13] P. Klán and J. Wirz, *Photochemistry of Organic Compounds: from Concepts to Practice*, Postgraduate Chemistry Series (Wiley, Chichester, 2009).

[14] S. A. Kovalenko, A. L. Dobryakov, J. Ruthmann, and N. P. Ernsting, "Femtosecond spectroscopy of condensed phases with chirped supercontinuum probing", Phys. Rev. A **59**, 2369–2384 (1999).

[15] U. Megerle, I. Pugliesi, C. Schriever, C. Sailer, and E. Riedle, "Sub-50 fs broadband absorption spectroscopy with tunable excitation: putting the analysis of ultrafast molecular dynamics on solid ground", Appl. Phys. B **96**, 215–231 (2009).

[16] H. Haken, *Molekülphysik und Quantenchemie*, Springer-Lehrbuch (Springer, Berlin, 2006), 5th ed.

[17] N. J. Turro, V. Ramamurthy, and J. C. Scaiano, *Modern Molecular Photochemistry of Organic Molecules* (University Science Books, Sausalito, CA, 2010).

[18] A. Jabłoński, "Efficiency of anti-Stokes fluorescence in dyes", Nature **131**, 839–840 (1933).

[19] A. Jabłoński, "Über den Mechanismus der Photolumineszenz von Farbstoffphosphoren", Z. Physik **94**, 38–46 (1935).

[20] T. A. Roelofs, C.-H. Lee, and A. R. Holzwarth, "Global target analysis of picosecond chlorophyll fluorescence kinetics from pea chloroplasts: a new approach to the characterization of the primary processes in photosystem II α- and β-units", Biophys. J. **61**, 1147–1163 (1992).

[21] J. Amesz and A. J. Hoff, eds., *Biophysical Techniques in Photosynthesis*, vol. 3 of *Advances in Photosynthesis and Respiration* (Kluwer Academic Publishers, Dordrecht, 1996).

[22] H. Satzger and W. Zinth, "Visualization of transient absorption dynamics – towards a qualitative view of complex reaction kinetics", Chem. Phys. **295**, 287–295 (2003).

[23] I. H. M. van Stokkum, D. S. Larsen, and R. van Grondelle, "Global and target analysis of time-resolved spectra", Biochim. Biophys. Acta, Bioenerg. **1657**, 82–104 (2004).

[24] L. J. G. W. van Wilderen, C. N. Lincoln, and J. J. van Thor, "Modelling multi-pulse population dynamics from ultrafast spectroscopy", PLoS ONE **6**, e17373 (2011).

[25] M. Berberan-Santos, E. Bodunov, and B. Valeur, "Mathematical functions for the analysis of luminescence decays with underlying distributions 1. Kohlrausch decay function (stretched exponential)", Chem. Phys. **315**, 171–182 (2005).

[26] P. Pernot, "Analyse baeyésienne des données pour la modélisation des signaux spectro-cinetiques", in "Réactions ultrarapides en solution: approches expérimentales et théoriques," , M. Mostafavi and T. Gustavsson, eds. (CNRS Edition, 2007), pp. 191–213.

[27] R. Croce, M. G. Müller, R. Bassi, and A. R. Holzwarth, "Carotenoid-to-chlorophyll energy transfer in recombinant major light-harvesting complex (LHCII) of higher plants. I. Femtosecond transient absorption measurements", Biophys. J. **80**, 901–915 (2001).

[28] M. G. Müller, J. Niklas, W. Lubitz, and A. R. Holzwarth, "Ultrafast transient absorption studies on Photosystem I reaction centers from *chlamydomonas reinhardtii*. 1. A new interpretation of the energy trapping and early electron transfer steps in Photosystem I", Biophys. J. **85**, 3899–3922 (2003).

[29] M. G. Müller, I. Lindner, I. Martin, W. Gärtner, and A. R. Holzwarth, "Femtosecond kinetics of photoconversion of the higher plant photoreceptor phytochrome carrying native and modified chromophores", Biophys. J. **94**, 4370–4382 (2008).

[30] E. R. Henry, "The use of matrix methods in the modeling of spectroscopic data sets", Biophys. J. **72**, 652–673 (1997).

[31] J. J. Snellenburg, S. P. Laptenok, R. Seger, K. M. Mullen, and I. H. M. van Stokkum, "Glotaran: a Java-based graphical user interface for the R-package TIMP", J. Stat. Softw. **49**, 1–22 (2012).

[32] K. M. Mullen and I. H. M. van Stokkum, "TIMP: an R package for modeling multi-way spectroscopic measurements", J. Stat. Softw. **18**, 1–46 (2007).

[33] R Core Team, *R: a Language and Environment for Statistical Computing*, R Foundation for Statistical Computing, Vienna, Austria (2013). ISBN 3-900051-07-0, http://www.R-project.org.

[34] R. K. Jain and C. P. Ausschnitt, "Subpicosecond pulse generation in a synchronously mode-locked cw rhodamine 6G dye laser", Opt. Lett. **2**, 117–119 (1978).

[35] T. Sizer II, J. D. Kafka, C. Gable, and G. Mourou, "Generation and amplification of 70 fs pulses using a frequency-doubled Nd:YAG pumping source", Appl Phys. B **29**, 248 (1982).

[36] M. Wollenhaupt, A. Assion, and T. Baumert, "Femtosecond laser pulses: linear properties, manipulation, generation and measurement", in "Springer Handbook of Lasers and Optics," , F. Träger, ed. (Springer Science+Business Media, New York, 2007), pp. 937–983.

[37] R. W. Boyd, *Nonlinear Optics* (Academic Press, Burlington, 2008), 3rd ed.

[38] A. M. Weiner, *Ultrafast Optics* (John Wiley & Sons Inc., Hoboken, 2009).

[39] D. E. Spence, P. N. Kean, and W. Sibbett, "60-fsec pulse generation from a self-mode-locked Ti:sapphire laser", Opt. Lett. **16**, 42–44 (1991).

[40] P. F. Moulton, "Spectroscopic and laser characteristics of Ti:Al_2O_3", J. Opt. Soc. Am. B **3**, 125–133 (1986).

[41] P. A. Franken, A. E. Hill, C. W. Peters, and G. Weinreich, "Generation of optical harmonics", Phys. Rev. Lett. **7**, 118 (1961).

[42] T. J. Driscoll, G. M. Gale, and F. Hache, "Ti:sapphire second-harmonic-pumped visible range femtosecond optical parametric oscillator", Opt. Commun. **110**, 638–644 (1994).

[43] G. M. Gale, M. Cavallari, T. J. Driscoll, and F. Hache, "Sub-20-fs tunable pulses in the visible from an 82-MHz optical parametric oscillator", Opt. Lett. **20**, 1562–1564 (1995).

[44] P. Hamm, R. A. Kaindl, and J. Stenger, "Noise suppression in femtosecond mid-infrared light sources", Opt. Lett. **25**, 1798–1800 (2000).

[45] M. K. Reed, M. K. Steiner-Shepard, and D. K. Negus, "Widely tunable femtosecond optical parametric amplifier at 250 kHz with a Ti:sapphire regenerative amplifier", Opt. Lett. **19**, 1855–1857 (1994).

[46] A. Brodeur and S. L. Chin, "Band-gap dependence of the ultrafast white-light continuum", Phys. Rev. Lett. **80**, 4406 (1998).

[47] R. Huber, H. Satzger, W. Zinth, and J. Wachtveitl, "Noncollinear optical parametric amplifiers with output parameters improved by the application of a white light continuum generated in CaF_2", Opt. Commun. **194**, 443–448 (2001).

[48] C. Nagura, A. Suda, H. Kawano, M. Obara, and K. Midorikawa, "Generation and characterization of ultrafast white-light continuum in condensed media", Appl. Opt. **41**, 3735–3742 (2002).

[49] C. Romero, R. Borrego-Varillas, A. Camino, G. Mínguez-Vega, O. Mendoza-Yero, J. Hernández-Toro, and J. R. Vázquez de Aldana, "Diffractive optics for spectral control of the supercontinuum generated in sapphire with femtosecond pulses", Opt. Express **19**, 4977–4984 (2011).

[50] J. Kohl-Landgraf, J.-E. Nimsch, and J. Wachtveitl, "LiF, an underestimated supercontinuum source in femtosecond transient absorption spectroscopy", Opt. Express **21**, 17060–17065 (2013).

[51] L. Eberson, *Electron Transfer Reactions in Organic Chemistry*, vol. 25 of *Reactivity and Structure Concepts in Organic Chemistry* (Springer, Berlin Heidelberg, 1987).

[52] G. J. Kavarnos, *Fundamentals of Photoinduced Electron Transfer* (VCH Publishers, New York, NY, 1993).

[53] V. Balzani, ed., *Electron Transfer in Chemistry* (Wiley-VCH, Weinheim, 2001).

[54] J.-L. Brédas, D. Beljonne, V. Coropceanu, and J. Cornil, "Charge-transfer and energy-transfer processes in π-conjugated oligomers and polymers: a molecular picture", Chem. Rev. **104**, 4971–5004 (2004).

[55] J. Hankache and O. S. Wenger, "Organic mixed valence", Chem. Rev. **111**, 5138–5178 (2011).

[56] A. Heckmann and C. Lambert, "Organic mixed-valence compounds: a playground for electrons and holes", Angew. Chem. Int. Ed. **51**, 326–392 (2012).

[57] M. Parthey and M. Kaupp, "Quantum-chemical insights into mixed-valence systems: within and beyond the Robin–Day scheme", Chem. Soc. Rev. **43**, 5067–5088 (2014).

[58] B. J. Zwolinski, R. J. Marcus, and H. Eyring, "Inorganic oxidation–reduction reactions in solution electron transfers", Chem. Rev. **55**, 157–180 (1955).

[59] C. Creutz and H. Taube, "Direct approach to measuring the Franck–Condon barrier to electron transfer between metal ions", J. Am. Chem. Soc. **91**, 3988–3989 (1969).

[60] R. A. Marcus, "On the theory of oxidation-reduction reactions involving electron transfer. I", J. Chem. Phys. **24**, 966 (1956).

[61] W. F. Libby, "Theory of electron exchange reactions in aqueous solution", J. Phys. Chem. **56**, 863–868 (1952).

[62] A. Weller, "Photoinduced electron transfer in solution: exciplex and radical ion pair formation free enthalpies and their solvent dependence", Z. Phys. Chem. Neue Folge **133**, 93–98 (1982).

[63] H. Heitele, "Dynamic solvent effects on electron-transfer reactions", Angew. Chem. Int. Ed. **32**, 359–377 (1993).

[64] Thu Ba Truong, "Charge transfer to a solvent state. 9. Effect of solvent reorganization energy on electron-transfer reaction rate constant. The Marcus inverted region", J. Phys. Chem. **88**, 3906–3913 (1984).

[65] B. S. Brunschwig, S. Ehrenson, and N. Sutin, "Solvent reorganization in optical and thermal electron-transfer processes", J. Phys. Chem. **90**, 3657–3668 (1986).

[66] J. R. Miller, L. T. Calcaterra, and G. L. Closs, "Intramolecular long-distance electron transfer in radical anions. The effects of free energy and solvent on the reaction rates", J. Am. Chem. Soc. **106**, 3047–3049 (1984).

[67] J. Jortner and M. Bixon, "Intramolecular vibrational excitations accompanying solvent-controlled electron transfer reactions", J. Chem. Phys. **88**, 167–170 (1988).

[68] R. Maksimenka, M. Margraf, J. Köhler, A. Heckmann, C. Lambert, and I. Fischer, "Femtosecond dynamics of electron transfer in a neutral organic mixed-valence compound", Chem. Phys. **347**, 436–445 (2008).

[69] A. Heckmann, C. Lambert, M. Goebel, and R. Wortmann, "Synthesis and photophysics of a neutral organic mixed-valence compound", Angew. Chem. Int. Ed. **43**, 5851–5856 (2004).

[70] A. Heckmann and C. Lambert, "Neutral organic mixed-valence compounds: synthesis and all-optical evaluation of electron-transfer parameters", J. Am. Chem. Soc. **129**, 5515–5527 (2007).

[71] S. F. Nelsen, M. T. Ramm, J. J. Wolff, and D. R. Powell, "Intramolecular electron transfer between doubly four σ-bond-linked tetraalkylhydrazine cationic and neutral units", J. Am. Chem. Soc. **119**, 6863–6872 (1997).

[72] Spectra-Physics, *Solstice - One-box ultrafast amplifier system* (2008).

[73] Spectra Physics, *Mai Tai - Diode-pumped mode-locked Ti:sapphire laser* (2002).

[74] Spectra Physics, *Empower - User's Manual* (2005).

[75] M. Kullmann, "Transiente Absorptionsspektroskopie an einem molekularen Schalter auf Spiropyranbasis", Diplomarbeit, Universität Würzburg (2009).

[76] J. Buback, "Femtochemistry of pericyclic reactions and advances towards chiral control", Dissertation, Universität Würzburg (2011).

[77] S. Schott, A. Steinbacher, J. Buback, P. Nuernberger, and T. Brixner, "Generalized magic angle for time-resolved spectroscopy with laser pulses of arbitrary ellipticity", J. Phys. B: At. Mol. Opt. Phys. **47**, 124014 (2014).

[78] P. Hamm, S. Wiemann, M. Zurek, and W. Zinth, "Highly sensitive multichannel spectrometer for subpicosecond spectroscopy in the midinfrared", Opt. Lett. **19**, 1642–1644 (1994).

[79] D. Wolpert, "Quantum control of photoinduced chemical reactions", Dissertation, Universität Würzburg (2008).

[80] F. Gai, J. C. McDonald, and P. A. Anfinrud, "Pump–dump–probe spectroscopy of bacteriorhodosin: evidence for a near-IR excited state absorbance", J. Am. Chem. Soc. **119**, 6201–6202 (1997).

[81] S. A. Kovalenko, J. Ruthmann, and N. P. Ernsting, "Femtosecond hole-burning spectroscopy with stimulated emission pumping and supercontinuum probing", J. Chem. Phys. **109**, 1894–1900 (1998).

[82] P. Changenet-Barret, C. T. Choma, E. F. Gooding, W. F. DeGrado, and R. M. Hochstrasser, "Ultrafast dielectric response of proteins from dynamics Stokes shifting of coumarin in calmodulin", J. Phys. Chem. B **104**, 9322–9329 (2000).

[83] D. S. Larsen, E. Papagiannakis, I. H. M. van Stokkum, M. Vengris, J. T. M. Kennis, and R. van Grondelle, "Excited state dynamics of β-carotene explored with dispersed multi-pulse transient absorption", Chem. Phys. Lett. **381**, 733–742 (2003).

[84] E. Papagiannakis, M. Vengris, D. S. Larsen, I. H. M. van Stokkum, R. G. Hiller, and R. van Grondelle, "Use of ultrafast dispersed pump–dump–probe and pump–repump–probe spectroscopies to explore the light-induced dynamics of peridinin in solution", J. Phys. Chem. B **110**, 512–521 (2006). 00058.

[85] S. Draxler, T. Brust, J. Eicher, W. Zinth, and M. Braun, "Novel detection scheme for application in pump–pepump–probe spectroscopy", Opt. Commun. **283**, 1050–1054 (2010).

[86] J. Buback, M. Kullmann, F. Langhojer, P. Nuernberger, R. Schmidt, F. Würthner, and T. Brixner, "Ultrafast bidirectional photoswitching of a spiropyran", J. Am. Chem. Soc. **132**, 16510–16519 (2010).

[87] S. Ruetzel, M. Kullmann, J. Buback, P. Nuernberger, and T. Brixner, "Tracing the steps of photoinduced chemical reactions in organic molecules by coherent two-dimensional electronic spectroscopy using triggered exchange", Phys. Rev. Lett. **110**, 148305 (2013).

[88] S. Keiber, "Investigation of the electron transfer properties of a neutral mixed-valence polymer and introduction of a shot-to-shot readout mechanism for high repitition rates", Master thesis, Universität Würzburg (2011).

[89] T. Polack, "Spectroscopie infrarouge impulsionnelle appliquée au transfert de ligands dans les hémoprotéines", Dissertation, École Polytechnique, Paris (2003).

[90] T. Polack, J. P. Ogilvie, S. Franzen, M. H. Vos, M. Joffre, J.-L. Martin, and A. Alexandrou, "CO vibration as a probe of ligand dissociation and transfer in myoglobin", Phys. Rev. Lett. **93**, 018102 (2004).

[91] G. Auböck, C. Consani, R. Monni, A. Cannizzo, F. v. Mourik, and M. Chergui, "Femtosecond pump/supercontinuum-probe setup with 20 kHz repetition rate", Rev. Sci. Instrum. **83**, 093105 (2012).

[92] Coherent Inc., "Operator's manual, Mira model 900-b laser", (1993).

[93] Coherent Inc., "Operator's manual, Verdi V-18 diode-pumped lasers", (2005).

[94] Coherent Inc., "Operator's manual, RegA model 9000 laser", (1997).

[95] S. Karg, "Transiente Absorptionsspektroskopie im sichtbaren Spektralbereich", Diplomarbeit, Universität Würzburg (2009).

[96] F. Kanal, "Untersuchung lichtinduzierter Ladungstransfer-Prozesse mittels transienter Absorptionsspektroskopie im sichtbaren Spektralbereich", Diplomarbeit, Universität Würzburg (2010).

[97] T. Quast, "Spectroscopic investigations of charge-transfer processes and polarisation pulse shaping in the visible spectral range", Dissertation, Universität Würzburg (2012).

[98] P. Tournois, "Acousto-optic programmable dispersive filter for adaptive compensation of group delay time dispersion in laser systems", Opt. Commun. **140**, 245–249 (1997).

[99] S. D. McClure, D. B. Turner, P. C. Arpin, T. Mirkovic, and G. D. Scholes, "Coherent oscillations in the PC577 cryptophyte antenna occur in the excited electronic state", J. Phys. Chem. B **118**, 1296–1308 (2014).

[100] J. Piel, E. Riedle, L. Gundlach, R. Ernstorfer, and R. Eichberger, "Sub-20 fs visible pulses with 750 nJ energy from a 100 kHz noncollinear optical parametric amplifier", Opt. Lett. **31**, 1289–1291 (2006).

[101] Y. H. Meyer, M. Pittman, and P. Plaza, "Transient absorption of symmetrical carbocyanines", J. Photochem. Photobiol. A **114**, 1–21 (1998).

[102] D. Wang, H. Jiang, H. Yang, C. Liu, Q. Gong, J. Xiang, and G. Xu, "Investigation on photoexcited dynamics of IR-140 dye in ethanol by femtosecond supercontinuum-probing technique", J. Opt. A: Pure Appl. Opt. **4**, 155–159 (2002).

[103] D. Wang, H. Jiang, S. Wu, H. Yang, Q. Gong, J. Xiang, and G. Xu, "An investigation of solvent effects on the optical properties of dye IR-140 using the pump supercontinuum-probing technique", J. Opt. A: Pure Appl. Opt. **5**, 515–519 (2003).

[104] M. Bradler, P. Baum, and E. Riedle, "Femtosecond continuum generation in bulk laser host materials with sub-μJ pump pulses", Appl. Phys. B **97**, 561–574 (2009).

[105] C. Schriever, S. Lochbrunner, E. Riedle, and D. J. Nesbitt, "Ultrasensitive ultraviolet-visible 20 fs absorption spectroscopy of low vapor pressure molecules in the gas phase", Rev. Sci. Instrum. **79**, 013107 (2008).

[106] D. Polli, L. Lüer, and G. Cerullo, "High-time-resolution pump-probe system with broadband detection for the study of time-domain vibrational dynamics", Rev. Sci. Instrum. **78**, 103108 (2007).

[107] D. Linde, "Characterization of the noise in continuously operating mode-locked lasers", Appl. Phys. B **39**, 201–217 (1986).

[108] M. J. Feldstein, P. Vöhringer, and N. F. Scherer, "Rapid-scan pump–probe spectroscopy with high time and wave-number resolution: optical-Kerr-effect measurements of neat liquids", J. Opt. Soc. Am. B **12**, 1500–1510 (1995).

[109] A. Yabushita, Y.-H. Lee, and T. Kobayashi, "Development of a multiplex fast-scan system for ultrafast time-resolved spectroscopy", Rev. Sci. Instrum. **81**, 063110 (2010).

[110] K. F. Lee, A. Bonvalet, P. Nuernberger, and M. Joffre, "Unobtrusive interferometer tracking by pathlength oscillation for multidimensional spectroscopy", Opt. Express **17**, 12379–12384 (2009).

[111] P. Nuernberger, K. F. Lee, A. Bonvalet, M. H. Vos, and M. Joffre, "Multiply excited vibration of carbon monoxide in the primary docking site of hemoglobin following photolysis from the heme", J. Phys. Chem. Lett. **1**, 2077–2081 (2010).

[112] H. Lu, "Preparation and characterization of neutral organic mixed valence oligomers and dimer", Diplomarbeit, Universität Würzburg (2012).

[113] C. Slavov, M. Ballottari, T. Morosinotto, R. Bassi, and A. R. Holzwarth, "Trap-limited charge separation kinetics in higher plant photosystem I complexes", Biophys. J. **94**, 3601–3612 (2008).

[114] M. Szczepaniak, J. Sander, M. Nowaczyk, M. G. Müller, M. Rögner, and A. R. Holzwarth, "Charge separation, stabilization, and protein relaxation in photosystem II core particles with closed reaction center", Biophys. J. **96**, 621–631 (2009).

[115] N. P. Pawlowicz, R. van Grondelle, I. H. M. van Stokkum, J. Breton, M. R. Jones, and M. L. Groot, "Identification of the first steps in charge separation in bacterial photosynthetic reaction centers of *rhodobacter sphaeroides* by ultrafast mid-infrared spectroscopy: electron transfer and protein dynamics", Biophys. J. **95**, 1268–1284 (2008).

[116] J. Zhu, I. H. M. van Stokkum, L. Paparelli, M. R. Jones, and M. L. Groot, "Early bacteriopheophytin reduction in charge separation in reaction centers of *rhodobacter sphaeroides*", Biophys. J. **104**, 2493–2502 (2013).

[117] M. Di Donato, A. D. Stahl, I. H. M. van Stokkum, R. van Grondelle, and M.-L. Groot, "Cofactors involved in light-driven charge separation in photosystem I identified by subpicosecond infrared spectroscopy", Biochemistry **50**, 480–490 (2011).

[118] E. Romero, I. H. M. van Stokkum, V. I. Novoderezhkin, J. P. Dekker, and R. van Grondelle, "Two different charge separation pathways in photosystem II", Biochemistry **49**, 4300–4307 (2010).

[119] A. Espagne, P. Changenet-Barret, J.-B. Baudin, P. Plaza, and M. M. Martin, "Photoinduced charge shift as the driving force for the excited-state relaxation of analogues of the photoactive yellow protein chromophore in solution", J. Photochem. Photobiol., A **185**, 245–252 (2007).

[120] W. Zinth and J. Wachtveitl, "The first picoseconds in bacterial photosynthesis—ultrafast electron transfer for the efficient conversion of light energy", ChemPhysChem **6**, 871–880 (2005).

[121] J. Petersson, M. Eklund, J. Davidsson, and L. Hammarström, "Ultrafast electron transfer dynamics of a Zn(II)porphyrin–viologen complex revisited: S_2 vs S_1 reactions and survival of excess excitation energy", J. Phys. Chem. B **114**, 14329–14338 (2010).

[122] W. Akemann, D. Laage, P. Plaza, M. M. Martin, and M. Blanchard-Desce, "Photoinduced intramolecular charge transfer in push–pull polyenes: effects of solvation, electron-donor group, and polyenic chain length", J. Phys. Chem. B **112**, 358–368 (2008).

[123] S. Bhosale, A. L. Sisson, P. Talukdar, A. Fürstenberg, N. Banerji, E. Vauthey, G. Bollot, J. Mareda, C. Röger, F. Würthner, N. Sakai, and S. Matile, "Photoproduction of proton gradients with π-stacked fluorophore scaffolds in lipid bilayers", Science **313**, 84–86 (2006).

[124] M. R. Wasielewski, "Self-assembly strategies for integrating light harvesting and charge separation in artificial photosynthetic systems", Acc. Chem. Res. **42**, 1910–1921 (2009).

[125] D. Villamaina, M. M. A. Kelson, S. V. Bhosale, and E. Vauthey, "Excitation wavelength dependence of the charge separation pathways in tetraporphyrin-naphthalene diimide pentads", Phys. Chem. Chem. Phys. **16**, 5188–5200 (2014).

[126] R. Letrun and E. Vauthey, "Excitation wavelength dependence of the dynamics of bimolecular photoinduced electron transfer reactions", J. Phys. Chem. Lett. **5**, 1685–1690 (2014).

[127] A. Rosspeintner, G. Angulo, and E. Vauthey, "Bimolecular photoinduced electron transfer beyond the diffusion limit: the Rehm–Weller experiment revisited with femtosecond time resolution", J. Am. Chem. Soc. **136**, 2026–2032 (2014).

[128] S. Dümmler, W. Roth, I. Fischer, A. Heckmann, and C. Lambert, "Excited-state dynamics in a neutral organic mixed-valence compound", Chem. Phys. Lett. **408**, 264–268 (2005).

[129] O. F. Mohammed, "Ultrafast intramolecular charge transfer of formyl perylene observed using femtosecond transient absorption spectroscopy", J. Phys. Chem. A **114**, 11576–11582 (2010).

[130] S. A. Kovalenko, N. Eilers-König, T. A. Senyushkina, and N. P. Ernsting, "Charge transfer and solvation of betaine-30 in polar solvents—a femtosecond broadband transient absorption study", J. Phys. Chem. A **105**, 4834–4843 (2001).

[131] O. Bixner, V. Lukeš, T. Mančal, J. Hauer, F. Milota, M. Fischer, I. Pugliesi, M. Bradler, W. Schmid, E. Riedle, H. F. Kauffmann, and N. Christensson, "Ultrafast photo-induced charge transfer unveiled by two-dimensional electronic spectroscopy", J. Chem. Phys. **136**, 204503 (2012).

[132] C. Consani, G. Auböck, F. v. Mourik, and M. Chergui, "Ultrafast tryptophan-to-heme electron transfer in myoglobins revealed by UV 2D spectroscopy", Science **339**, 1586–1589 (2013).

[133] R. G. Kepler, "Charge carrier production and mobility in anthracene crystals", Phys. Rev. **119**, 1226–1229 (1960).

[134] M. Gailberger and H. Bässler, "dc and transient photoconductivity of poly(2-phenyl-1,4-phenylenevinylene)", Phys. Rev. B **44**, 8643–8651 (1991).

[135] H. Meyer, D. Haarer, H. Naarmann, and H. H. Hörhold, "Trap distribution for charge carriers in poly(paraphenylene vinylene) (PPV) and its substituted derivative DPOP-PPV", Phys. Rev. B **52**, 2587–2598 (1995).

[136] J. Veres, S. Ogier, G. Lloyd, and D. de Leeuw, "Gate insulators in organic field-effect transistors", Chem. Mater. **16**, 4543–4555 (2004).

[137] D. Reitzenstein, "Donor-acceptor conjugated polymers for applications in organic electronic devices", Dissertation, Universität Würzburg (2010).

[138] I. Ratera and J. Veciana, "Playing with organic radicals as building blocks for functional molecular materials", Chem. Soc. Rev. **41**, 303–349 (2011).

[139] A. Heckmann, S. Dümmler, J. Pauli, M. Margraf, J. Köhler, D. Stich, C. Lambert, I. Fischer, and U. Resch-Genger, "Highly fluorescent open-shell NIR dyes: the time-dependence of back electron transfer in triarylamine-perchlorotriphenylmethyl radicals", J. Phys. Chem. C **113**, 20958–20966 (2009).

[140] S. Amthor, B. Noller, and C. Lambert, "UV/Vis/NIR spectral properties of triarylamines and their corresponding radical cations", Chem. Phys. **316**, 141–152 (2005).

[141] M. Ballester, "Perchloro-organic chemistry: structure, spectroscopy and reaction pathways", in "Advances in Physical Organic Chemistry," , vol. 25, D. Bethell, ed. (Academic Press, 1989), pp. 267–445.

[142] C. Rovira, D. Ruiz-Molina, O. Elsner, J. Vidal-Gancedo, J. Bonvoisin, J.-P. Launay, and J. Veciana, "Influence of topology on the long-range electron-transfer phenomenon", Chem. Eur. J. **7**, 240–250 (2001).

[143] C. Sporer, I. Ratera, D. Ruiz-Molina, Y. Zhao, J. Vidal-Gancedo, K. Wurst, P. Jaitner, K. Clays, A. Persoons, C. Rovira, and J. Veciana, "A Molecular Multiproperty Switching Array Based on the Redox Behavior of a Ferrocenyl Polychlorotriphenylmethyl Radical", Angew. Chem. Int. Ed. **43**, 5266–5268 (2004).

[144] W. Schmidt and E. Steckhan, "Über organische Elektronenüberträgersysteme, I. Elektrochemische und spektroskopische Untersuchung bromsubstituierter Triarylamin-Redoxsysteme", Chem. Ber. **113**, 577–585 (1980).

[145] M. Ballester and I. Pascual, "'Spin-charge exchange' in a stable radical-carbanion, and related intermolecular one-electron transfers", Tetrahedron Lett. **26**, 5589–5592 (1985).

[146] J.-P. Foing, M. Joffre, J.-L. Oudar, and D. Hulin, "Coherence effects in pump–probe experiments with chirped pump pulses", J. Opt. Soc. Am. B **10**, 1143–1148 (1993).

[147] J.-P. Likforman, M. Joffre, G. Chériaux, and D. Hulin, "Control of the spectral-oscillation artifact in femtosecond pump–probe spectroscopy", Opt. Lett. **20**, 2006–2008 (1995).

[148] K. Ekvall, P. van der Meulen, C. Dhollande, L.-E. Berg, S. Pommeret, R. Naskrecki, and J.-C. Mialocq, "Cross phase modulation artifact in liquid phase transient absorption spectroscopy", J. Appl. Phys. **87**, 2340 (2000).

[149] M. Lorenc, M. Ziolek, R. Naskrecki, J. Karolczak, J. Kubicki, and A. Maciejewski, "Artifacts in femtosecond transient absorption spectroscopy", Appl. Phys. B: Lasers Opt. **74**, 19–27 (2002).

[150] L. Reynolds, J. A. Gardecki, S. J. V. Frankland, M. L. Horng, and M. Maroncelli, "Dipole solvation in nondipolar solvents: experimental studies of reorganization energies and solvation dynamics", J. Phys. Chem. **100**, 10337–10354 (1996).

[151] E. A. Carter and J. T. Hynes, "Solvation dynamics for an ion pair in a polar solvent: time-dependent fluorescence and photochemical charge transfer", Chem. Phys. **94**, 5961–5979 (1991).

[152] "ChemBio3D Ultra 3.0", (2010).

[153] M. J. Frisch, G. W. Trucks, H. B. Schlegel, G. E. Scuseria, M. A. Robb, J. R. Cheeseman, G. Scalmani, V. Barone, B. Mennucci, G. A. Petersson, H. Nakatsuji, M. Caricato, X. Li, H. P. Hratchian, A. F. Izmaylov, J. Bloino, G. Zheng, J. L. Sonnenberg, M. Hada, M. Ehara, K. Toyota, R. Fukuda, J. Hasegawa, M. Ishida, T. Nakajima, Y. Honda, O. Kitao, H. Nakai, T. Vreven, J. A. Montgomery, Jr., J. E. Peralta, F. Ogliaro, M. Bearpark, J. J. Heyd, E. Brothers, K. N. Kudin, V. N. Staroverov, R. Kobayashi, J. Normand, K. Raghavachari, A. Rendell, J. C. Burant, S. S. Iyengar, J. Tomasi, M. Cossi, N. Rega, J. M. Millam, M. Klene, J. E. Knox, J. B. Cross, V. Bakken, C. Adamo, J. Jaramillo, R. Gomperts, R. E. Stratmann, O. Yazyev, A. J. Austin, R. Cammi, C. Pomelli, J. W. Ochterski, R. L. Martin, K. Morokuma, V. G. Zakrzewski, G. A. Voth, P. Salvador, J. J. Dannenberg, S. Dapprich, A. D. Daniels, O. Farkas, J. B. Foresman, J. V. Ortiz, J. Cioslowski, and D. J. Fox, "Gaussian 09, revision B.01", (2009). Gaussian Inc. Wallingford CT 2009.

[154] I. R. Gould, D. Noukakis, L. Gomez-Jahn, R. H. Young, J. L. Goodman, and S. Farid, "Radiative and nonradiative electron transfer in contact radical-ion pairs", Chem. Phys. **176**, 439–456 (1993).

[155] J. Cortes, H. Heitele, and J. Jortner, "Band-shape analysis of the charge-transfer fluorescence in barrelene-based electron donor–acceptor compounds", J. Phys. Chem. **98**, 2527–2536 (1994).

[156] P. Cias, C. Slugovc, and G. Gescheidt, "Hole transport in triphenylamine based OLED devices: from theoretical modeling to properties prediction", J. Phys. Chem. A **115**, 14519–14525 (2011).

[157] The inner reorganization energy of the PCTM moiety was calculated with the "neutral in cation geometry" (NICG) by DFT, B3LYP, 6-31G* using Gaussian09, analogous to Ref. [156].

[158] R. C. Weast and D. R. Lide, *CRC Handbook of Chemistry and Physics, 70th Edition* (CRC Press, 1989).

[159] C. Reichardt, "Solvatochromic dyes as solvent polarity indicators", Chem. Rev. **94**, 2319–2358 (1994).

[160] H. Marciniak, X.-Q. Li, F. Würthner, and S. Lochbrunner, "One-dimensional exciton diffusion in perylene bisimide aggregates", J. Phys. Chem. A **115**, 648–654 (2011).

[161] Y. Zaushitsyn, K. G. Jespersen, L. Valkunas, V. Sundström, and A. Yartsev, "Ultrafast dynamics of singlet-singlet and singlet-triplet exciton annihilation in poly(3-2′-methoxy-5′octylphenyl)thiophene films", Phys. Rev. B **75**, 195201 (2007).

[162] L. Wu and R. Wang, "Carbon monoxide: endogenous production, physiological functions, and pharmacological applications", Pharmacol. Rev. **57**, 585–630 (2005).

[163] R. Alberto and R. Motterlini, "Chemistry and biological activities of CO-releasing molecules (CORMs) and transition metal complexes", Dalton Trans. pp. 1651–1660 (2007).

[164] U. Schatzschneider, "Novel lead structures and activation mechanisms for CO-releasing molecules (CORMs)", Br. J. Pharmacol. **172**, 1638–1650 (2015).

[165] H.-J. Galla, "Nitric oxide, NO, an intercellular messenger", Angew. Chem. Int. Ed. **32**, 378–380 (1993).

[166] A. Verma, D. J. Hirsch, C. E. Glatt, G. V. Ronnett, and S. H. Snyder, "Carbon monoxide: a putative neural messenger", Science **259**, 381–384 (1993).

[167] S. Hou, S. H. Heinemann, and T. Hoshi, "Modulation of BKCa channel gating by endogenous signaling molecules", Physiology **24**, 26–35 (2009).

[168] R. Motterlini and L. E. Otterbein, "The therapeutic potential of carbon monoxide", Nat. Rev. Drug Discovery **9**, 728–743 (2010).

[169] S. Hou, R. Xu, S. H. Heinemann, and T. Hoshi, "The RCK1 high-affinity Ca^{2+} sensor confers carbon monoxide sensitivity to Slo1 BK channels", Proc. Natl. Acad. Sci. U. S. A. **105**, 4039–4043 (2008).

[170] C. C. Romão, W. A. Blättler, J. D. Seixas, and G. J. L. Bernardes, "Developing drug molecules for therapy with carbon monoxide", Chem. Soc. Rev. **41**, 3571–3583 (2012).

[171] R. Motterlini, J. E. Clark, R. Foresti, P. Sarathchandra, B. E. Mann, and C. J. Green, "Carbon monoxide-releasing molecules characterization of biochemical and vascular activities", Circ. Res. **90**, e17–e24 (2002).

[172] R. Motterlini, P. Sawle, J. Hammad, S. Bains, R. Alberto, R. Foresti, and C. J. Green, "CORM-A1: a new pharmacologically active carbon monoxide-releasing molecule", FASEB J. **19**, 284–286 (2005).

[173] L. A. P. Antony, T. Slanina, P. Šebej, T. Šolomek, and P. Klán, "Fluorescein analogue xanthene-9-carboxylic acid: a transition-metal-free CO releasing molecule activated by green light", Org. Lett. **15**, 4552–4555 (2013).

[174] S. Pai, K. Radacki, and U. Schatzschneider, "Sonogashira, CuAAC, and oxime ligations for the synthesis of Mn^{I} tricarbonyl PhotoCORM peptide conjugates", Eur. J. Inorg. Chem. **2014**, 2886–2895 (2014).

[175] L. Chen, X. Jiang, X. Wang, L. Long, J. Zhang, and X. Liu, "A kinetic analysis of CO release from a diiron hexacarbonyl complex promoted by amino acids", New J. Chem. **38**, 5957–5963 (2014).

[176] S. Romanski, B. Kraus, U. Schatzschneider, J.-M. Neudörfl, S. Amslinger, and H.-G. Schmalz, "Acyloxybutadiene iron tricarbonyl complexes as enzyme-triggered CO-releasing molecules (ET-CORMs)", Angew. Chem. Int. Ed. **50**, 2392–2396 (2011).

[177] P. C. Kunz, H. Meyer, J. Barthel, S. Sollazzo, A. M. Schmidt, and C. Janiak, "Metal carbonyls supported on iron oxide nanoparticles to trigger the CO-gasotransmitter release by magnetic heating", Chem. Commun. **49**, 4896–4898 (2013).

[178] R. D. Rimmer, H. Richter, and P. C. Ford, "A photochemical precursor for carbon monoxide release in aerated aqueous media", Inorg. Chem. **49**, 1180–1185 (2009).

[179] U. Schatzschneider, "PhotoCORMs: light-triggered release of carbon monoxide from the coordination sphere of transition metal complexes for biological applications", Inorg. Chim. Acta **374**, 19–23 (2011).

[180] R. D. Rimmer, A. E. Pierri, and P. C. Ford, "Photochemically activated carbon monoxide release for biological targets. Toward developing air-stable photoCORMs labilized by visible light", Coord. Chem. Rev. **256**, 1509–1519 (2012).

[181] P. Šebej, J. Wintner, P. Müller, T. Slanina, J. Al Anshori, L. A. P. Antony, P. Klán, and J. Wirz, "Fluorescein analogues as photoremovable protecting groups absorbing at ~520 nm", J. Org. Chem. **78**, 1833–1843 (2013).

[182] I. Chakraborty, S. J. Carrington, and P. K. Mascharak, "Design strategies to improve the sensitivity of photoactive metal carbonyl complexes (photoCORMs) to visible light and their potential as CO-donors to biological targets", Acc. Chem. Res. **47**, 2603–2611 (2014).

[183] H. Hildenbrand, "Zwei-Photonen-Anregung mit Nachweis im Infraroten", Bachelor thesis, Universität Würzburg (2012).

[184] C. Nagel, S. McLean, R. K. Poole, H. Braunschweig, T. Kramer, and U. Schatzschneider, "Introducing $[Mn(CO)_3(tpa\text{-}\kappa^3N)]^+$ as a novel photoactivatable CO-releasing molecule with well-defined iCORM intermediates – synthesis, spectroscopy, and antibacterial activity", Dalton Trans. **43**, 9986–9997 (2014).

[185] G. L. Geoffrey and M. S. Wrighton, *Organometallic Photochemistry* (Academic Press, New York, 1979).

[186] C. Elschenbroich, *Organometallchemie* (Vieweg+Teubner, Wiesbaden, 2008), 6th ed.

[187] W. Strohmeier and D. von Hobe, "Quantenausbeute als Funktion der Wellenlänge bei der photochemischen Bildung von Metallcarbonylderivaten", Z. Phys. Chem. **34**, 393–400 (1962).

[188] W. Strohmeier, D. Hobe, von, G. Schönauer, and H. Laporte, "Einfluß des Zentralatoms und der Donatoren auf die photochemische Bildung von Metallcarbonyl-Derivaten", Z. Naturforsch. **17b**, 502–504 (1962).

[189] L. Bañares, T. Baumert, M. Bergt, B. Kiefer, and G. Gerber, "Femtosecond photodissociation dynamics of $Fe(CO)_5$ in the gas phase", Chem. Phys. Lett. **267**, 141–148 (1997).

[190] L. Bañares, T. Baumert, M. Bergt, B. Kiefer, and G. Gerber, "The ultrafast photodissociation of $Fe(CO)_5$ in the gas phase", J. Chem. Phys. **108**, 5799–5811 (1998).

[191] S. A. Trushin, W. Fuss, K. L. Kompa, and W. E. Schmid, "Femtosecond dynamics of $Fe(CO)_5$ photodissociation at 267 nm studied by transient ionization", J. Phys. Chem. A **104**, 1997–2006 (2000).

[192] H. Ihee, J. Cao, and A. H. Zewail, "Ultrafast electron diffraction of transient $[Fe(CO)_4]$: determination of molecular structure and reaction pathway", Angew. Chem. Int. Ed. **40**, 1532–1536 (2001).

[193] A. Assion, T. Baumert, M. Bergt, T. Brixner, B. Kiefer, V. Seyfried, M. Strehle, and G. Gerber, "Control of chemical reactions by feedback-optimized phase-shaped femtosecond laser pulses", Science **282**, 919–922 (1998).

[194] M. Bergt, T. Brixner, B. Kiefer, M. Strehle, and G. Gerber, "Controlling the femtochemistry of $Fe(CO)_5$", J. Phys. Chem. A **103**, 10381–10387 (1999).

[195] P. T. Snee, C. K. Payne, S. D. Mebane, K. T. Kotz, and C. B. Harris, "Dynamics of photosubstitution reactions of $Fe(CO)_5$: an ultrafast infrared study of high spin reactivity", J. Am. Chem. Soc. **123**, 6909–6915 (2001).

[196] P. Portius, J. Yang, X.-Z. Sun, D. C. Grills, P. Matousek, A. W. Parker, M. Towrie, and M. W. George, "Unraveling the photochemistry of $Fe(CO)_5$ in solution: observation of $Fe(CO)_3$ and the conversion between $^3Fe(CO)_4$ and $^1Fe(CO)_4$(solvent)", J. Am. Chem. Soc. **126**, 10713–10720 (2004).

[197] M. Besora, J.-L. Carreón-Macedo, A. J. Cowan, M. W. George, J. N. Harvey, P. Portius, K. L. Ronayne, X.-Z. Sun, and M. Towrie, "A combined theoretical and experimental study on the role of spin states in the chemistry of $Fe(CO)_5$ photoproducts", J. Am. Chem. Soc. **131**, 3583–3592 (2009).

[198] S. C. Nguyen, J. P. Lomont, M. C. Zoerb, A. D. Hill, J. P. Schlegel, and C. B. Harris, "Chemistry of the triplet 14-electron complex $Fe(CO)_3$ in solution studied by ultrafast time-resolved IR spectroscopy", Organometallics **31**, 3980–3984 (2012).

[199] B. Ahr, M. Chollet, B. Adams, E. M. Lunny, C. M. Laperle, and C. Rose-Petruck, "Picosecond X-ray absorption measurements of the ligand substitution dynamics of $Fe(CO)_5$ in ethanol", Phys. Chem. Chem. Phys. **13**, 5590–5599 (2011).

[200] P. Wernet, M. Beye, F. d. Groot, S. Düsterer, K. Gaffney, S. Grübel, R. Hartsock, F. Hennies, I. Josefsson, B. Kennedy, K. Kunnus, T. Leitner, T. Mazza, M. Meyer, D. Nordlund, M. Odelius, W. Quevedo, P. Radcliffe, I. Rajkovic, B. Schlotter, M. Scholz, S. Schreck, E. Suljoti, S. Techert, J. Turner, C. Weniger, W. Zhang, and A. Föhlisch, "Mapping chemical bonding of reaction intermediates with femtosecond X-ray laser spectroscopy", EPJ Web of Conferences **41**, 3 (2013).

[201] S. K. Kim, S. Pedersen, and A. H. Zewail, "Femtochemistry of organometallics: dynamics of metal–metal and metal–ligand bond cleavage in $M_2(CO)_{10}$", Chem. Phys. Lett. **233**, 500–508 (1995).

[202] T. J. Meyer and J. V. Caspar, "Photochemistry of metal–metal bonds", Chem. Rev. **85**, 187–218 (1985).

[203] J. Z. Zhang and C. B. Harris, "Photodissociation dynamics of $Mn_2(CO)_{10}$ in solution on ultrafast time scales", J. Chem. Phys. **95**, 4024–4032 (1991).

[204] J. C. Owrutsky and A. P. Baronavski, "Ultrafast infrared study of the ultraviolet photodissociation of $Mn_2(CO)_{10}$", J. Chem. Phys. **105**, 9864–9873 (1996).

[205] D. A. Steinhurst, A. P. Baronavski, and J. C. Owrutsky, "Transient infrared spectroscopy of $Mn_2(CO)_{10}$ with 400 nm excitation", Chem. Phys. Lett. **361**, 513–519 (2002).

[206] R. B. Hitam, K. A. Mahmoud, and A. J. Rest, "Photochemistry of σ-allyl complexes of manganese and tungsten in frozen gas matrices at ca. 12 K. Infrared spectroscopic evidence for photodecarbonylation and $\sigma \rightarrow \pi$ conversion processes", J. Organomet. Chem. **291**, 321–333 (1985).

[207] W. I. Dzik, C. Creusen, R. de Gelder, T. P. J. Peters, J. M. M. Smits, and B. de Bruin, "Carbonyl complexes of rhodium with N-donor ligands: factors determining the formation of terminal versus bridging carbonyls", Organometallics **29**, 1629–1641 (2010).

[208] T. Jiao, Z. Pang, T. J. Burkey, R. F. Johnston, T. A. Heimer, V. D. Kleiman, and E. J. Heilweil, "Ultrafast ring closure energetics and dynamics of cyclopentadienyl manganese tricarbonyl derivatives", J. Am. Chem. Soc. **121**, 4618–4624 (1999).

[209] T. T. To, E. J. Heilweil, C. B. Duke, K. R. Ruddick, C. E. Webster, and T. J. Burkey, "Development of ultrafast photochromic organometallics and photoinduced linkage isomerization of arene chromium carbonyl derivatives", J. Phys. Chem. A **113**, 2666–2676 (2009).

[210] E. J. Heilweil, J. O. Johnson, K. L. Mosley, P. P. Lubet, C. E. Webster, and T. J. Burkey, "Engineering femtosecond organometallic chemistry: photochemistry and dynamics of ultrafast chelation of cyclopentadienylmanganese tricarbonyl derivatives with pendant benzenecarbonyl and pyridinecarbonyl groups", Organometallics **30**, 5611–5619 (2011).

[211] M. Lim, T. A. Jackson, and P. A. Anfinrud, "Binding of CO to myoglobin from a heme pocket docking site to form nearly linear Fe–C–O", Science **269**, 962–966 (1995).

[212] M. Lim, T. A. Jackson, and P. A. Anfinrud, "Ultrafast rotation and trapping of carbon monoxide dissociated from myoglobin", Nat. Struct. Mol. Biol. **4**, 209–214 (1997).

[213] J. T. King, M. R. Ross, and K. J. Kubarych, "Water-assisted vibrational relaxation of a metal carbonyl complex studied with ultrafast 2D-IR", J. Phys. Chem. B **116**, 3754–3759 (2012).

[214] J. T. King, E. J. Arthur, C. L. Brooks, and K. J. Kubarych, "Site-specific hydration dynamics of globular proteins and the role of constrained water in solvent exchange with amphiphilic cosolvents", J. Phys. Chem. B **116**, 5604–5611 (2012).

[215] J. T. King and K. J. Kubarych, "Site-specific coupling of hydration water and protein flexibility studied in solution with ultrafast 2D-IR spectroscopy", J. Am. Chem. Soc. **134**, 18705–18712 (2012).

[216] J. Niesel, "CO release properties and biological activity of manganese tricarbonyl complexes", Dissertation, Ruhr-Universität Bochum (2012).

[217] J. Niesel, A. Pinto, H. W. Peindy N'Dongo, K. Merz, I. Ott, R. Gust, and U. Schatzschneider, "Photoinduced CO release, cellular uptake and cytotoxicity of a tris(pyrazolyl)methane (tpm) manganese tricarbonyl complex", Chem. Commun. pp. 1798–1800 (2008).

[218] H.-M. Berends and P. Kurz, "Investigation of light-triggered carbon monoxide release from two manganese photoCORMs by IR, UV–Vis and EPR spectroscopy", Inorg. Chim. Acta **380**, 141–147 (2012).

[219] M. Falk and T. A. Ford, "Infrared spectrum and structure of liquid water", Can. J. Chem. **44**, 1699–1707 (1966).

[220] J. Barrett and A. L. Mansell, "Ultra-violet absorption spectra of the molecules H_2O, HDO and D_2O", Nature **187**, 138–138 (1960).

[221] F. Neese, "The ORCA program system", WIREs Comput. Mol. Sci. **2**, 73–78 (2012).

[222] T. P. Dougherty, W. T. Grubbs, and E. J. Heilweil, "Photochemistry of $Rh(CO)_2$(acetylacetonate) and related metal dicarbonyls studied by ultrafast infrared spectroscopy", J. Phys. Chem. **98**, 9396–9399 (1994).

[223] M. J. Frisch, G. W. Trucks, H. B. Schlegel, G. E. Scuseria, M. A. Robb, J. R. Cheeseman, G. Scalmani, V. Barone, B. Mennucci, G. A. Petersson, H. Nakatsuji, M. Caricato, X. Li, H. P. Hratchian, A. F. Izmaylov, J. Bloino, G. Zheng, J. L. Sonnenberg, M. Hada, M. Ehara, K. Toyota, R. Fukuda, J. Hasegawa, M. Ishida, T. Nakajima, Y. Honda, O. Kitao, H. Nakai, T. Vreven, J. A. Montgomery, Jr., J. E. Peralta, F. Ogliaro, M. Bearpark, J. J. Heyd, E. Brothers, K. N. Kudin, V. N. Staroverov, R. Kobayashi, J. Normand, K. Raghavachari, A. Rendell, J. C. Burant, S. S. Iyengar, J. Tomasi, M. Cossi, N. Rega, J. M. Millam, M. Klene, J. E. Knox, J. B. Cross, V. Bakken, C. Adamo, J. Jaramillo, R. Gomperts, R. E. Stratmann, O. Yazyev, A. J. Austin, R. Cammi, C. Pomelli, J. W. Ochterski, R. L. Martin, K. Morokuma, V. G. Zakrzewski, G. A. Voth, P. Salvador, J. J. Dannenberg, S. Dapprich, A. D. Daniels, O. Farkas, J. B. Foresman, J. V. Ortiz, J. Cioslowski, and D. J. Fox, "Gaussian 09 revision A.1", (2009). Gaussian Inc. Wallingford CT 2009.

[224] M. P. Andersson and P. Uvdal, "New scale factors for harmonic vibrational frequencies using the B3LYP density functional method with the triple-ζ basis set 6-311+G(d,p)", J. Phys. Chem. A **109**, 2937–2941 (2005).

[225] P. Rudolf, J. Buback, J. Aulbach, P. Nuernberger, and T. Brixner, "Ultrafast multisequential photochemistry of 5-diazo meldrum's acid", J. Am. Chem. Soc. **132**, 15213–15222 (2010).

[226] P. Hamm, "Coherent effects in femtosecond infrared spectroscopy", Chem. Phys. **200**, 415–429 (1995).

[227] P. Nuernberger, K. F. Lee, A. Bonvalet, T. Polack, M. H. Vos, A. Alexandrou, and M. Joffre, "Suppression of perturbed free-induction decay and noise in experimental ultrafast pump–probe data", Opt. Lett. **34**, 3226–3228 (2009).

[228] R. Laenen, T. Roth, and A. Laubereau, "Novel precursors of solvated electrons in water: evidence for a charge transfer process", Phys. Rev. Lett. **85**, 50–53 (2000).

[229] T. P. Dougherty and E. J. Heilweil, "Transient infrared spectroscopy of $(\eta^5$–$C_5H_5)Co(CO)_2$ photoproduct reactions in hydrocarbon solutions", J. Chem. Phys. **100**, 4006–4009 (1994).

[230] T. P. Dougherty and E. J. Heilweil, "Ultrafast transient infrared absorption studies of $M(CO)_6$ (M = Cr, Mo or W) photoproducts in *n*-hexane solution", Chem. Phys. Lett. **227**, 19–25 (1994).

[231] S. K. Pal, J. Peon, B. Bagchi, and A. H. Zewail, "Biological water: femtosecond dynamics of macromolecular hydration", J. Phys. Chem. B **106**, 12376–12395 (2002).

[232] T. Lian, S. E. Bromberg, M. C. Asplund, H. Yang, and C. B. Harris, "Femtosecond infrared studies of the dissociation and dynamics of transition metal carbonyls in solution", J. Phys. Chem. **100**, 11994–12001 (1996).

[233] S. V. C. Vummaleti, D. Branduardi, M. Masetti, M. De Vivo, R. Motterlini, and A. Cavalli, "Theoretical insights into the mechanism of carbon monoxide (CO) release from CO-releasing molecules", Chem. Eur. J. **18**, 9267–9275 (2012).

[234] P. J. Giordano and M. S. Wrighton, "Photosubstitution behavior of dicarbonyl(η^5-cyclopentadienyl)pyridinomanganese and -rhenium and related complexes", Inorg. Chem. **16**, 160–166 (1977).

[235] M. A. Gonzalez, M. A. Yim, S. Cheng, A. Moyes, A. J. Hobbs, and P. K. Mascharak, "Manganese carbonyls bearing tripodal polypyridine ligands as photoactive carbon monoxide-releasing molecules", Inorg. Chem. **51**, 601–608 (2012).

[236] D. Schleier, "Zeitaufgelöste Spektroskopie an Tetrazoliumsalzen", Bachelor thesis, Universität Würzburg (2013).

[237] H. v. Pechmann and P. Runge, "Oxydation der Formazylverbindungen. II. Mittheilung", Ber. Dtsch. Chem. Ges. **27**, 2920–2930 (1894).

[238] A. M. Mattson and C. O. Jensen, "Colorimetric determination of reducing sugars with triphenyltetrazolium chloride." Anal. Chem. **22**, 182–185 (1950).

[239] K. Wallenfels, "Über einen neuen Nachweis reduzierender Zucker im Papierchromatogramm und dessen quantitative Auswertung", Naturwissenschaften **37**, 491–492 (1950).

[240] T. Mosmann, "Rapid colorimetric assay for cellular growth and survival: application to proliferation and cytotoxicity assays", J. Immunol. Methods **65**, 55–63 (1983).

[241] M. V. Berridge, P. M. Herst, and A. S. Tan, "Tetrazolium dyes as tools in cell biology: new insights into their cellular reduction", in "Biotechnology Annual Review," , vol. 11, M.R. El-Gewely, ed. (Elsevier, 2005), pp. 127–152.

[242] M. C. Alley, D. A. Scudiero, A. Monks, M. L. Hursey, M. J. Czerwinski, D. L. Fine, B. J. Abbott, J. G. Mayo, R. H. Shoemaker, and M. R. Boyd, "Feasibility of drug screening with panels of human tumor cell lines using a microculture tetrazolium assay", Cancer Res. **48**, 589–601 (1988).

[243] J. Carmichael, W. G. DeGraff, A. F. Gazdar, J. D. Minna, and J. B. Mitchell, "Evaluation of a tetrazolium-based semiautomated colorimetric assay: assessment of chemosensitivity testing", Cancer Res. **47**, 936–942 (1987).

[244] G. Lakon, "The topographical tetrazolium method for determining the germinating capacity of seeds", Plant Physiol. **24**, 389–394 (1949).

[245] R. P. Moore, "Tetrazolium seed testing dvelopments in North America", J. Seed Technol. **1**, 17–30 (1976).

[246] B. Jámbor, *Tetrazoliumsalze in der Biologie* (VEB Gustav Fischer, Jena, 1960).

[247] E. Seidler, *The Tetrazolium-Formazan System: Design and Histochemistry*, vol. 24 of *Progress in Histochemistry and Cytochemistry* (Gustav Fischer Verlag, Stuttgart, 1991).

[248] R. Muthyala, *Chemistry and Applications of Leuco Dyes* (Plenum Press, New York, 1997).

[249] W. Ried, "Formazane und Tetrazoliumsalze, ihre Synthesen und ihre Bedeutung als Reduktionsindikatoren und Vitalfarbstoffe", Angew. Chem. **64**, 391–396 (1952).

[250] A. W. Nineham, "The chemistry of formazans and tetrazolium salts", Chem. Rev. **55**, 355–483 (1955).

[251] F. Altman, "Tetrazolium salts and formazans", Prog. Histochem. Cytochem. **9**, III–VI,1–51 (1976).

[252] F. Weygand and I. Frank, "Über die Einwirkung von Licht auf Tetrazolium-Verbindungen: Tetrazolium-Typie. I. Mitt." Z. Naturforsch. **3b**, 377–379 (1948).

[253] D. Jerchel and H. Fischer, "Diphenyl-substituierte Formazane und Tetrazoliumsalze", Liebigs Ann. Chem. **563**, 200–207 (1949).

[254] I. Hausser, D. Jerchel, and R. Kuhn, "Ein blau fluorescierendes Bestrahlungsprodukt von Triphenyltetrazolium-chlorid", Chem. Ber. **82**, 195–199 (1949).

[255] K. H. Hausser, "Die Quantenbilanz der cis-trans-Umwandlung von Triphenylformazan durch sichtbares Licht", Naturwiss. **36**, 313–314 (1949).

[256] B. Jámbor, "Tetrazoliumvegyületek fényreakciói I. A diszproporcionálódási reakció", Agrokem. Talajtan **5**, 89–98 (1956).

[257] M. C. González and E. San Román, "Photochemistry of aqueous solutions of triphenyltetrazolium chloride", J. Phys. Chem. **93**, 3536–3540 (1989).

[258] R. T. Lofberg, "Electron spin resonance signals of tetrazolium compounds", Nature **206**, 503–504 (1965).

[259] F. A. Neugebauer and G. A. Russell, "Tetrazolinyl radicals", J. Org. Chem. **33**, 2744–2746 (1968).

[260] F. A. Neugebauer, "The constitution of the radical intermediate between formazan and tetrazoliumsalt", Tetrahedron Lett. **17**, 2129–2132 (1968).

[261] K. Umemoto, "Reduction mechanism of 2,3,5-triphenyltetrazolium chloride and 1,3,5-triphenylformazan", Bull. Chem. Soc. Jpn. **58**, 2051–2055 (1985).

[262] K. Umemoto, "Electrochemical studies of the reduction mechanism of tetrazolium salts and formazans", Bull. Chem. Soc. Jpn. **62**, 3783–3789 (1989).

[263] P. Rapta, V. Brezová, M. Čeppan, M. Melnik, D. Bustin, and A. Staško, "Radical intermediates in the redox reactions of tetrazolium salts in aprotic solvents (cyclovoltammetric, EPR and UV-VIS study)", Free Radical Res. **20**, 71–82 (1994).

[264] A. Kovács, L. Wojnárovits, W. L. McLaughlin, S. E. E. Eid, and A. Miller, "Radiation-chemical reaction of 2,3,5-triphenyl-tetrazolium chloride in liquid and solid state", Radiat. Phys. Chem. **47**, 483–486 (1996).

[265] E. W. Castner, D. Kennedy, and R. J. Cave, "Solvent as electron donor: donor/acceptor electronic coupling is a dynamical variable", J. Phys. Chem. A **104**, 2869–2885 (2000).

[266] S. T. Repinec, R. J. Sension, A. Z. Szarka, and R. M. Hochstrasser, "Femtosecond laser studies of the *cis*-stilbene photoisomerization reactions: the *cis*-stilbene to dihydrophenanthrene reaction", J. Phys. Chem. **95**, 10380–10385 (1991).

[267] M. Greenfield, S. D. McGrane, and D. S. Moore, "Control of *cis*-stilbene photochemistry using shaped ultraviolet pulses", J. Phys. Chem. A **113**, 2333–2339 (2009).

[268] F. B. Mallory and C. W. Mallory, "Photocyclization of stilbenes and related molecules", in "Organic Reactions," , vol. 30, W. G. Dauben, G. A. Boswell, Jr., R. F. Hirschmann, S. Danishefsky, L. A. Paquette, H. A. Gschwend, G. H. Posner, R. F. Heck, and H. J. Reich, eds. (John Wiley & Sons, Inc., 1984). Cf. compound **401**.

[269] H. Wang, C. Burda, G. Persy, and J. Wirz, "Photochemistry of 1*h*-benzotriazole in aqueous solution: a photolatent base", J. Am. Chem. Soc. **122**, 5849–5855 (2000).

[270] X. Pang, B. Hou, W. Li, F. Liu, and Z. Yu, "2,3,5-Triphenyl-2*h*-tetrazolium chloride and 2,4,6-tri(2-pyridyl)-s-triazine on the corrosion of mild steel in HCl", Chin. J. Chem. Eng. **15**, 909–915 (2007).

[271] D. D. Zorn, J. A. Boatz, and M. S. Gordon, "Electronic structure studies of tetrazolium-based ionic liquids", J. Phys. Chem. B **110**, 11110–11119 (2006).

[272] F. A. Neugebauer and H. Trischmann, "Über Tetraaza-pentenyl-Radikale", Monatsh. Chem. **97**, 554–569 (1966).

[273] A. I. Bogatyreva, O. M. Polumbrik, and A. L. Buchachenko, "Kinetics of photochemical reactions of triphenylverdazyl radicals", Russ. Chem. Bull. **23**, 2122–2125 (1974).

[274] C. Weinert, B. Wezisla, J. Lindner, and P. Vöhringer, "Ultrafast primary processes of the stable neutral organic radical, 1,3,5-triphenylverdazyl, in liquid solution", Phys. Chem. Chem. Phys. **17**, 13659–13671 (2015).

[275] O. M. Polumbrik, "Advances in the chemistry of verdazyl radicals", Russ. Chem. Rev. **47**, 767 (1978).

[276] R. G. Hicks, "What's new in stable radical chemistry?" Org. Biomol. Chem. **5**, 1321–1338 (2007).

[277] C. Reichardt, *Solvents and Solvent Effects in Organic Chemistry* (Wiley-VCH, Weinheim, 2011), 4th ed.

[278] M. J. Kamlet, J. L. M. Abboud, M. H. Abraham, and R. W. Taft, "Linear solvation energy relationships. 23. A comprehensive collection of the solvatochromic parameters, π^*, α, and β, and some methods for simplifying the generalized solvatochromic equation", J. Org. Chem. **48**, 2877–2887 (1983).

[279] International Union of Pure and Applied Chemistry, *IUPAC. Compendium of Chemical Terminology – the "Gold Book"* (http://goldbook.iupac.org/index.html, 2014), 2nd ed.

[280] T. R. Griffiths and D. C. Pugh, "Correlations among solvent polarity scales, dielectric constant and dipole moment, and a means to reliable predictions of polarity scale values from current data", Coord. Chem. Rev. **29**, 129–211 (1979).

[281] G. Wypych, ed., *Handbook of Solvents* (ChemTec Publishing, Toronto, 2001).

[282] K. M. Kadish and J. E. Anderson, "Purification of solvents for electroanalysis: benzonitrile; dichloromethane; 1,1-dichloroethane and 1,2-dichloroethane", Pure Appl. Chem. **59** (1987).

[283] K. Umemoto, "Reaction of hydroxide ion with electron acceptors in acetonitrile", Chem. Lett. **14**, 1415–1418 (1985).

[284] K. Umemoto, Y. Nagase, and Y. Sasaki, "Reaction of hydroxide ion with electron donors in aprotic solvents", Bull. Chem. Soc. Jpn. **67**, 3245–3248 (1994).

[285] I. Moreno-Villoslada, M. Soto, F. González, F. Montero-Silva, S. Hess, I. Takemura, K. Oyaizu, and H. Nishide, "Reduction of 2,3,5-triphenyl-2H-tetrazolium chloride in the presence of polyelectrolytes containing 4-styrenesulfonate moieties", J. Phys. Chem. B **112**, 5350–5354 (2008).

[286] R. E. Graham, E. R. Biehl, and C. T. Kenner, "Effect of laboratory light on tetrazolium reaction and on stability of formazans in various solvents", J. Pharm. Sci. **66**, 965–970 (1977).

[287] H. Hiura and H. Takahashi, "Resonance Raman and absorption studies of the configurations of photochromic 3-alkyl-substituted 1,5-diphenylformazans: steric effect of the substituent", J. Mol. Struct. **212**, 221–233 (1989).

[288] H. Hiura and H. Takahashi, "Study of the configurations of 3-aryl-substituted 1,5-diphenylformazans by resonance raman and absorption spectroscopy: steric and conjugation effects of the substituent", J. Mol. Struct. **212**, 235–245 (1989).

[289] R. Kuhn and H. M. Weitz, "Photochemie des Triphenylformazans", Chem. Ber. **86**, 1199–1212 (1953).

[290] Y. Marcus, "The properties of organic liquids that are relevant to their use as solvating solvents", Chem. Soc. Rev. **22**, 409–416 (1993).

[291] D. R. Lide, *CRC Handbook of Chemistry and Physics* (CRC Press, Boca Raton, FL, 1998), 79th ed.

[292] J. A. Riddick, W. B. Bunger, and T. K. Sakano, *Organic Solvents: Physical Properties and Methods of Purification* (John Wiley & Sons, New York, 1986), 4th ed.

[293] K. B. Snow and T. F. Thomas, "Mass spectrum, ionization potential, and appearance potentials for fragment ions of sulfuric acid vapor", Int. J. Mass Spectrom. Ion Processes **96**, 49–68 (1990).

[294] W. Tao, R. B. Klemm, F. L. Nesbitt, and L. J. Stief, "A discharge flow-photoionization mass spectrometric study of hydroxymethyl radicals (H_2COH and H_2COD): photoionization spectrum and ionization energy", J. Phys. Chem. **96**, 104–107 (1992).

[295] J. L. Holmes and F. P. Lossing, "Ionization energies of homologous organic compounds and correlation with molecular size", Org. Mass Spectrom. **26**, 537–541 (1991).

[296] R. D. Bowen and A. Maccoll, "Low energy, low temperature mass spectra 2—low energy, low temperature mass spectra of some small saturated alcohols and ethers", Org. Mass Spectrom. **19**, 379–384 (1984).

[297] J. D. Shao, T. Baer, and D. K. Lewis, "Dissociation dynamics of energy-selected ion-dipole complexes. 2. Butyl alcohol ions", J. Phys. Chem. **92**, 5123–5128 (1988).

[298] G. P. Dubey, M. Sharma, and S. Oswal, "Volumetric, transport, and acoustic properties of binary mixtures of 2-methyl-1-propanol with hexadecane and squalane at t = (298.15, 303.15, and 308.15) K: experimental results, correlation, and prediction by the ERAS model", J. Chem. Thermodyn. **41**, 849–858 (2009).

Acknowledgments

This presented work would not have been possible in its actual form without the support of several people I appreciate to have worked with during this thesis. All the projects would not have been as successful as they were, if not conducted in the unique and inspiring atmosphere at the “Lehrstuhl für Physikalische Chemie I”. In the following, I would like to thank those people for their individual or collective support:

- Prof. Dr. Tobias Brixner for the opportunity to carry out this work in his research group. I especially want to thank him for the trust and the freedom he gave me what allowed the development of own ideas and creativity. The perfect working environment with regards to equipment, staff, and personal support satisfies every need of a young researcher. Furthermore, I would like to thank him for his encouragements, his help to focus on the right aspects of a project in the right moment, and his ambition to qualify his coworkers as individually well-trained members in a group of excellent scientists.
- Prof. Dr. Patrick Nuernberger for the cooperation in several projects during my work. His willingness to contribute to many projects in our group in detail really helped to push them forward. I am grateful for your valuable ideas and many stimulating discussions. Without your advices and impressive literature knowledge, so many projects would lack important and improving aspects.
- Prof. Dr. Christoph Lambert for the excellent cooperation on the donor–acceptor compounds. I especially want to thank Prof. Lambert for many fruitful discussions and for giving valuable insights into many aspects of charge transfer. I thank his coworker Han Lu who always provided samples in no time what made the work with him so pleasant. Dr. Marco Holzapfel contributed with DFT calculations and many discussions about the right performance of electron-transfer calculations.
- Prof. Dr. Ulrich Schatzschneider for the superb collaboration on the CORMs, many productive discussions, and the TDDFT calculations. His coworkers Dr. Johanna Niesel and Christoph Nagel are acknowledged for their steady support with samples of the CORM.
- Dr. Phillipp Rudolf for successfully working together on the CORM project. I especially want to thank him for the friendly working atmosphere in the lab and the shared office. Regardless of which challenge we faced in the lab, his personality made it impossible to give up hope. I guess the perfect teamwork contributed to the success of the whole project. Also I thank him for taking care of our reference system and the homepage, tasks the whole group benefited from.
- Dr. Stefan Rützel for the excellent common work on the oligomer project. Without his expertise and experience, the spectroscopy on the oligomers would not have been such a smooth project. I enjoyed discussing with him many aspects of spectroscopy. I also appreciate his proofreading of large parts of this thesis and helpful advice in the lab.
- Reiner Eck for the collaboration on the 100 kHz setup. Thanks to his excellent ideas and ongoing interest in the project, the realization of the high-repetition-rate chopping was made possible at all. I also thank him for his help with any other electronics problem.
- Dr. Christian Rewitz for being such a pleasant office mate and for many stimulating discussions. I really enjoyed your company and your nature. By the way, sorry for ignoring your “red light” so often.

- Sabine Keiber for helping a lot at the beginning of the 100 kHz project during her Master thesis. I really appreciated her brilliant ideas and endurance no matter how hard the laser challenged us. Domenik Schleier contributed extremely helpful during his Bachelor thesis on tetrazolium salts with own ideas and large commitment. Heiko Hildenbrand helped diligently in the MIR team to set up the two-photon absorption detection setup during his Bachelor thesis. Nina Schopf and Dominik Gehrig were working during their internships on different projects. Both of them were reliable and eagerly working students. I hope, that all of them profited well from our common time.
- Dr. Martin Kullmann for many helpful discussions, shared coffee breaks, and for his help and advice in the lab.
- Sebastian Schott for the shared lab time during which we build up the UV pump beam line. I also want to acknowlegde his critical proofreading of parts of this thesis and maintaining our reference system.
- Christian Kramer for discussions about error propagation and Fourier transformation. Sharing your profound knowledge helped me a lot, as well as your immediate corrections when proofreading parts of this thesis.
- Johannes Knorr for his help in the lab in the MIR project.
- The technical assistants Sabine Fuchs and Belinda Böhm for taking care of all the occurring laser issues and other technical help. I am grateful for your commitment on helping to align the 100 kHz laser what gave me more time to work on the project itself. The technical assistants Sabine Stahl and Gudrun Mühlrath are thanked for providing all the chemistry lab infrastructure.
- The mechanical-workshop crew, namely Wolfgang Liebler, Katharina Schreckling, Ralf Kohrmann, Gerhard Bömmel, and Peter Lang for producing excellent solutions for all kinds of mountings, cuvette holders, and many more fast and superb solutions of whatever mechanical problem emerged in the lab.
- The secretaries Andrea Gehring and Anna Rosenfeldt for their help in all administrative concerns. Due to your help we can really focus on our research.
- Dr. Johannes Buback, Andreas Steinbacher, and Sebastian Röding for taking care of our "VI-Pool". Without your work, measuring in the lab would have been much more complicated. Dr. Johannes Buback is additionally granted for his help in coding for the ultrafast line camera.
- Jürgen Zimmermann and Dr. Jens Petersen for their server maintenance. Christoph Schwarz is thanked for taking care of our workstations.
- Johannes H. Klein for proofreading parts of this thesis and helpful discussions about several aspects of mixed-valence chemistry.
- Dr. Antigoni Alexandrou and Dr. Sergey Laptenok for providing incentives about high-speed chopping. Sergey also provided helpful knowledge about Glotaran.
- The Fonds der Chemischen Industrie is acknowledged for financial support via a scholarship, as well as the German Research Foundation for financial support via the DFG Research Unit FOR 1809. The graduate college GRK 1221 is thanked for the educational support, namely Prof. Dr. Bernd Engels and Uschi Rüppel for providing such an excellent platform to get a glance of what is left and right of ones own research.
- All the so far unmentioned members of the PC I team and the Institute of Physical and Theoretical Chemistry are thanked for the friendly working atmosphere.

Finally, I want to express my gratefulness to my friends with whom the studies and the necessary distractions over the last years made such a wonderful time. However, my deepest gratitude goes to my parents and my family, whose love and support made it possible for me to come where I am standing now and who always took care of me. Especially, I want to thank my precious girlfriend Marie Markones for her ongoing support and love, and for making back-sets more bearable and lucky moments even more extraordinary.